DYNAMIC B_0 SHIMMING AT 7 TESLA

By

SAIKAT SENGUPTA

Dissertation
Submitted to the Faculty of the
Graduate School of Vanderbilt University
in partial fulfillment of the requirements
for the degree of

DOCTOR OF PHILOSOPHY

in
Biomedical Engineering
December, 2010
Nashville, Tennessee
Approved:

Professor Malcolm J. Avison
Professor John C. Gore
Professor Adam W. Anderson
Professor Mark D. Does
Professor Edward B. Welch

To my parents

and

To my wife Gourija

ACKNOWLEDGEMENTS

There is a long list of people I wish to thank, without whose help and guidance this work would never have been accomplished. First and foremost, I would like to thank my advisor Dr Malcolm J Avison for making this possible. He has spent countless hours imparting knowledge, patiently analyzing my work and encouraging me, without ever making it seem like a burden. It has been a pleasure to work under his guidance. I would like to thank Dr. John Gore for his valuable guidance and support. I am truly indebted to him for giving me the opportunity to be a part of the Vanderbilt University Institute of Imaging Science (VUIIS), one of the premier imaging institutes in the world and supporting my time in graduate school.

I am especially grateful to Dr. Edward B Welch, who has helped me from the onset in almost all aspects of the work. He has often been an 'on the field' guide for me. This work would never have been possible without his help. I would also like to thank Dr Anderson and Dr Does for their valuable comments and suggestions and for their help in correcting this thesis. I am indebted towards Dr. Yansong Zhao, who got me started in the project with his excellent work, Dr. David Foxall and Chuck Nockowsksi who can brighten anybody's day.

Several other people have helped me immensely in this work and in my learning process. I cherish with pleasure my discussions with Dr. Huairen Zeng, who was ever willing to sit down with a pen and paper and clarify my doubts. I would like to thank Dr.Vicki Morgan, Dr. Allen Newton, Dr. Ha-Kyu Jeong, Dr. Amanda Wake, Dr. David

Smith for their help, and my office mates Chris Wargo, Jack Skinner, Elizabeth Ann Stringer and Jennifer Whisenant for making this an enjoyable journey.

Finally, I would not have finished this work without the love and support of my family. My parents, who always believed in me and encouraged me to strive harder. Most importantly, my wife, Gourija, whose love, support and undying faith in my work has brought me here. They will be happiest to see the success of this endeavor.

TABLE OF CONTENTS

Page

LIST OF TABLES

Table Page

LIST OF FIGURES

CHAPTER I

OBJECTIVES AND SPECIFIC AIMS

1.1 Objectives

Recent developments in magnetic resonance imaging (MRI) hardware in the realm of increasing magnetic field strengths have pushed the boundaries of signal and resolutions achievable. Today, high field strength magnets (3 Tesla and greater) are being employed more commonly in order to obtain stronger MR signals, larger spectral dispersions and greater blood oxygen level dependent (BOLD) effects. However, along with increased gains, higher field strengths bring with them a host of challenges, primary among them being increased main field (B_0) inhomogeneity (ΔB_0) arising from the magnetic susceptibility variations between different tissues. These field inhomogeneities can detract heavily from the theoretical benefits of high field leading to reduced signal dropout and severe distortions in imaging and broader line widths in spectroscopy. Compensation of field inhomogeneities has traditionally been carried out by room temperature static global shimming using a set of discrete orthogonal shim coils designed to produce specific spatial field corrections to minimize field inhomogeneities. Dynamic shimming is a more advanced technique of field shimming, in which the shim settings are changed during the acquisition of data from individual slices or sub-volumes or are changed to accommodate temporal variations in B_0 homogeneity. Therefore, multiple shim settings optimal for each slice, sub-volume or time point can be applied during a single experiment, leading to improved localized compensation of field inhomogeneities,

compared with that obtained using a single global shim set. The implementation of dynamic shimming presents technical challenges, primary among them being slowly decaying eddy currents produced by rapidly switching shims. These eddy currents produce eddy fields, which distort the magnetic field both spatially and temporally. Nevertheless, with increasing field strengths and consequently higher susceptibility artifacts, dynamic shimming may be an important tool to improve image quality compared to conventional shimming techniques.

The overall purpose of this work is to implement and assess the ability of dynamic shimming to improve image quality at ultra-high field The measurement and compensation of eddy fields is also a focus of major effort, as it is imperative to the successful implementation of dynamic shimming. To this end, the work is divided into 3 specific aims listed below.

1.2 Specific aim 1: Implementation of dynamic B_0 shimming

Fieldmap based dynamic slice-wise shimming is implemented on a human 7 Tesla clinical scanner. Different shim calculation techniques are implemented. Real time shim switching hardware is integrated for dynamic shim update and software tools are developed for expedited shim analysis. This work is described in chapter 3.

1.3 Specific aim 2: Evaluation of dynamic B_0 shimming

In the second part of the work, simulations as well as phantom and invivo studies are performed to compare slicewise dynamic shimming to conventional image based 2^{nd} order static global shimming. 2^{nd} and 3^{rd} order shim induced eddy currents are

characterized. An order wise comparison of static and dynamic shimming methods is also performed to evaluate the benefits of going to higher orders from lower order shims and to dynamic shim update from a static shimming regime. This work is presented in chapter 4.

1.4 Specific aim 3: Software based compensation of shim induced eddy fields

Shim switching induced eddy currents can introduce significant field errors in dynamic shimming. In this part of the work, a novel method of prospective eddy field compensation (EFC) applied to higher order dynamic shim induced eddy currents is developed and implemented. The method does not require the use of extra hardware for eddy current compensation (ECC) or shim shielding and is based on an assumption of reaching an eddy field steady state during an imaging sequence. This work is presented in chapter 5.

Chapter 2 provides a detailed review of magnetic field inhomogeneity, it origins, effects and techniques for measuring the same. It discusses in detail the primary approach to the prospective correction of field homogeneity, ie ΔB_0 shimming, the primary topic of study in this thesis. It introduces an advanced form of shimming, namely *dynamic shimming* and explains its advantages over conventional shimming techniques. Finally, it gives a brief introduction to eddy currents in MRI, including methods of eddy current mitigation.

CHAPTER II

BACKGROUND AND SIGNIFICANCE

2.1. Static magnetic field

In Magnetic resonance imaging (MRI) a strong static magnetic field with uniform magnitude and orientation (B_0) is required to polarize the nuclear spins in an object placed within the field. The nuclear spins precess about the externally applied magnetic field B_0 with the angular frequency given by

$$\omega_0 = \gamma B_0 \tag{2.1}$$

where γ is a physical constant known as the gyromagnetic ratio, the value of which is nucleus dependent and ω_0 is the angular precession frequency, also called the Larmor frequency. In water, the hydrogen proton has a γ value of approximately 2.68 x 10^8 radians/second/Tesla (or $\chi = \gamma/2\pi$ = 42.58 MHz/Tesla). In a perfectly uniform magnetic field, all the nuclear spins of the same species are aligned and spin with the same Larmor frequency about the applied magnetic field direction. This setup provides the canvas on which magnetic field gradients are then applied, to encode spatial position with frequency for imaging.

2.2. Field inhomogeneity (ΔB_0)

An important aspect of the main magnetic field is the spatial uniformity, often expressed in parts per million (ppm) of field deviation from the specified field. In real

world scenarios, perfectly uniform magnets are never available. Typically, factory installed magnets have inherent field inhomogeneities of less than 0.5 parts per million (ppm) in magnitude over the imaging field of view. These small inhomogeneities result from imperfections in magnet construction.

2.2.1 Magnetic susceptibility differences

The introduction of an object into the field gives rise to local field perturbations. These field perturbations arise from differences in macroscopic magnetic susceptibilities (χ) within that object and between the object and the medium. χ is a dimensionless scalar quantity that measures the degree to which the material becomes magnetized. The field perturbation at any point in the object caused due to a susceptibility boundary can be expressed as [Bhagwandien 1994, Truong TK 2002, Yoder 2004]:

$$\Delta B_0(x,y,z) = \Delta\chi \,.\, D(x,y,z).B_0 \tag{2.2}$$

where $\Delta B_0(x,y,z)$ is the inhomogeneity at location (*x, y, z*) inside the object, $\Delta\chi$ is the susceptibility difference at the material boundary and $D(x,y,z)$ is a geometry factor given by

$$D = \frac{1}{B_0 4\pi}\oint_S \frac{(z'-z)}{\left[(x'-x)^2+(y'-y)^2+(z'-z)^2\right]^3}.B_0.dS + 1 \tag{2.3}$$

where (x',y',z') represents a point on the object's closed surface *S*. B_0 is constant and therefore, the integral over *S* is a function only of the object's geometry.

According to Eq 2.2, ΔB_0 depends on:

1. The main field strength, B_0: ΔB_0 is seen to scale linearly with the main field strength. At high field strengths, this causes the adverse effects of ΔB_0 in imaging and spectroscopy to be extremely detrimental.
2. The susceptibility difference $\Delta\chi$: ΔB_0 is directly proportional to the susceptibility difference between the two materials. In *invivo* scans, large susceptibility differences seen at the air-bone-tissue interfaces lead to high ΔB_0 levels as well as high field gradients across individual voxels at these locations. In the human head, the most severe effects are seen in the inferior frontal cortex superior to the sphenoid and ethmoid sinuses and in the inferior temporal cortex superior to the auditory canals and mastoid air cells. These χ differences often produce field inhomogeneities of several ppm.
3. The geometry of the object and its orientation with respect to the main magnetic field, as given by the geometry factor *D*.

In addition to the static ΔB_0 effect caused by the susceptibility differences at the tissue interfaces, ΔB_0 can also vary temporally in the brain due to a variety of physiological processes in the body that do not necessarily originate in the head. For example, the field homogeneity in the brain has been shown to vary with cardiovascular pulsation, brain motion and respiration [Raj 2000, 2001, Hu 1995, Poncelet 1992]. In particular, the movement of the lungs and diaphragm during respiration causing volume changes can affect the field in the brain [Raj 2000]. In addition the exchange of gases

having different magnetic susceptibilities during respiration can also cause field fluctuations [Zhao 2005a]. For example, the susceptibility of air in the lungs changes according to the concentrations of oxygen (O_2), carbon dioxide (CO_2) and water vapor which change roughly periodically over the respiratory cycle. These ΔB_0 changes can cause fluctuations in the signal that are sufficient to degrade measurements such as BOLD related T_2^* changes, which require very high sensitivity and B_0 homogeneity to capture small signal changes. At high field, respiration has been identified as major source of intensity variation artifacts in functional MRI (fMRI) time series [Van de Moortele 2002].

Intense local susceptibility changes can also arise from foreign paramagnetic and ferromagnetic objects in the body. Metallic implants for example can cause severe ΔB_0 variations and image artifacts. Although some methods have been developed to correct for these ΔB_0 changes [Cho 1988 (VAT), Lu 2009 (SEMAC), Koch 2010], in general these material are not amenable to MRI.

2.3 Susceptibility artifacts

Of the sources of ΔB_0 described above, static susceptibility differences at air, tissue and bone boundaries predominate. The artifacts caused by the susceptibility differences are called '*susceptibility artifacts'*, which in imaging manifest as geometric distortions, intensity variation and signal loss due to intravoxel dephasing of spins and image blurring. The magnetic field variations interfere with the spatial encodings, which are based on the assumption that the static field is perfectly homogenous and the gradient fields are perfectly linear. Magnetic field variations alter the precession frequencies of the

excited spins, affecting slice selection and frequency and phase encoding. This results in mis-registration between actual physical location and image position, producing in-plane shape and slice profile distortions. Geometric distortions also induce image intensity variations by mapping more or less spins into an image voxel. In addition, magnetic field inhomogeneity reduces the effective spin–spin relaxation time T_2 to T_2^* and causes signal loss in gradient recalled echo (GRE) images. There is no such signal loss for spin echo (SE) images due to the π refocusing pulse provided ΔB_0 remains constant with time. Signal losses are worse with increasing echo time (TE) and higher field. Figure 2.1 displays a schematic of the artifacts associated with field inhomogeneity in imaging. The manifestation of ΔB_0 in the form of these image artifacts can be attributed to the Fourier encoding and reconstruction model of MRI. The following paragraphs describe the origin of these artifacts in detail.

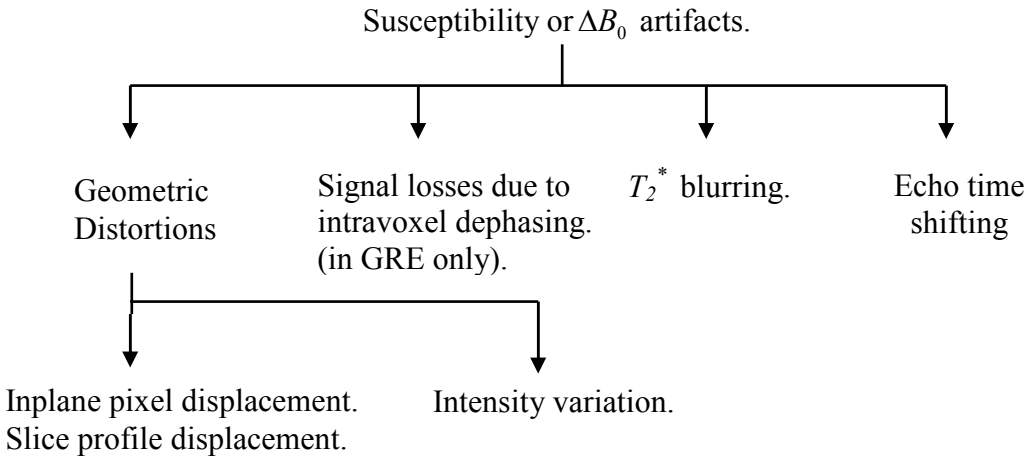

Fig 2.1: Breakdown of susceptibility induced artifacts in imaging.

In a nuclear magnetic resonance (NMR) system, the signal received by a coil from a sample under observation may be expressed after demodulation with ω_0 as

$$S(t) = \int \rho_0(r) e^{-t/T_2(r)} dr^3 \tag{2.4}$$

Where $\rho_0(r)$ is the nuclear spin density in space and $T_2(r)$ is the spatial distribution of the T_2 relaxation time due to spin-spin interactions. The spatial sensitivity variation of the receive coil, diffusion properties of the sample and off resonance conditions are ignored in the above expression. In the presence of the encoding gradients and off resonance (ΔB_0), additional phase is accrued by the spins, the amount of which depends on the strength of the additional field and the time for which they are present. Ignoring T_2 effects, Eq 2.4 can therefore be rewritten for gradient encoded signal from an infinitely thin slice in the *x,y* plane as:

$$S(t) = \iint \rho_0(x,y) \, . e^{-i\gamma (G_x x t_{RO} + G_y y t_{PE})} . e^{-i\gamma (\Delta B_0(x,y) t)} \, dx \, dy \tag{2.5}$$

In the above expression, G_x is the readout field gradient assumed to be along the magnet's *x* axis and G_y is the phase encoding field gradient assumed to be along the *y* axis. The gradient functions in time are assumed to be rectangular. t_{RO} and t_{PE} are the times for which the readout and phase encoding gradients are active. $\Delta B_0(x,y)$ is the off resonance factor in the image plane. During an imaging experiment, the phase accrual due to the gradients is controlled in a predetermined manner to Fourier encode the spins. However, $\Delta B_0(x,y)$ arising from the susceptibility differences imparts phase noise in the signal, giving rise to the image artifacts. The intensity of the artifacts are greatly dependent on the type of pulse sequence used, owing primarily to the relative phase differences accrued over time during repeated excitations which vary with different pulse

sequence schemes. Fast T_2^* based imaging sequences like single shot GRE and SE EPI are particularly sensitive to field inhomogeneities.

2.3.1 Image Distortions

The most readily perceptible artifact caused by ΔB_0 in MRI is image distortion. Image distortion affects both gradient and spin echo images. The amount of distortion varies inversely with the sampling rate (or bandwidth, BW) of the MR signal. For 2D imaging, the field inhomogeneity variations in the slice direction result in slice profile distortions, while inhomogeneities in the plane of the slice cause in-plane distortions.

2.3.1.1 Image distortions in GRE and SE

Consider the simple GRE and SE pulse sequences illustrated in Figure 2.2. TE is the echo time, G_x and G_y represent the readout and phase encode gradients along x and y respectively, $\mathrm{RF}_{\pi/2}$ and RF_{π} represent the $\pi/2$ radiofrequency excitation and π refocusing

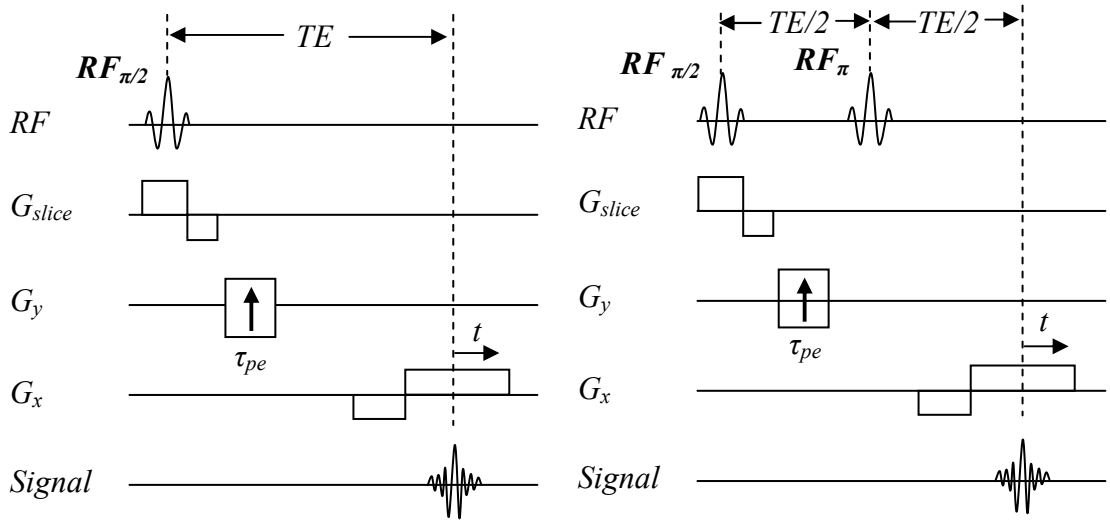

Fig. 2.2 Basic MRI pulse sequences. (a) Gradient Recalled Echo (b) Spin Echo.

pulses. For the spin echo sequence, the RF_{π} pulse lies at TE/2, which refocuses the spins and forms an echo at TE. Let t be the time measured from the center of the positive lobe of readout gradient of length τ_{RO} which coincides with the center of the signal echo. Also, let τ_{pe} be the time for which the phase encoding gradient is active. For the GRE sequence in the presence of ΔB_0, we can rewrite Eq. 2.5 as

$$\begin{aligned} S(t) &= \iint \rho_0(x,y).e^{-i\gamma(G_y y \tau_{PE} + (-G_x)x\frac{\tau_{RO}}{2} + G_x x(\frac{\tau_{RO}}{2}+t))}.e^{-i\gamma(\Delta B_0(x,y)(TE+t))}\,dx\,dy \\ &= \iint \rho_0(x,y).e^{-i\gamma\Delta B_0(x,y)TE}.e^{-i\gamma(G_y y \tau_{PE} + G_x x t)}.e^{-i\gamma\Delta B_0(x,y)t}dx\,dy \\ &= \iint \rho_0(x,y).e^{-i\gamma\Delta B_0(x,y)TE}.e^{-i\gamma(G_y y \tau_{PE} + G_x t[x+\frac{\Delta B_0(x,y)}{G_x}])}dx\,dy \end{aligned} \tag{2.6}$$

From Eq 2.6 it can be seen that according to the Fourier shift theorem, the additional phase produced in the signal by $\Delta B_0(x,y)$ will create a pixel shift in the reconstructed image. A pixel originally at (x, y) will be mapped to (x_1, y_1) in the reconstructed image such that

$$x_1 = x + \frac{\Delta B_0(x,y)}{G_x} \quad ; \quad y_1 = y \tag{2.7}$$

In both GRE and SE images, the in-plane image distortions occur in the frequency encode direction only (in this case, x). The pixel shift is proportional to the field inhomogeneity $\Delta B_0(x,y)$ and inversely proportional to the readout gradient strength G_x. The pixel shift x_1-x may also be written as

$$x_1 - x = \frac{\gamma\,\Delta B_0(x,y).FOV_x}{2\pi.BW_x} \tag{2.8}$$

Where, $FOVx$ and BW_x are the field of view and the sampling bandwidth in the x direction respectively. The pixel displacement is inversely proportional to the sampling bandwidth and directly proportional to the field of view. Therefore, decreasing field of view and/or increasing receive bandwidth will help reduce geometric distortion.

2.3.1.2 Image distortions in Echo Planar Imaging (EPI)

The image distortions in EPI are much more severe than in conventional GRE and SE imaging. In-plane distortions in EPI are seen both in the phase and frequency encode directions, with those along the phase encode direction dominating. Figure 2.3 illustrates the basic EPI sequence. The spatial information is encoded by an alternating frequency encoding gradient in combination with a series of short phase encoding gradient blips.

Let TE be the echo time, Δt_y be the duration of the frequency encode lines (or 'dwell time' in the phase encode direction) and τ_{pe} the time for which each phase

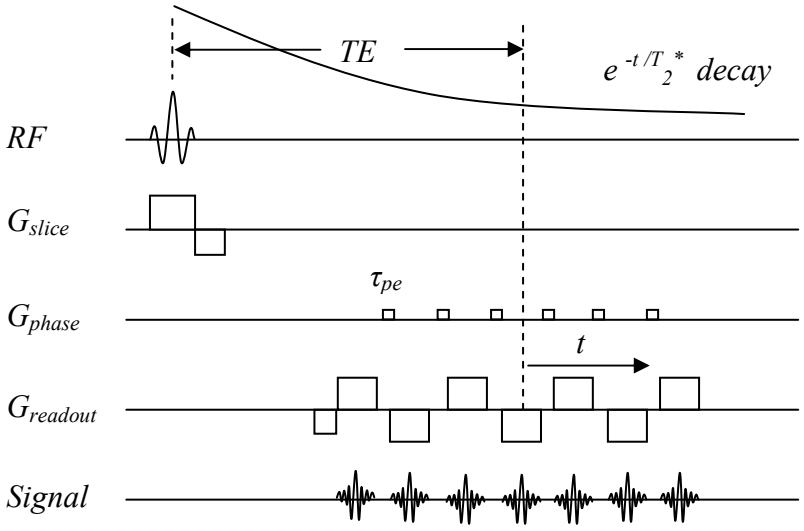

Fig. 2.3 Echo Planar Imaging (EPI) pulse sequence.

encoding blip is active. Therefore, the time at n^{th} readout line and m^{th} sample point is

$$t = TE + n\Delta t_y + m\ \Delta t_x \quad (2.9)$$

The sample numbers, n and m are zero when the phase and readout gradients are zero respectively. Eq. 2.5 can then be rewritten as

$$S(t) = \iint \rho_0(x,y).e^{-i\gamma((-1)^n G_x x m\Delta t_x + G_y y n\tau_{PE})}.e^{-i\gamma(\Delta B_0(x,y)(TE + n\Delta t_y + m\ \Delta t_x))}\,dx\,dy$$

$$= \iint \rho_0(x,y).\ e^{-i\gamma\Delta B_0(x,y)TE}\ e^{-i\gamma(m\Delta t_x G_x[(-1)^n x + \frac{\Delta B_0(x,y)}{G_x}] + G_y n\tau_{PE}[y + \frac{\Delta B_0(x,y)\Delta t_y}{G_y \tau_{PE}}])}\,dx\,dy$$

$$= \iint \rho_0(x,y)\ .\ e^{-i\gamma\Delta B_0(x,y)TE}\ e^{-i\gamma(m\Delta t_x G_x[(-1)^n x + \frac{\Delta B_0(x,y)}{G_x}] + n\Delta t_y G_y^{eff}[y + \frac{\Delta B_0(x,y)}{G_y^{eff}}])}\,dx\,dy \quad (2.10)$$

$$where,\ G_y^{eff} = \frac{G_y \tau_{PE}}{\Delta t_y} \quad (2.11)$$

An additional factor of $(-1)^n$ in the readout direction accounts for the reversing polarity of the gradient for even and odd readout lines, indexed by n. Eq. 2.10 is analogous to Eq. 2.6 giving a convenient formulation to express in-plane distortion in EPI. G_y^{eff} is the effective gradient that would produce the same change in phase by being turned on for Δt_y as G_y would produce in τ_{PE}. In this case a pixel originally at (x, y) will be mapped to (x_1, y_1) in the reconstructed image such that

$$x_1 = (-1)^n x + \frac{\Delta B_0(x,y)}{G_x} \quad ; \quad y_1 = y + \frac{\Delta B_0(x,y)}{G_y^{eff}} \tag{2.12}$$

The distortion in the readout direction here is seen to be similar to the non EPI case apart from the reversing direction as a result of the oscillating readout gradient. However, the distortion in the phase encode direction in this case differs significantly. Typically in EPI, $\tau_{PE} << \Delta t_y$, resulting in a very low value for G_y^{eff}. Therefore, for the same $\Delta B_0(x,y)$ and gradient strength, the pixel displacement in the phase encode direction is much higher than that in the readout direction. As a result, the distortion in EPI is predominantly apparent in the phase encode direction. Also, since the dwell time (Δt_y) in the phase encode direction is large (the bandwidth is small), the distortion produced in EPI in the phase encode direction is significantly higher than that produced in the frequency encode direction in conventional GRE or SE for the same $\Delta B_0(x,y)$.

It can be seen from Eq. 2.12 that for bulk off-resonance where ΔB_0 is independent of *x* and *y*, the pixel displacement is the same for all *x* or *y* which results in a net shift of the image. A linear field gradient in the readout direction causes a diagonal shearing of the image, whereas a linear field gradient in the phase encoding direction causes a compression or expansion of the image in the phase encoding direction. The final distortions depend on the complicated field distributions with respect to the spatial encoding directions.

2.3.1.3 Slice Profile Distortion

The distortion in the slice selection direction is analogous to the in-plane distortion. Figure 2.4 illustrates the distortion in slice selection in the form of the mapping between frequency (ω) and space along the slice selection direction (z). In the presence of ΔB_0 at a position z_1 the spins at that position precess at the frequency ω_z, which is the nominal frequency of spins at the location z. Therefore, an RF pulse intended to excite a slice at location z will excite spins at location z_1 as well.

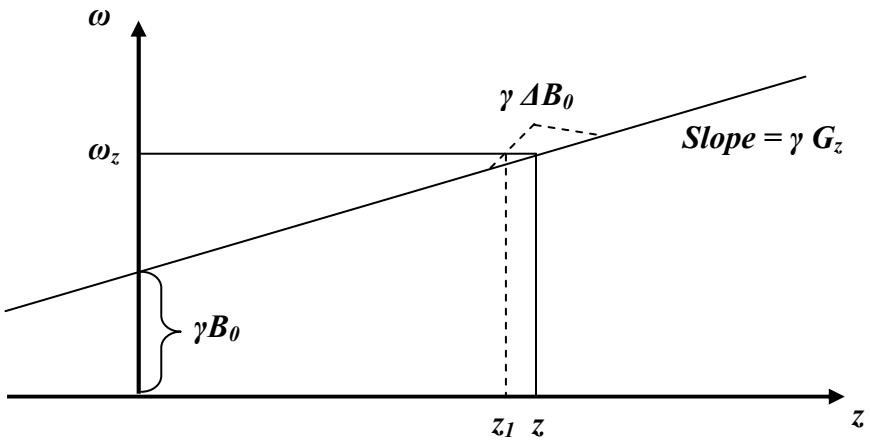

Fig. 2.4 Frequency vs. position mapping, showing effect of local ΔB_0 on slice selection.

Moreover, if ΔB_0 is non zero at location z as well, the slice profile may be significantly distorted. The slice distortion is given by

$$z_1 = z - \frac{\Delta B_0(x, y, z_1)}{Gz} \tag{2.13}$$

where G_z is the slice selection gradient. An ideal slice with a rectangular profile is therefore distorted according to the distribution of ΔB_0. In addition, the thickness of the slice may not be uniform because the magnetic field may vary along the slice as well. A thinner slice region will have fewer excited spins and thus lower signal whereas a thicker region will appear brighter.

2.3.2 Intensity variation

A direct consequence of pixel displacement is the misregistration of signal intensities. Geometric distortion in any spatial encoding direction changes the actual voxel size and may map voxels (or parts of voxels) from different positions into one pixel, thereby creating intensity variations in the image.

Consider the variable substitutions of Eq. 2.12 in Eq. 2.10. If the pixels are shifted to (x_1, y_1) from (x, y) with the transformations being a one to one function of x and y, the substitution of variables make the volume elements of Eq. 2.10,

$$dxdy = J\, dx_1\, dy_1 \tag{2.14}$$

where J is the Jacobian determinant of the transformation

$$\begin{vmatrix} \dfrac{\partial x}{\partial x_1} & \dfrac{\partial x}{\partial y_1} \\ \dfrac{\partial y}{\partial x_1} & \dfrac{\partial y}{\partial y_1} \end{vmatrix} \tag{2.15}$$

The Jacobian is the factor by which the small elemental area $dx_1 dy_1$ local to (x_1, y_1) changes when mapped to (x, y). The presence of the Jacobian allows for the signal intensity modulation due to geometric distortion. These changes in brightness are caused by mapping more or fewer spins into the voxel. The intensity is decreased when signals

from spins are spread out over a larger portion of the image whereas the intensity is increased when the signal from spins are piled up on to a smaller portion of the image.

2.3.3 Intravoxel signal dephasing

A susceptibility artifact that is often more detrimental than image distortions is the signal loss occurring due to dephasing of the spins within a voxel. ΔB_0 gradients inside the voxel cause the spins within a voxel to resonate at different frequencies causing signal to decay faster than when ΔB_0 is absent or when ΔB_0 has zero gradient within the voxel. For a given TE therefore, the spins may be completely dephased in locations of high ΔB_0 gradients before signal acquisition. In the human head for example, the high ΔB_0 gradients around the frontal sinuses and ear canals cause the signals from tissues in areas to completely decay before data acquisition in GRE imaging leading to no information from these areas.

Conventional GRE and SE images suffer from the same distortions for a given ΔB_0 . However, in SE, the spins dephased by ΔB_0 before the RF$_\pi$ pulse are refocused by the pulse. In other words, the phase accrued by the spins due to ΔB_0 before the RF$_\pi$ pulse ($\gamma \Delta B_0 TE/2$) is compensated by the negative phase developed after the pulse ($-\gamma \Delta B_0 TE/2$), since ΔB_0 itself does not change sense after the refocusing pulse[1]. Therefore in SE, the extra phase term of $-\gamma \Delta B_0 TE$ appearing in Eqs. 2.6 and 2.10

[1] Assuming ΔB_0 doesn't change in time and ignoring effects such as motion, diffusion and eddy fields that may introduce phase changes.

representing GRE imaging disappears, leading to recovery of the signal. In the GRE case, this term represents the signal loss due to intravoxel dephasing.

In Eqs. 2.6 and 2.10, ΔB_0 is assumed to be uniform within the voxel. If ΔB_0 is assumed to be linearly changing across a voxel of dimensions $\Delta x, \Delta y \; and \; \Delta z$, the signal magnitude can be written as [Zhao 2005] :

$$|S| = \rho(x,y,z)\Delta x\Delta y\Delta z \; \mathrm{sinc}(\pi TE\,\Delta x\frac{\partial f}{\partial x}) \; \mathrm{sinc}(\pi TE\,\Delta y\frac{\partial f}{\partial y}) \; \mathrm{sinc}(\pi TE\,\Delta z\frac{\partial f}{\partial z}) \quad (2.16)$$

Where $f = f(x,y,z)$ is the frequency at this voxel, $\rho(x,y,z)$ is the spin density. The signal magnitude depends on the voxel size, the local frequency gradient and TE. Commonly in imaging, the slice thickness is larger than the in-plane voxel dimensions. Therefore, the signal loss depends largely on the slice thickness.

2.4 B_0 field mapping

The above sections presented a detailed description of the major artifacts caused by field inhomogeneity. Mapping of the ΔB_0 field is valuable for the correction of these image artifacts, either by prospective or post processing methods. The ΔB_0 fieldmaps can be used in post-processing steps to compute pixel shifts in the image domain and then restore the position to its nominal position on a pixel-by-pixel basis to correct image distortion. Alternatively, fieldmaps may also be used to correct the raw signal prior to reconstruction. Prospectively, fieldmaps can be used to correct ΔB_0 offsets in a process known as shimming, which is a topic of extensive study in this thesis.

2.4.1 Techniques for B_0 field mapping

Several techniques have been developed for mapping ΔB_0. In principle, the estimation of ΔB_0 may be done by the measurement of susceptibility values across the body of interest and using the formulation in Eq 2.2. Several modeling studies have been performed based on this principle with reasonable accuracy of simulated fieldmaps [Bhagwandien 1994, Truong TK 2002, Yoder 2004]. However, very few methods have been actually implemented *in vivo* [Marques 2005]. The reasons for this lie in the difficulties in accurately estimating susceptibility values of complex tissue structures *in vivo* as well as high computation and time requirements. ΔB_0 may also be estimated spatially by a point by point measurement with the use of a single inductive NMR probe as is usually done in the factory setting. This method however is very tedious, error prone and cannot map within samples. The majority of techniques therefore involve estimation of fieldmaps by the measurement of phase evolution within a known period of time.

The first methods for mapping the static field distribution proposed by Maudsley *et al* in 1979 and 1984, were based on chemical shift imaging [Maudsley 1979, 1984]. These methods were time consuming and inefficient as a spectrum had to be collected at each spatial location to derive a single proton field magnitude value. In 1985, Sekihara *et al* introduced a faster method for mapping ΔB_0 in 3 dimensions based on a shifted spin echo method [Sekihara 1985]. This method requires minimal modifications to the standard spin echo sequence, with the addition of a small time delay Δt between the RF_π refocusing pulse and data acquisition. Two images are gathered, one with and one without the modification. The difference between the acquisition times of the modified and the unmodified sequences causes phase shifts between the two images that depend on

ΔB_0. If $I_1(x,y) = \rho(x,y)e^{i\phi_1(x,y)}$ and $I_1(x,y) = \rho(x,y)e^{i\phi_2(x,y)}$ are the two images acquired at the two time points, the phase difference in space $\Delta\phi(x,y)$ may be calculated as

$$\Delta\phi(x,y) = \arctan\left[\frac{\mathrm{Im}\{I_1^*(x,y)\, I_2(x,y)\}}{\mathrm{Re}\{I_1^*(x,y)\, I_2(x,y)\}}\right] \tag{2.17}$$

Where $I_1^*(x,y)$ is the complex conjugate of $I_1(x,y)$, Re{.} and Im{.} are the real and imaginary components of the image. Eq. 2.17 is preferred over subtraction of the individual image phases to find $\Delta\phi(x,y)$, as it is more robust to measurement errors. If Δt is the time difference between the echo times of the two images, then $\Delta B_0(x,y)$ may be estimated as

$$\Delta B_0(x,y) = \frac{\Delta\phi(x,y)}{\gamma\,\Delta t} \quad or \quad \Delta f(x,y) = \frac{\Delta\phi(x,y)}{2\pi\,\Delta t} \tag{2.18}$$

This expression forms the basis for all imaging based field mapping methods, which primarily differ according to the procedure for obtaining $\Delta\phi(x,y)$. The same measurement using the spin ehco sequence may also be performed by shifting the RF_π pulse instead of the data acquisition [Prammer, 1988]. Figure 2.5 shows examples of human head fieldmaps obtained at 7 Tesla using a Δt of 1 ms.

A drawback of the above method is that the field of view over which ΔB_0 is measured often contains more than one chemical shift component whose small (ppm) differences in γ values and hence produce additional phase shifts that are

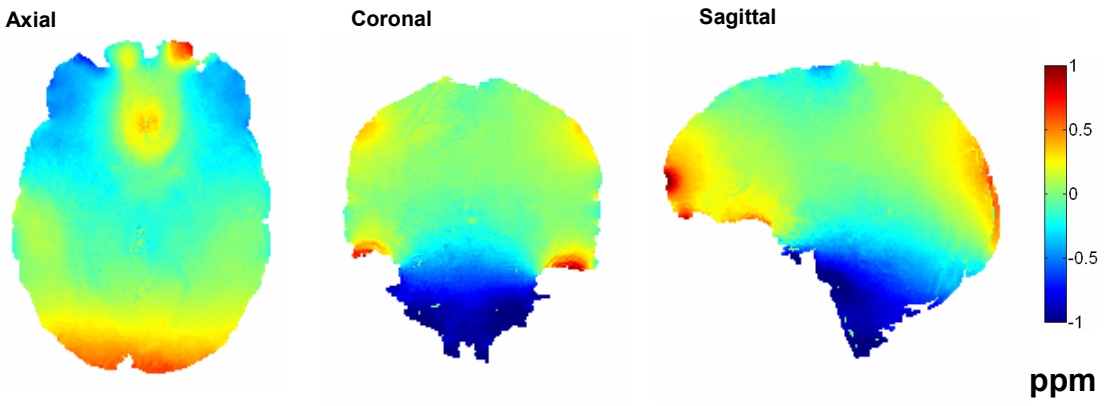

Fig. 2.5 Human brain axial, coronal and sagittal fieldmaps showing field distribution in ppm at 7 Tesla. ΔTE was 1 ms. Field wraps are observed in the inferior regions of the coronal and sagittal slices.

indistinguishable from the phase accrued due to ΔB_0. One example of this is fat and water. In order to estimate the ΔB_0 accurately in these cases, the fat signal has to be suppressed in the fieldmapping procedure. One method for this was proposed by Schneider and Glover in 1991. This method used a faster GRE sequence with similar modification to the SE method. However in this case, the time difference between the two TEs was fixed at $1/\Delta f$ where, Δf was the difference between the resonant frequencies of the two species, specifically fat and water. In this manner, at both TE and TE+Δt, the fat and water signal are in phase, with the only differences arising due to ΔB_0. Considering the difference in resonant frequencies of fat and water to be ~3.5 ppm, Δt for field strengths of 1.5, 3 and 7 Tesla can be estimated to be ~ 4.5 ms, 2.25 ms and 0.97 ms. This method is however limited by the broadness of the fat spectrum and the different T_2^* values of fat and water. In addition, because this is a GRE method, signal losses due to intravoxel dephasing cause the loss of field information in areas of high ΔB_0 gradients. Nevertheless, this method remains one of the most popularly used ΔB_0 mapping methods

today. In all our imaging studies presented in the subsequent chapters, we have utilized this pulse sequence for fieldmapping at 7Tesla. Other variants of the basic method described above include using a spatial spectral pulse to suppress the lipid signal [Webb 1991], using echo planar images to obtain ΔB_0 maps [Reese 1995 Reber 1998] and using a 3 point Dixon acquisition [Glover 1991].

2.4.2 Phase unwrapping

Phase accrued due to ΔB_0 is extracted from the measured complex signal by the inverse tangent function as described previously (Eq. 2.17). The arctan function is uniquely defined only in the principal value range of [$-\pi$ π]. Any absolute phase that is out of this range is "wrapped" into the principal interval, causing a wrapped phase image. For the situation of MRI field mapping, if the ΔB_0 is beyond ±1/(2Δt) in Hz, the phase difference can exceed $\pm\pi$ and result in a wrapped field map (Figure 2.5, coronal and sagittal slices, inferior regions). Therefore, Δt should be small enough such that ±1/(2Δt) covers the entire range of ΔB_0, but big enough to allow detectable phase changes between the two phase images [Glover 1991]. Phase wrap often exists at air/tissue interfaces, where the magnetic field change is dramatic. The wrapped phase $\psi(x, y)$ is related with the unwrapped phase $\varphi(x, y)$ by

$$\psi(x,y) = \phi(x,y) + 2\pi\, k(x,y) \qquad where, \quad -\pi < \psi(x,y) \ \pi \tag{2.19}$$

k(x,y) is a constant that depends on position. A phase unwrapping algorithm tries to identify the points in the phase map at which $\pm 2\pi$ jumps occur and then restores the

original phase with an offset of a multiple of 2π. Phase unwrapping is often complicated by noise in the measured phase map leading to ambiguity in the direction of the field wrap.

2.5. Shimming of the main magnetic field

The previous sections have described the origins, effects and measurement techniques of main magnetic field inhomogeneity. Shimming is the process by which optimum B_0 field homogeneity is obtained over a desired volume by compensating for the field inhomogeneities [Golay 1958, Anderson 1961, Golay 1971, Hoult 2009, Chmurny 1990]. The majority of the work in this thesis involves the investigation of advanced field shimming techniques at high field. The following sections give an overview of shim correction calculation algorithms including a description of field expansion in spherical harmonics, design of shim coils and practical shimming workflow.

A uniform B_0 field is critical for MR imaging and spectroscopy. Typical imaging applications require ΔB_0 variations over the field of view of less than 0.5 ppm (60 Hz at 3 Tesla, 150 Hz at 7 Tesla) to avoid gross distortions and signal losses. In both single voxel spectroscopy and spectroscopic imaging, the requirements are even more stringent. Constraints on the design and manufacture of the main magnet can cause the raw B_0 field homogeneity of a newly designed magnet to be up to a few hundred ppm. Furthermore, any material placed in the bore of a magnet after fabrication can also change the field dramatically relative to the high degree of homogeneity demanded by imaging and spectroscopy. To ‘shim’ the magnet therefore is to reduce the inhomogeneity of raw magnetic field to levels required by NMR and MRI. In the shimming process, the

strength of the magnetic field at every location in the desired 'active volume' of the magnet is mapped and adjusted to reduce the $\Delta B_0(r)$. Shimming is a pre-emptive correction of the magnetic field and is therefore capable of correcting for geometric distortion as well as avoiding intravoxel dephasing. In comparison, post processing methods of image restoration are only capable of correcting for geometric distortion in images, as the signal loss due to intravoxel dephasing is irreversible.

Before the advent of high current density superconductors, most magnets were made of iron. To obtain a homogeneous field, the positions of pole pieces were adjusted with the aid of "shims", a term for thin metal blocks used on machinery to adjust part fitting. This term has carried over to NMR to refer to the adjustments of the magnetic field. Shimming is accomplished in more than one step. First, by placing small ferromagnetic plates or rods at strategic locations within the energized magnet to tune the magnetic field, i.e., *passive shimming,* and second, by adjusting the applied currents through a set of so called electrical shim coils of different configurations to create small fields that either adjust the static magnetic field also called *active shimming*

2.5.1. Passive shimming

Usually performed only during magnet installations and maintenance, passive shimming involves placing small ferromagnetic rods and wedges (also called 'shims') along the sides of the magnet to compensate for field distortions.

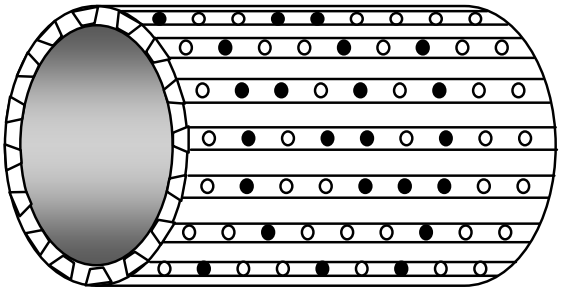

Fig 2.6: Shim inserts in magnet bore indexed locations for passive shimming.

Commonly, steel pieces are placed at a number of indexed positions on rails mounted on the inner surface of the magnet bore. The amount of steel needed in each of these locations is calculated from the measured ΔB_0 map and iteratively optimized. Passive shimming is a laborious and a time intensive process and hence done very infrequently. It corrects for the inherent machine inhomogeneity, but not for subject induced inhomogeneity.

Subject specific passive shimming has also been suggested as a method to optimize subject specific ΔB_0 in addition to active shimming. Passive shim inserts have the capability to produce dipolar high order field gradients, which can significantly counter the rapidly changing roughly dipolar fields encountered in the inferior frontal area of the brain above the oral cavity and the sinuses. Wilson et al in 2002 developed diamagnetic passive shim inserts made of Pyrolytic-graphite that were placed in the mouths of patients and demonstrated significant recovery of signal in the inferior frontal cortex [Wilson 2002, 2003, 2003a]. Others have shown increase in BOLD sensitivity in the orbitofrontal cortex with diamagnetic shim inserts [Cusack 2005]. Passive shim oral inserts have also been made of ferromagnetic materials (Nickel–Iron permalloy) with similar gains in field homogeneity [Juchem 2006]. It has also been demonstrated that passive shimming can be accomplished using combinations of diamagnetic and paramagnetic shim elements. Koch *el at* used diamagnetic bismuth (Bi), paramagnetic zirconium (Zr), and paramagnetic niobium (Nb) on acrylic cone shaped formers on mouse heads, to effectively minimize ΔB_0 in a sample specific manner [Koch 2006a] and more recently this work was extended to humans [Koch 2007a]. Overall, intraoral passive shimming is a promising technique to compensate for rapidly changing B_0 fields

typically seen in the human brain that are not normally corrected by regular *active shimming* methods.

2.5.2. Active shimming

In active shimming, the magnetic field is adjusted with the use of orthogonal spatial correction 'shim fields' produced by current carrying shim coils. The shim coils are placed in the bore, coaxially with the gradient coils and are operated by dedicated power supplies. The strengths of the spatially varying field produced are proportional to the current in the coils. The spatially varying fields and thereby the shim coils are generally categorized by the 'order' of their spatial variation. The gradients for example are linear fields and therefore 1^{st} order. The actively driven shim coils can be either superconductive or resistive. Superconductive shims are fitted within the cryostat and are generally optimized only during magnet construction. They reduce the level of inhomogeneity of a passively shimming magnet to the order of a few ppm. Resistive shim coils are installed separately in the bore and are at room temperature. These shim coils target subject specific inhomogeneities and are tunable by the user.

Most clinical scanners possess up to 2^{nd} order shims that are generally referred to by their common names based on the description of the field produced in cartesian coordinates (**Z2, ZX, ZY, X2-Y2, XY**). Some clinical scanners as well as animal systems also posses 3^{rd} order shims that produce fields with 3^{rd} order spatial dependence (**Z3, Z2X, Z2Y, Z(X2-Y2), ZXY,X3, Y3**). Some magnets, for example certain high resolution NMR spectroscopy systems may have even higher order shim coils. (**Z4, Z5** etc).

To calculate the currents required in the individual shim coils for field correction, the existing magnetic field in the bore must be decomposed into the spatial field variation components represented by the shims. The following sections introduce the mathematical framework for shimming.

2.5.3 Shim Theory

As introduced above, shimming is the process of minimizing the field offsets within the target volume of the magnet. If $B_0(x,y,z)$ is the actual field distribution, the ultimate aim of shimming is to eliminate the spatial dependency of $B_0(x,y,z)$ so as to reduce the field to a constant B_0^C independent of location. Therefore, the process of shimming may be expressed as finding the solution to the multiple linear equation

$$B_0^C = B_0(x,y,z) + \sum_i c_i S_i(x,y,z)$$

$$or \quad \Delta B_0(x,y,z) = B_0(x,y,z) - B_0^C = -\sum_i c_i S_i(x,y,z) \tag{2.20}$$

Where $S_i(x,y,z)$ represent the spatial distributions of the magnetic correction fields used for compensation and c_i are their weights. In active shimming, these spatial distributions modeled by spherical harmonics are produced by discrete actively driven shim coils with currents proportional to c_i. Typically, due to hardware constraints in MRI systems, shim coils produce up to 3rd order spatial harmonics limiting the degree of correction practically achievable.

The equation that governs the behavior of the field in the bore of a superconducting magnet is Laplace's equation :

$$\left\{\frac{\partial^2}{\partial x^2} + \frac{\partial^2}{\partial y^2} + \frac{\partial^2}{\partial z^2}\right\} B_0 = 0 \quad or \quad \nabla^2 B_0 = 0 \tag{2.21}$$

In NMR and MRI, we assume that the field variation is less than 100 ppm at all locations. Considering this high degree of accuracy in the magnetic field, it can be assumed that field is unidirectional, (i.e. along the bore/long axis of the magnet) at all locations. For MRI magnets, this is assumed to be the '*z*' direction. From Eqs. 2.20 and 2.21, it is apparent that the solution to the shimming problem in Eq. 2.20 may be obtained by solving Eq 2.21 to obtain $S_i(x, y, z)$ and c_i .

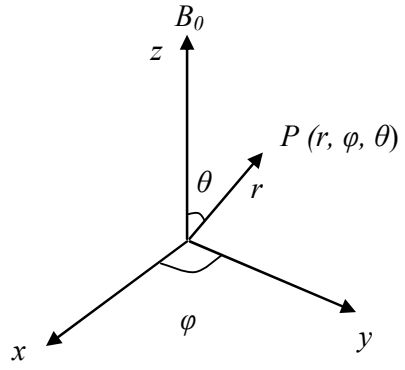

Fig. 2.7 Cartesian (x, y, z) and spherical polar coordinates (r, θ, φ). The main field B_0 is assumed to be aligned along the z axis.

We assume a coordinate system for shim analysis such that the main magnetic field aligns along the *z* axis as shown in Figure 2.7 The most common way of solving for Eq. 2.21 is to use spherical coordinates radius '*r*', declination '*θ*' and azimuth '*φ*'.

The solution for Eq 2.21 is standard and is given as:

$$B_{0_{nm}}(r,\theta,\varphi) = \sum_{n=0}^{\infty}\sum_{m=0}^{n} C_{nm} r^n P_{nm}(\cos\theta)\cos[m(\varphi - \psi_{nm})] \tag{2.22}$$

Here, the product $P_{nm}(\cos\theta)\cos[m(\varphi-\psi_{nm})]$ is the spherical harmonic of the n^{th} order and m^{th} degree. $C_{n,m}$ and $\psi_{n,m}$ are constants representing the weights and spatial phases of the harmonics. $P_{n,m}(cos\theta)$ are polynomials in $\cos\theta$, also called Ferrer's associated Legendre functions where n and m are integers such that $n \geq m \geq 0$. $P_{n,m}(cos\theta)$ is defined as :

$$P_{nm}(\cos\theta) = \frac{(-1)^m}{2^n\, n!}(1-\cos^2\theta)^{\frac{m}{2}}\frac{d^{n+m}}{d\cos^{n+m}\theta}(\cos^2\theta-1)^n \qquad (2.23)$$

As seen in Eq 2.22, the magnetic field can be expressed as a linear combination of an infinite number of products of spherical harmonics and powers of distance r. The lowest order spherical harmonic with $n = 0$, $m = 0$ may be expressed as a constant which is equal to the sum of the nominal constant magnetic field B_0^C and a constant term C that accounts for any field offset existing in practice. Eq. 2.22 may therefore be written as

$$B_{0_{nm}}(r,\theta,\varphi) = B_0^C + C + \sum_{n=1}^{\infty}\sum_{m=0}^{n} C_{nm} r^n P_{nm}(\cos\theta)\cos[m(\varphi-\psi_{nm})] \qquad (2.24)$$

From Eq 2.20 and 2.24, we can write the field inhomogeneity as

$$\Delta B_0(r,\theta,\varphi) = C + \sum_{n=1}^{\infty}\sum_{m=0}^{n} C_{nm} r^n P_{nm}(\cos\theta)\cos[m(\varphi-\psi_{nm})] \qquad (2.25)$$

With the fieldmapping methods described in the previous section one can map $\Delta B_0(x,y,z)$ or $\Delta B_0(r,\theta,\varphi)$. Shimming is then simply the process of multiple linear

regression to find the coefficients C_{nm} that are nothing but the 'shim coefficients' in units of *Field/Distance*^{n}.

From Eq.2.22, it is also observed that when $m = 0$, the field has complete cylindrical symmetry. All variation of B_0 with φ disappears as the final cosine term is unity. The resulting functions are called the *zonal harmonics*, given by

$$B_{0zonql} = \sum_{n=0}^{\infty} C_{n0} r^n P_{nm}(\cos\theta) \tag{2.26}$$

When m ≠ 0, the spherical harmonic fields oscillate as we move around in a circle about the *z* axis with frequencies mφ, producing what are known as the *tesseral harmonics.*

It should be noted that each harmonic has a particular phase, defined by the factor $m\psi_{n,m}$ which essentially defines the rotation about the *z* axis for the tesseral harmonic. For complete field cancellation, it is required to adjust the amplitude as well as phase of the harmonics. We may write the cosine term from Eq 2.22 as

$$\cos[m(\varphi - \psi_{nm})] = \cos(m\varphi)\cos(m\psi_{nm}) + \sin(m\varphi)\sin(m\psi_{nm}) \tag{2.27}$$

which implies that the spherical harmonic with order *n* and degree *m* may be expressed as a linear combination of two complimentary components. Because the tesseral harmonics have amplitude and phase, any shim coil system must be either physically rotatable about the *z* axis or else duplicated by another shim set $\pi/2m$ radians displaced from the first. Typically, manufacturers provide a complimentary phase shim coil (*cosine or sine*), with

which both the amplitude and phase can be cancelled as physically rotating individual coils is difficult. These two components are often indicated as *nm* and *nm'*. Some texts refer to only the zonal coefficients as C_n and the *sin(mφ)* and co*sine(mφ)* tesseral components as A_{nm} and $B_{nm.}$ Table 2.1 gives the complete spherical harmonic functions and representation up the 3rd order.

2.5.4. Shim coils

Shim coils are composed of current carrying loops and arcs connected in series in such a way as to produce a desired specific spherical harmonic in the target space of the

n	m	Shim Name	Cartesian Form	$P_{nm}(\cos\theta)$	Full Spherical Form $S_{nm}(\theta, \varphi)$
1	0	Z	z	$\cos\theta$	$\cos\theta$
1	1	X	x	$\sin\theta$	$\sin\theta\cos\varphi$
1	1	Y	y	$\sin\theta$	$\sin\theta\sin\varphi$
2	0	Z2	z2 - (x2 + y2)/2	$(3\cos^2\theta - 1)/2$	$(3\cos^2\theta - 1)/2$
2	1	ZX	zx	$\sin\theta\cos\theta$	$\sin\theta\cos\theta\cos\varphi$
2	1	ZY	zy	$\sin\theta\cos\theta$	$\sin\theta\cos\theta\sin\varphi$
2	2	X2-Y2	x2-y2	$\sin^2\theta$	$\sin^2\theta\cos 2\varphi$
2	2	2XY	2xy	$\sin^2\theta$	$\sin^2\theta\sin 2\varphi$
3	0	Z3	z[z2 - 3(x2 + y2)/2]	$(5\cos^3\theta - 3\cos\theta)/2$	$(5\cos^3\theta - 3\cos\theta)/2$
3	1	Z2X	x(4z2 - x2 - y2)	$\sin\theta(5\cos^2\theta - 1)$	$\sin\theta(5\cos^2\theta - 1)\cos\varphi$
3	1	Z2Y	y(4z2 - x2 - y2)	$\sin\theta(5\cos^2\theta - 1)$	$\sin\theta(5\cos^2\theta - 1)\sin\varphi$
3	2	Z(X2-Y2)	z(x2 - y2)	$\sin^2\theta\cos\theta$	$\sin^2\theta\cos\theta\cos 2\varphi$
3	2	XYZ	2xyz	$\sin^2\theta\cos\theta$	$\sin^2\theta\cos\theta\sin 2\varphi$
3	3	X3	x3 - 3xy2	$\sin^3\theta$	$\sin^3\theta\cos 3\varphi$
3	3	Y3	3x2y - y3	$\sin^3\theta$	$\sin^3\theta\sin 3\varphi$

Table 2.1: Shim spherical harmonics in cartesian and spherical harmonics.

magnet. The current in the coils is proportional to the coefficients of the individual spherical harmonic coefficients (C_{nm}) obtained from the shim regression process. The

coils are generally referred to by their common name, which is cartesian coordinate based, as given in Table 2.1. For example, the zonal shim coils upto 2rd order are *Z0, Z, Z2* while the tesseral coils are *XY, X2-Y2, ZX* and *ZY*. The first order shim harmonics *X, Y* and *Z* are usually generated by the scanner's gradient coils while the other harmonics have dedicated coils, amplifiers and a control unit that communicates with the spectrometer.

In general, fields produced by current loops contain an infinite number of spherical harmonics. The art behind the design of shim coils lies in combining these individual coil elements to produce the desired pure harmonic. Romeo and Hoult showed that in order to produce an *n, m* harmonic, coil elements can be arranged geometrically in such a way that all orders *n* and degrees *m* less than that desired are nulled while as many of the higher orders and degrees are minimized or eliminated [Romeo 1984]. Zonal shims like Z, Z2 Z3 etc for example, employ combinations of circular coils with symmetric and antisymmetric current flow directions and optimized intercoil distances to cancel out unwanted harmonics (Helmholtz/ Maxwell configurations). Tesseral shim coils employ a cylindrical design with circular end arcs (Golay saddle configuration). The coils are constructed on cylindrical formers placed between the imaging gradient former and magnet heat shields. Figure 2.8 shows examples of traditional coil layouts of zonal and tesseral shims. More recently, distributed wire pattern generation techniques based on target field [Turner 1986] and stream function [Forbes 2001, 2002, 2003] methods have been employed to produce the spherical harmonics. These techniques offer much higher control over the optimization of shim strengths, power utlization and impedance. In spite of best efforts however, there always remains some amount of lower or higher

impurity in the harmonics produced. For example, a Z2 shim coil often has some residual Z0 impurity. This effect has to be taken into account in any shimming procedure.

Generally, the higher the number of shims available in the system, the better the field homogeneity achievable. Having more shims however can make the shimming process quite complicated. A constraining factor in the performance of shim coils is the current limit of the shim power supply as the strength of the field produced depends

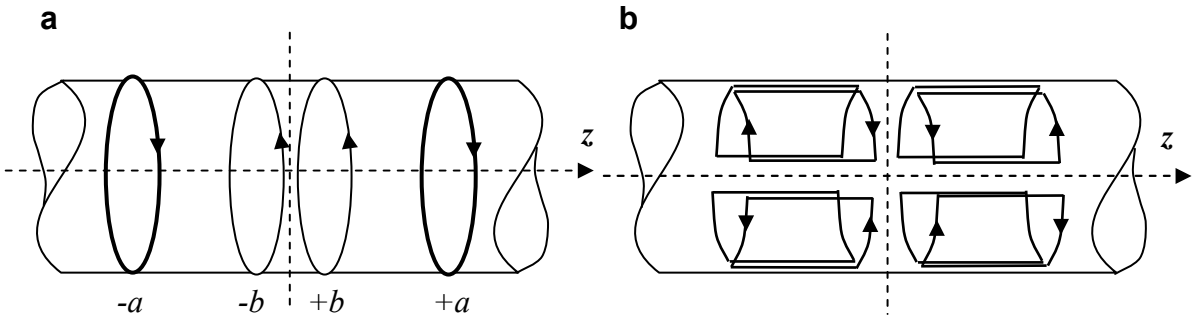

Fig. 2.8 Basic Zonal and Tesseral shim coil designs.(a) A zonal Z2 shim coil based on a basic 2 Helmholtz pair configuration (b) Tesseral X2-Y2 shim coil based on the Golay saddle configuration.

directly on the amount of current in the shim coils. Also, the shim coils are usually placed outside the gradient former in the bore of the scanner, quite far from the sample to be shimmed. The field produced at a distance r by a current loop carrying current I has been shown to be proportional to I/r^{n+1}, where n is the order of the shim [Romeo 1984]. The loop current I is limited by the number of turns and therefore available bore space. For this reason it remains difficult to produce strong 3rd and higher order fields in large bore clinical systems. One of the approaches to tackle this problem is the use of shoulder slotted shim coils, which bring the shim coils close to the subjects head [Poole 2008a]. The inductance of the shim coil is also important in shim performance. The higher the

inductance, the slower is the rate of shim current change, a property that is crucial in applications that require rapid switching of shims. The inductance is hence always included as a coil design parameter.

It should be noted that the orthogonality of the spherical harmonics given by Eq. 2.22 is valid only over a spherical volume of interest, encountered in traditional cylindrical bore magnets. MR magnets with geometries other than cylinders, such as open magnets, asymmetric magnets (homogeneous region placed close to one end of a magnet), which are designed for easy patient access, and magnets dedicated to image specific body parts, use the target field and stream function methods to design the shim system.

Recently, active shim coil oral inserts have also been shown to reduce ΔB_0 in the inferior temporal cortex [Hsu 2005]. This insert contains three current loops individually adjustable to shape the local field in a subject specific basis. Patient comfort is however an issue with active local shim coils.

2.5.5. Shimming Techniques

Shimming techniques are primarily of two types, manual and automatic. Both techniques first obtain an estimate of the field inhomogeneity, either in the form of a free induction decay (FID) curve or as a fieldmap. Following that, individual shims are either manually or automatically adjusted to optimize ΔB_0 .

2.5.5.1 Manual shimming

In manual FID shimming, the operator seeks to maximize the area under the FID curve or in other words, minimize the width of the water spectrum peak after a single 90^o

pulse by individually adjusting the shim channels. When the area under the FID is maximum, the signal from the shimmed volume is being generated by a very narrow range of off-resonant spins, thereby minimizing ΔB_0. Manual shimming is the traditional approach to shimming and is present on most scanners, although not very often used in human imaging scans owing to time constraints. Although experienced users can decipher the shim channel needing adjustment from the shape of the FID or the water peak, getting stuck in a local minimum is a common occurrence. In practice, FID shimming can be quite laborious and can require large amounts of time to obtain optimal field homogeneity. Often adjustment of one shim channel causes other harmonics to be produced due to non-orthogonal imperfections of the shim channels leading to false optimums. For this reason manual shimming has to be performed in an iterative manner, starting from the higher order shims that generally have higher cross talk going down to the first and zeroth order fields. This can take up precious scanner time and is therefore generally avoided in human scans. Also, FID shimming optimizes the field over a whole volume, providing little information about the local field distributions.

For these reasons, automatic shimming, in which the shim coils are set automatically, is the preferred way of shimming. Introduced by Prammer et al in 1988, automatic shimming seeks to minimize ΔB_0 extracted from fieldmaps by calculating the spherical harmonics and adjusting the shim coils all at once [Prammer 1988]. Automatic shimming is usually performed as a pre-scan stage and the shim values set for the entire duration of the scan. There are two major types of automatic shimming that essentially differ in their measurement of ΔB_0, fieldmap based and projection based automatic shimming.

2.5.5.2 Automatic projection based shimming (FASTMAP)

Projection based shimming is a rapid shimming procedure based on the argument that C_{nm} over a volume can be uniquely determined by using information from a set of carefully chosen linear fieldmap projections in the volume [Gruetter 1992, 1993]. The projections are generally acquired using reduced field of view techniques such as STEAM [Frahm 1985] or PRESS [Bottomley 1984]. Field information along the projections is extracted from repeated acquisitions having a time delay between the first and second RF pulse of a STEAM sequence. Essentially, if the relative contributions of the individual spherical harmonics to the field along the selected projections are known, one can regress for the actual strength of a harmonic based on the data from all the projections.

If we let the spherical harmonic term $P_{nm}(\cos\theta)\cos[m(\varphi-\psi_{nm})]$ be identified as W_{nm} then neglecting the constant term C that can be set to zero by adjusting the center frequency setting, Eq. 2.25 for the field along a projection j that runs through the center of the coordinate system may be written as

$$\Delta B_0^j(r,\theta,\varphi) \quad = \quad \sum_{n=1}^{\infty} r^n \sum_{m=0}^{n} C_{nm} W_{nm}^j \tag{2.28}$$

where $W_{nm}^j \equiv W_{nm}[\theta^j, \varphi^j]$ is a constant along the projection j and describes the contribution of spherical harmonic W_{nm} to the field along the projection j. W_{nm}^j can be calculated very simply from the polar formulations of W_{nm} . For instance, for j along the x

axis, the inclination θ is 90^o and the azimuth φ is 0^o. From Table 2.1 is can be seen that the relative contributions of the 1st order fields to the field along this projection are

$$\begin{aligned} Z &= W_{10}^{(90,0)} = Cos(90) = 0 \\ X &= W_{11}^{(90,0)} = Sin(90)Cos(0) = 1 \\ Y &= W_{11}^{(90,0)} = Sin(90)Sin(0) = 0 \end{aligned} \tag{2.29}$$

Once $\Delta B_0^j(r,\theta,\varphi)$ has been measured along a projection, a polynomial regression to the n^{th} degree yields the yields the coefficients a_n^j such that

$$\Delta B_0^j = a_0^j + a_1^j r + a_2^j r^2 \ldots . a_n^j r^n \tag{2.30}$$

The polynomial coefficient a_n^j is an estimate of the sum of all the harmonics of n^{th} order along that *j*. Therefore, minimizing the expression

$$\sum_{m=0}^{n} C_{nm} W_{nm}^j - a_n^j \tag{2.31}$$

with respect to C_{nm} in a least squares sense for each *n* gives the solution for the shimming problem. When the orientation of the projections is chosen such that

$$\sum_j W_{na}^j W_{nb}^j \begin{array}{l} = 0 \ for \ a \neq b \\ > 1 \ for \ a = b \end{array} \tag{2.32}$$

a simple solution to the minimization can be written as

$$C_{nm} = \frac{\sum_j a_n^j W_{nm}^j}{\sum_j (W_{nm}^j)^2} \tag{2.33}$$

Since W_{nm}^j can be obtained very easily for defined j, the shim solution can be obtained simply by linear combinations of a_n^j. To determine the first order shim setting, projections along the three main axes *x* (90,0), *y* (90,90) and *z* (0) are necessary. 6

orthogonal projections, *xy* (90,-45), *yx* (90, -135), *zx* (45,0), *xz* (45,180), *zy* (45, -90), *yz* (45,90) are used to determine all first and second order shim settings.

The main advantage of this method, also called FASTMAP (Fast Automatic Shimming Technique by Mapping Along Projections) is that field can be optimized very quickly, since the projections do not require phase encoding. Some improved variants of FASTMAP include FASTERMAP which uses a semi adiabatic spin echo sequence for improved signal [Shen 1997] , FASTESTMAP which reduced the time taken by using an asymmetric echo planar readout gradient train [Greuetter 2000] and FLATNESS, which attempts to apply the method in slice shimming [Shen 1999]. Projection based methods generally work well over reasonably homogeneous volumes with moderately uniform field changes. They can therefore be used reliably for applications probing small volumes like single voxel spectroscopy. For larger volumes like the human brain in entirety and the body where more than one resonance may be present or where the fields change rapidly, these methods often fall short. Fieldmap based methods are much better suited in those cases.

2.5.5.3 Automatic fieldmap based shimming

In fieldmap based shimming, shim values are obtained from the multiple linear regression of 2D or 3D ΔB_0 maps acquired using one of the methods described in section 2.4. The GRE based method of Glover *et al*. [Glover 1991] remains a very popular method for fieldmapping. The fieldmaps are generally thresholded based on the accompanying magnitude image to extract the field information from a desired shim region of interest (ROI). Several different cost functions have been investigated for the

minimization procedure including least squares error [Prammer 1988, Glover 1991, Webb 1991], the maximum field deviation [Prammer 1988] and the sum of the intravoxel gradients in the ROI [Wen 1995]. Of the above functions, the least squares error is the most frequently used.

One of the advantages of fieldmap based shimming is its flexibility to arbitrary shaped ROIs. Also, fieldmap based methods have a higher immunity to signal voids than projection based methods. On the flipside, there exists a time penalty for fieldmap based shimming as an extra fieldmapping scan has to be performed before the imaging scan. Errors can also be introduced due to motion of the subject between the fieldmapping and the actual scan. In addition, it is difficult to obtain fieldmaps during the actual scan to track dynamic field deviations due to time constrains. EPI and spiral acquisition based rapid fieldmapping [Kim 2002, Reber 1998, Reese 1995] techniques have been used for shimming, although these methods suffer from additional imaging artifacts in the fieldmap (distortions, T_2* blurring) due to the interaction of the lower bandwidths and ΔB_0 itself.

Shimming is usually performed as a scan preparation stage. Shim coefficients calculated from the regression are converted into current values and communicated to the shim power supply unit prior to the actual scan. Usually, only a single set of shim values are produced which minimizes the ΔB_0 variation over the entire target volume. For small volumes, this single 'global' shim setting can homogenize the field sufficiently for most applications. The approach can however be inadequate for shimming over extended volumes, for example the whole brain or multiple slice stacks in whole-body imaging where ΔB_0 varies considerably across the volume. Applications such as DTI in the brain,

data driven functional MRI, brain connectivity studies among others require maximal brain coverage, where a single shim set usually does not suffice. One approach of attaining higher local field homogeneity over extended volumes is dynamic shimming, a subject of extensive discussion in this thesis.

2.6. Dynamic Shimming

For shimming over extended volumes or volumes over which the ΔB_0 profile changes rapidly, the traditional global shimming method in which only one shim set is applied for the whole volume can be modified to dynamically update the shim settings. Dynamic shimming is a technique in which the shim settings can be changed during the acquisition of data from multiple slices or sub-volumes. Therefore, multiple shim settings optimal for each slice or sub-volume can be applied during a single experiment, leading to better localized compensation of field inhomogeneities than is obtainable using a single global shim set. Figure 2.9 illustrates the concept of dynamic shimming in comparison to traditional global shimming.

In spite of the relative simplicity of the idea behind dynamic shimming, the technique has not seen widespread use in commercial scanners. The reason behind this is that dynamic shimming relies on the ability to change shim settings rapidly during a scan. On most scanners, only the first order shims controlled by the imaging gradients can be switched dynamically and reliably during acquisition. Unlike the gradients, shim coils are usually driven by low bandwidth amplifiers using slow asynchronous serial communication channels with the spectrometer making it difficult to precisely update shim values during the scan. Shim amplifiers also have long settling times that may be up

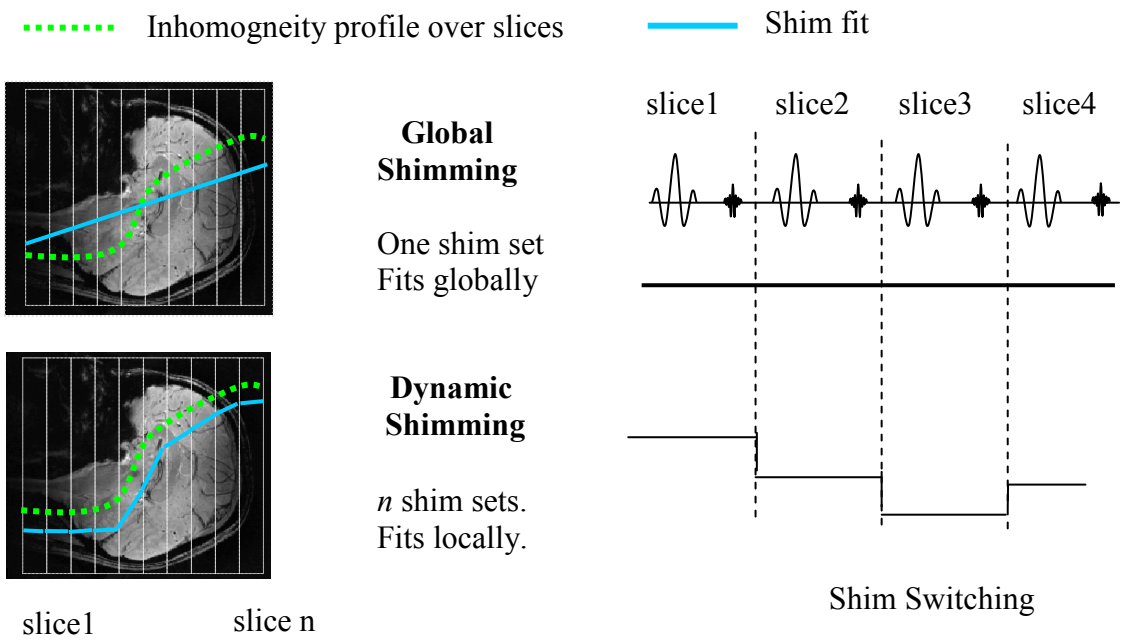

Fig. 2.9 Dynamic Vs Global Shimming.

to 5 ms depending on the impedance of the connected shim coils [RRI specification sheet]. In addition, most commercially available scanner software does not include full control of the shim waveforms. Moreover, most shim coils are unshielded and can cause severe eddy currents when switched rapidly, degrading image quality. These technical challenges have hindered the widespread use of dynamic B_0 shimming. One of the approaches taken to circumvent these hardware bottlenecks has been to introduce an additional shim control unit that can supply shim currents according to preloaded dynamic correction values during the scan. Typically, this module is synchronized with the pulse sequence with the use of pulse triggers generated by the spectrometer at appropriate times.

Various groups have demonstrated the potential benefits of dynamic shimming vis-à-vis traditional global static shimming. A slice-wise dynamic shimming method in

which the optimal first order shim currents were updated for every slice in a multislice acquisition at 2.1 Tesla was first proposed by Blamire *et al* in 1996. [Blamire 1996] shortly followed by Morrell and Spielman at 1.5 Tesla [Morell 1997]. Dynamic shimming was extended to 2nd order at 4 Tesla by de Graaf *et al* in 2003 where the Z0 eddy field produced by rapid switching of the Z2 shim was characterized and compensated using a multiple time constant compensation circuit [deGraaf 2003] . This work was extended by Koch *et al* in 2006 to include all the 2nd order shims [Koch 2006,2007] . Field homogeneity improvements were demonstrated in multislice whole brain imaging, multivoxel spectroscopy and multislice spectroscopic imaging. All of the above studies made use of an external hardware unit to store and dynamically update the shim currents. Zhao et al. simulated DS up to 3rd order and showed that DS can yield better optimized field homogeneity than GS [Zhao 2005].

This thesis presents the first implementation of slicewise dynamic shimming at 7 Tesla. Chapter 3 discusses the implementation while Chapter 4 presents the results of comparison to static global shimming. Other issues such as shim induced eddy currents, shim switching strategies and relative benefits of higher order shimming have also been examined. Henceforth, we will refer to dynamic shimming simply as '**DS**' and global static shimming as '**GS**' for brevity.

2.7. Eddy Currents

In MRI, eddy currents are induced in the conducting structures of the magnet assembly by the rapid switching of magnetic fields which are either in the form of gradients or shims. These conducting structures include the heat shields in the dewar

holding the superconducting magnet, magnet supports, magnet cryostat and radio frequency shields. The eddy fields generated in the bore by the eddy currents oppose the primary field (Lenz's law) thereby increasing their rise time and introducing errors in the gradient performance. In dynamic shimming, shim fields are changed rapidly in synchronization with the scan sequence. These changing shim fields induce eddy currents in the bore of the magnet that in turn produce eddy fields. These fields can severely compromise both imaging and spectroscopy using dynamic shims. The effects, measurement and compensation of eddy currents associated with dynamic shimming are topics discussed in detail in chapter 3 and 4 of this thesis.

The eddy fields are time varying and usually decay with multiple time constants that can range from 0.1 up to 1000s of milliseconds [Jensen 1987,Morich 1988, Boesch 1991, Robertson 1992]. Generally, eddy fields are characterized as 3 or 4 exponentially decaying components with, *short* (0.1 – 10 ms), *medium* (10 – 100 ms) and *long* (100 – 1000s of ms) time constants. The decay times of the fields depend on the particular magnet structure in which the eddy currents flow. Generally, the colder the structure, the more slowly decaying are the eddy currents owing to lower resistances. If left uncompensated, eddy currents can severely hamper performance in both spectroscopy and imaging. In general, the shorter the switching time of the gradients, the more severe are the eddy currents. Therefore, eddy currents can be extremely problematic in sequences requiring rapid switching of gradients such as EPI, those requiring large and precisely matched gradient pulses as in diffusion weighted imaging (DWI) or in dynamic shimming.

The time varying magnetic fields can be of the same harmonic as the switched field as well as other cross terms. As a result, they can produce a variety of artifacts in imaging including ghosting, distortions and blurring. In addition to introducing B_0 offsets that result in phase ramps in *k* space that lead to bulk image shifts, linear gradient induced eddy currents can skew (eddy current field gradient along the readout direction) or compress (eddy current field gradient along the phase encode direction) *k* space sampling, as shown in Figure 2.10. This *k* space distortion results in corresponding distortions in image space. Higher order eddy currents that can be induced by shim switching may distort *k* space sampling even more nonlinearly. In EPI, gradient induced eddy fields can cause inconsistencies between odd and even echoes in *k* space. These fields add to or subtract from the ideal gradient fields and cause echo time shifts that alternate in the odd and even lines. These give rise to characteristic *N/2* ghosts, which are essentially low intensity ghosts of the image at $x = \pm N/2$ displaced from the center of the

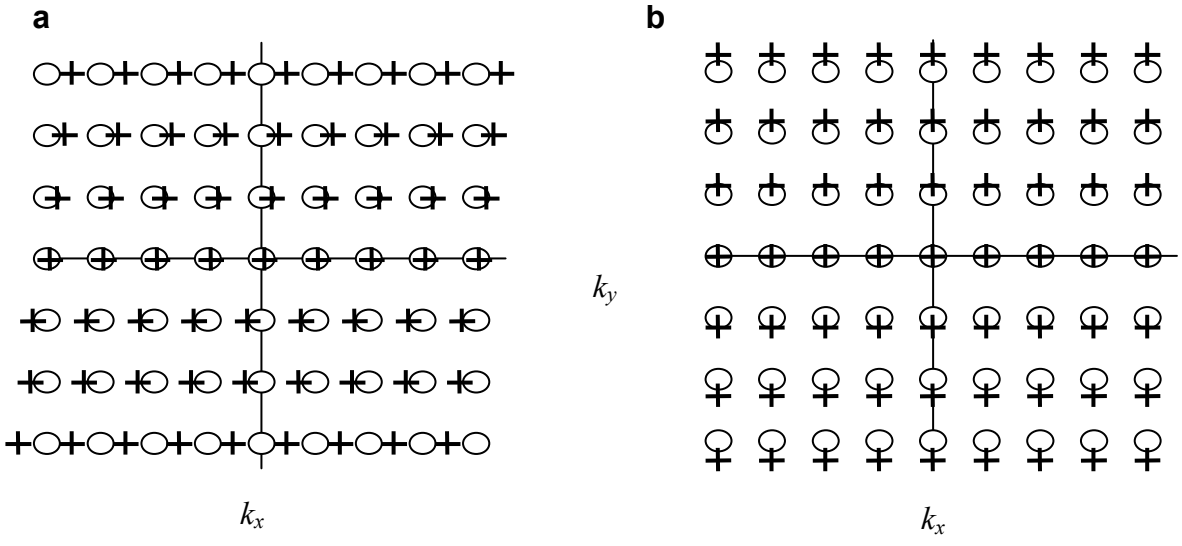

Fig. 2.10 K space distortions caused by eddy current induced field gradients (a) Eddy field gradient in the readout (k_x) direction causing shearing of k space. (b) Eddy field gradient in the phase encode (k_y) direction causing stretching of k space. Circles represent the correct sampling positions, plusses represent the actual positions.

image, where N is the number of pixels and x is the position along the phase encode direction. Higher order shim induced eddy fields can create more complicated ghosting patterns.

2.7.1 Eddy current compensation techniques

Traditionally, compensation of eddy currents produced by the gradients has been performed by a combination of two approaches. The first approach involves pre-shaping the gradient input waveform by the addition of several (typically 3 or 4) compensating waveforms representing the exponential components of the measured eddy field, so that the final waveform produced in the scanner follows the ideal profile [Glover Patent 1987, Jensen 1987]. The compensating waveforms are generated using a series of RC circuits that feed into the gradient amplifier. The second approach aims to reduce the production of eddy currents themselves by shielding the gradient coil to minimize the magnetic coupling between the coil and the metallic structures in magnet [Mansfield 1986, Turner 1986a]. In this method, the gradient coil is composed of two separate components, an inner coil that produces the gradient field and an outer concentric 'shield' coil which is specifically designed to cancel the field produced by the primary coil outside the shield. This shielding may be either 'passive' in the form of a concentric conductive tube [Turner 1986a] or 'active' in the form of a current driven coil [Mansfield 1986, Bowtell 1991]. The gradient and the shield coil are usually supplied by a single power supply. Figure 2.11 illustrates the standard gradient waveform shaping circuit (a) and gradient coil shielding (b).

Both of the approaches to combating eddy currents have drawbacks. The current waveform method requires overdriving the gradient amplifiers, especially to compensate

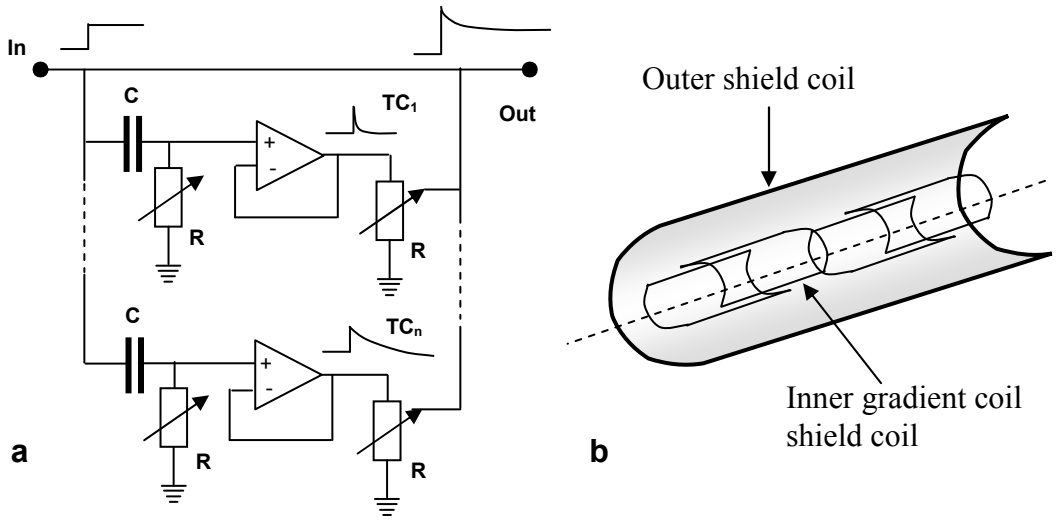

Fig. 2.11 Eddy current compensation by (a) Gradient waveform shaping 'pre-emphasis' network and (b) Gradient coil shielding.

the low time constant eddy fields (due to an initial spike in current demand) leading to increased voltage demands. Also, the spatial variation of the induced eddy field is often not exactly of the same harmonic as the switched gradient owing to crosstalk between the gradient channels, leading to inadequate compensation. Lastly, the applied compensation waveforms also produce their own eddy currents, which have to be accounted for. On the other hand, the coil shielding method can take up valuable bore space and can reduce the efficiency of the coil. Also, shielding does not compensate for eddy currents flowing in structures inside the gradient shield. Most modern systems therefore employ both eddy

current waveform compensation and active shielding in the first order gradients to effectively reduce eddy currents.

The majority of the 2^{nd} and 3^{rd} order shim systems available today possess neither waveform compensation nor active shielding. Historically, this has not been a problem as higher order shims are generally not switched rapidly during a scan. In fact, most of the experimental studies of eddy currents have dealt with primarily first and zeroeth order fields. However, DS involves the rapid switching of higher order shims in addition to the gradients. For successful implementation of DS, at least one method of eddy current compensation may be necessary if not both.

In this thesis, we have characterized the eddy currents arising from switching of 2^{nd} and 3^{rd} order shims. We have reported on the improvements made by the use of a single shielded shim coil (the Z2 coil) on image quality at 7 Tesla. A novel software based prospective technique of compensation of eddy fields produced by the dynamic switching of 2^{nd} and 3^{rd} order shims has also been developed and its utility demonstrated.

CHAPTER III

IMPLEMENTATION OF SLICEWISE DYNAMIC B_0 SHIMMING

3.1. Introduction

Compensation for field inhomogeneities has traditionally been carried out by room temperature static global shimming (GS) using a set of discrete orthogonal shim coils designed to produce specific spatial field corrections to minimize field inhomogeneities. As introduced in Section 2.5, these shim settings are usually determined and applied in the preparation phase and remain constant throughout the scan. Global shims optimize B_0 homogeneity over the entire volume of interest, rather than individual slices or sub-volumes. Dynamic shimming (DS) is a technique in which the slicewise shim settings can be changed during the acquisition of data from multiple slices or sub-volumes. Therefore, multiple shim settings optimal for each slice or sub-volume can be applied during a single experiment, leading to better localized compensation of field inhomogeneities, than obtainable using a single global shim set. With increasing field strengths and consequently higher susceptibility artifacts, DS can be an important tool to improve image quality compared to conventional shimming techniques.

A review of earlier work on DS has been presented in section 2.5. Previous DS implementations include multislice shimming to 1^{st} order [Blamire 1996, Morrell 1997] and 2^{nd} order [de Graaf 2003, Koch 2006, 2007]. In addition, 2^{nd} order DS has also been demonstrated to be effective in compensating for field variations induced due to respiration at 7 Tesla [VanGelderen 2007]. All implementations of DS to date have

incorporated an external hardware module for rapid switching of shims. Furthermore, in addition to the basic shim switching module, Koch *et al* also incorporated a multiple time constant compensation circuit for the compensation of the eddy currents produced by rapid switching of the 2nd order shims [Koch 2006, 2007].

Slicewise DS has not been implemented previously on a 7 Tesla clinical scanner. With increased ΔB_0 values at 7 Tesla, there is a need to evaluate the benefits that may be obtained with DS over static GS. The majority of the work presented in this thesis involves the implementation and evaluation of slicewise DS on a 7 Tesla whole body imaging system. This chapter presents the implementation of DS along the following lines

- Description of our scanner and shim system.
- Shim calibration.
- The process of shim calculation, from fieldmap data to shim values.
- Shim calculation approaches for slicewise optimized shims.
- The pulse program modifications and hardware additions for dynamic shim update.
- The dataflow of the DS setup.

3.2. Scanner and Shim system

The higher order DS studies were performed on a 7 Tesla whole body human MRI system (Philips Healthcare Inc, Cleveland Ohio, USA) with a 16 channel SENSE array receiver coil (Nova Medical, Inc, Wilmington, MA, USA) and a single channel quadrature transmit volume coil. The Philips 7T system design included 7 unshielded 3rd order shims (Z3, Z2X, Z2Y, Z(X2-Y2), XYZ, X3, Y3), 5 unshielded 2nd order shims (Z2,

ZX, ZY, X2-Y2, XY) and 2 actively shielded shims (Z2Dynamic or Z2D, Z0). The actively shielded shims were designed with low inductances for dynamic operation. The 2^{nd} order shims were wound on the gradient tube while the 3^{rd} order shims were on a separate tube. The shielded coils were composed of the primary coil and an outer shield coil connected in series. The shims were driven by amplifiers manufactured by Resonance Research Inc (MXH -14, ± 10A, ±95V, RRI, Billerica, MA, USA). Each amplifier had an additional auxiliary analog input for separate additive shim drive control. First-order shimming was provided via the 3 actively shielded 1^{st} order (X, Y, Z) gradients, controlled by the scanner's imaging gradient amplifiers.

The shim system control board was connected to the system computer using a 1 Gbaud/80 Mbytes/second high speed fiber glass serial link. The control board generated RS 232 output at 19.2 kBaud for the static shim channels, connected by a 9 pin connector. The RS 232 asynchronous connection for the static shims was the main bottleneck in the rapid and precise switching of shims, required in DS. This communication setup is almost universally found in shim systems, making DS difficult. For the dynamic Z2 and Z0 channels, the board generated ± 10V differential waveforms, connected to the amplifiers via 25 pin analog connectors. Also, the scanner pulse programming software provided object orientated controls for the gradient channels which enabled complete waveform control of the gradients. Such control was however not present for the individual shim channels.

To overcome the above mentioned hardware obstacles, we followed the approach taken by earlier DS studies. We performed the dynamic update of 2^{nd} order shims using a separate shim control hardware module (*'Load & Go Real Time Shims RTS'* MXV 14/4,

RRI, Billerica, MA, USA) which was used to store the slicewise shim values and load them on trigger from the scanner. Further details on the design and operation of the module are given in Section 3.6.

Given this basic setup for shimming, our method was based on estimating the slice-wise B_0 field variations from a repeated gradient echo scan with a known ΔTE and analyzing the fieldmaps to calculate slice-wise shim settings for DS and a global shim set for static GS. Shim calculation was performed entirely in Matlab2008^{TM} (Mathworks Inc, Natick, MA, USA). A graphical user interface (GUI) was developed in Matlab^{TM} and run on the console computer to enable expedited shim analysis. We performed shim comparison studies on phantoms and human subjects. The benefits of DS were evaluated by comparing the residual B_0 inhomogeneity, image distortion and signal losses to those obtained by conventional image based static GS.

3.3. Shim system calibration

The complete shim set up to 3rd order, was calibrated using a 17 cm spherical doped water 'braino' phantom placed at magnet isocenter. Individual shims were stepped in the range of -80% - 80% of the rated absolute current output of the shim amplifier in steps of 20 % (-8A, -6A…6A, 8A) using the real time shim switching hardware. Multislice axial fieldmaps were obtained in hertz, using the scanner's built-in B_0 estimation option. This option allows the introduction of a second data acquisition period at a user defined known ΔTE value in a gradient recalled echo (GRE) sequence. Other parameters of the sequence were, TR/TE = 95/4.4 ms, FOV = 300 mm, no of Slices = 11. A reference fieldmap obtained without any shim applied was subtracted from these

fieldmaps and the resulting maps were fit to the normalized set of spatial shim harmonic functions using a multilinear least squares regression function in Matlab 2008a. Cross terms were considered significant for only those channels that had a squared correlation coefficient (r^2) value > 0.9. Hence, a set of shim calibration coefficients were obtained, specifying the field in Hz/cm^n (or mT/m^n) produced per ampere of shim current, *n* being the order of the shim. These coefficients were used in our studies to calculate the shim currents required for field correction. Table 3.1 gives the values of the measured shim calibration constants including the relevant cross terms observed. These values matched with the scanner's stored factory settings, validating the procedure as well as calibrating the real time shim module.

3.4. Shim calculation: Practicalities

As described previously in section 2.5, shimming involves calculation of the individual spherical harmonic shim field magnitudes required to compensate for $\Delta B_0(x, y, z)$. These magnitudes can be converted to the actual currents required in the coils by the calibration constants, as given in Table 3.1. The following section describes the practical steps in shim calculation

3.4.1 Coordinate Transformations

Image based multislice fieldmap data acquired for shim calculation are generally defined only in the 'image' coordinates, i.e. in row, column and slice indices. These coordinates most often do not correspond to the shim or gradient coordinate system, which may be given as *x, y* and *z.* Therefore, to calculate the coefficients for the shim

		Field Produced in Hz/cm^n																
		Z0	X	Y	Z	Z2	Z2D	ZX	ZY	X2-Y2	2XY	Z3	Z2X	Z2Y	Z(X2-Y2)	2XYZ	X3	Y3
Shim Switched per Ampere	Z0	286.14																
	X		27.57															
	Y			27.59														
	Z				27.94													
	Z2	-149.9				-1.97												
	Z2D	-29.9	-1.64962		-0.42586		-0.58											
	ZX		0.1327					3.32										
	ZY								-3.33									
	X2-Y2	9.1		-0.146						3.19								
	2XY										3.00							
	Z3	-0.5187			0.4604	-0.0078						-0.0125						
	Z2X	-0.5778	0.3498			0.0140		-0.0161		-0.0038			-0.0155					
	Z2Y	-1.6037	0.1124	0.107										-0.0151				
	Z(X2-Y2)		-0.1250					-0.0497		0.0158					0.0985	-0.0015		
	2XYZ	-0.4420	0.1316	-0.0631	0.1404			0.0240	-0.0477		0.0131				0.0017	0.0974		
	X3			-0.11928						-0.01415	-0.0155				-0.000796		0.045	-0.00103
	Y3		0.14368		-0.11552					0.01379	-0.01488						0.00085	0.044
	Cross terms only with correlation $r^2 > 0.9$ shown.																	

Table 3.1: Calibration constants in (Hz/cm^n)/ Amp measured for the 7T shim system.

harmonics that are defined in either cartesian or polar coordinates (Table 2.1), one has to transform the image space coordinates (**R**ow,**C**olumn,**D**epth) to coordinates in the shim coordinate system (X,Y,Z). In practice, a series of transformations are required for this which account for slice gap/thickness, stack orientation, stack angulations and patient orientation.

Figure 3.1 shows the coordinate system of the 7T scanner. The positive *z* axis is defined to be coming out of the front of the magnet. The *x* axis is defined to be vertical and the *y* axis is defined to be horizontal.

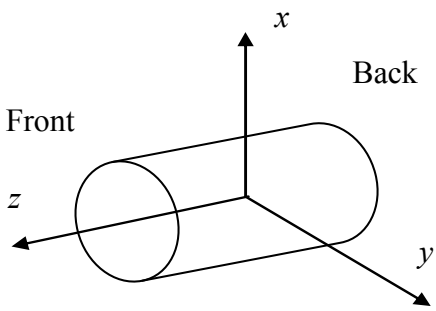

Fig 3.1 Shim coordinate system in our 7T scanner.

Several different coordinate systems are employed for different definitions of the object of interest. The coordinate systems are

1. The *Image coordinate system* (RCD), defining the row, column and depth of the image data.
2. The *Patient coordinate system* (L, P, H) defining the Left hand side, Posterior and Head of the patient.
3. The *Angulated patient coordinate system* (L', P', H') defining LPH system in an angulated slice.
4. The *Magnet coordinate system* (X, Y, Z) defining the *x,y,z* coordinates of the magnet which coincides with the gradient and shim system.

The transformations that are applied to the image based fieldmap data in the order of application are

1. Slice Orientation Transformation : This transformation, transforms the image coordinates to the patient coordinates which vary depending on whether the slice was axial, coronal or sagittal slice orientation.

2. Angulation Transformation :The Angulation transformation obtains slice rotated coordinates from the patient coordinates, depending on the slice angulation.

3. Patient Orientation Transformation :The patient orientation transformation obtains the shim/magnet system coordinates from the patient coordinates. This transformation considers the patient position, i.e. 'head first' or 'feet first' and the patient orientation i.e. 'prone' or 'supine'.

Therefore, to obtain the shim system coordinates of any arbitrarily positioned and rotated slice in the scanner, the series of transformations can be written as

$$\begin{bmatrix} Shim\,system \\ Coordinates \end{bmatrix} = \begin{bmatrix} Slice\ Orientation \\ Transformation \end{bmatrix} * \begin{bmatrix} Angulation \\ Transformation \end{bmatrix} * \begin{bmatrix} Patient\ Orientation \\ Transformation \end{bmatrix} * \begin{bmatrix} \mathrm{Im}age \\ Coordinates \end{bmatrix} \tag{3.1}$$

3.4.2 Multiple Regression and optimization functions

Once the fieldmap data has been transformed to the actual shim (*x,y,z*) coordinates, one can perform multiple linear regression to calculate the shim coefficients.

A set of normalized shim harmonic function values as given in Table 3.2 are calculated for each *x,y,z* location in the shim ROI which provide the $S_i(x,y,z)$ in Eq. 2.20. The regression can be performed by several different methods differing in the cost function employed. Three commonly used cost functions include

1. Sum of squares of field values (or Least Squares Method)

This method obtains the shim coefficients that minimize the sum of squares of the error between the measured and the estimated field. Therefore, it finds c_i such that

$$\sum_{p=1}^{P}\left[\Delta B(x_p, y_p, z_p) - \sum_{i=1}^{N} c_i S_i(x_p, y_p, z_p)\right]^2 \qquad (3.2)$$

is minimized. *P* is the number of pixels in the shim ROI. *N* represents the number of spherical harmonics. The least squares optimization method optimizes the actual pixelwise deviations of the field $\Delta B_0(x,y,z)$, which is directly related to image distortion (Eq 2.7). Therefore, employing this method of shim calculation in DS vs GS studies would be expected to yield greater benefits in distortion reduction compared to voxel wise signal recovery. However, most current GS algorithms employ the least squares method for shim calculation. In our studies, we used the least squares optimization routine 'lsqlin' in Matlab 2008a for implementing this regression technique.

2. Sum of squares of Intravoxel gradients

This optimization method seeks to minimize the signal loss due to the field gradients across a voxel [Wen 1995]. Since the signal loss in a voxel is directly

related to the amount of spin dephasing caused by the B_0 gradients across the voxel (Eq 2.16), minimizing the intravoxel gradients maximizes the signal. Therefore, the quantity to be minimized is

$$D = \sum_{VOI} \left[\left(\frac{\partial B}{\partial x} \right)^2 + \left(\frac{\partial B}{\partial x} \right)^2 + \left(\frac{\partial B}{\partial x} \right)^2 \right] \tag{3.3}$$

which is the least squares sum of the field gradients across the voxels in the shim volume of interest (VOI). Therefore, this method of shim calculation in DS vs GS studies would be expected to yield greater benefits in signal recovery compared to image distortion. In our studies, we used the 'fmincon' optimization routine in Matlab 2008a for implementing this regression technique.

As an alternative to this method, one may also optimize the field based on maximizing the signal. Since the signal in a voxel is related to the sinc of the intravoxel gradients (Eq. 2.16), one may attempt to minimize the signal loss by maximizing this function.

3. Peak to Peak value of the field

In this method, the peak to peak value of the field is minimized [Prammer 1988]. Consequently, the worst case field errors are minimized, which may not be the case in the two earlier methods. This method can however be susceptible to noise in the fieldmap and effective noise removal is required to make it robust. In our studies, we used the 'fmincon' optimization routine in Matlab 2008a for implementing this regression technique.

In all the methods described above, the optimization has to be constrained to the actual current limits of the shim amplifiers. It has been shown that for global shimming, constrained optimization methods performed significantly better than simple truncation methods, where the shim values are truncated according to the shim current limits [Wen 1995]. We employed constrained optimization in all our DS and GS studies. The shim values were constrained at ±10 Amperes, the current limit of the shim amplifiers. Constraining the shims was found to be particularly important in the case of the weak 3rd order shims and the shielded 2nd order Z2 shim. Section 4.1.2 presents further results on shim constraining in the context of higher order slicewise DS.

3.4.3 Stack Offset Correction

For calculation of shim correction values c_i for a given stack of slices, the origin of the X,Y,Z coordinate system is in practice, assumed to be at the center of the stack. This is correct when the stack is centered at the true magnet isocenter. However, when the stack is translated in any direction, the c_i coefficients have to be adjusted for the offset [Hoult 1987]. The corrected shim coefficients then are those shim values that would give the same residual field for the offset stack as what is predicted when assuming the stack to be at the origin of the shim coordinate system. For example, consider a z^2 field perturbation located at an offset location given by a. The field may be defined in the magnet coordinate system as $(z-a)^2 = z^2 - 2za + a^2$. Therefore, if a $-z^2$ correction field (as calculated in the offset slice coordinate system shim regression) is applied, a linear and constant field of $-2za + a^2$ remains uncompensated. These linear

and constant fields therefore have to be compensated in addition to the basic z^2 field correction. In general for accurate higher order inhomogeneity compensation at offset locations, lower order cascading fields in addition to the basic higher order correction are required. These lower order corrections can be calculated by the expansion of the cartesian shim definitions as in the example above. The corrections for the individual 2nd and 3rd order shim coefficients are

For 2nd order shimming

$Z = Z -[\ 2 * \ Z2 * \ z_o + \ ZX \ * \ x_o + ZY \ * \ y_o\ ]$

$X = X - [-Z2 * xo + ZX * z_o + 2 * X2Y2 * x_o + 2 * XY * y_o]$

$Y = Y - [-Z2 * y_o + ZY * z_o – 2 * X2Y2* y_o + 2 * XY * y_o]$

For 3rd order shimming

$$Z = Z + [2 * Z2 * z_o + ZX * x_o - ZY * y_o + 3 * Z3 * (z_o^2 - (x_o^2 + y_o^2)/2) + 8 * Z2X* x_o* z_o - 8 * Z2Y* y_o* z_o + Z(X2-Y2) * (x_o^2 - y_o^2) - 2 * ZXY * x_o * y_o];$$

$$X = X + [- Z2 * x_o + ZX * z_o + 2 * X2-Y2 * x_o - 2 * XY * y_o - 3 * Z3 * x_o * z_o + Z2X * (4 * z_o^2 - 3 * x_o^2 - y_o^2) + 2 * Z2Y * x_o * y_o + 2 * Z(X2-Y2) * x_o * z_o - 2 * ZXY * yo * z_o + 3 * X3 * (x_o^2 - y_o^2) - 6 * Y3 * x_o * y_o];$$

$$Y = Y + [Z2 * y_o + ZY * z_o + 2 * X2-Y2 * y_o + 2 * XY * x_o + 3 * Z3 * y_o * z_o + 2 * Z2X * x_o * y_o + Z2Y * (4 * z_o^2 - x_o^2 - 3 * y_o^2) + 2 * Z(X2-Y2) * y_o * z_o + 2 * ZXY * x_o * z_o + 6 * X3 * x_o * y_o + 3 * Y3 * (x_o^2 - y_o^2)];$$

$$Z2 = Z2 + [3 * Z3 * z_o + 4 * Z2X * x_o - 4 * Z2Y * y_o];$$

$ZX = ZX + [-3 * Z3 * xo + 8 * Z2X * zo + 2 * Z(X2-Y2) * xo - 2 * ZXY * yo];$

$ZY = ZY + [3 * Z3 * yo + 8 * Z2Y * zo + 2 * Z(X2-Y2) * yo + 2 * ZXY * xo];$

$X2-Y2 = X2-Y2 + [-Z2X * x_o - Z2Y * y_o + Z(X2-Y2) * z_o + 3 * X3 * x_o - 3 * Y3 * y_o];$

$XY = XY + [Z2X * y_o - Z2Y * x_o + ZXY * z_o + 3 * X3 * y_o + 3 * Y3 * x_o];$

Where x_o , y_o and z_o are the stack offsets in the magnet coordinate system. The shim coefficients are represented by their common names.

In our work the above formulations including the coordinate transformations, three different regression methods and stack offset correction were implemented for both global and dynamic shimming. Global shim calculation followed the general shimming procedure described above and in section 2.5. For slicewise shim calculation however, additional steps were performed, which are described in the following section.

3.5 Calculation of Dynamic Slicewise shims

Two different approaches can be used to calculate slicewise shims based on multislice fieldmaps.

3.5.1 Calculation by considering three slices together

In this approach, fieldmap data from a set of slices, typically 3, centered on the slice of interest are used to calculate the shim coefficients for that slice. All the shim coefficients are obtained from a single regression. This procedure is therefore similar to a global shim fit with only three slices, repeated for every slice in the stack. Even though the shims are calculated for only one central slice, data from the adjacent slices is used in

the regression. In this technique, if the fields in the adjacent slices are very different, the inplane field correction for the central slice may be compromised since the shims will globally fit the data from the three slices.

3.5.2 Calculation by degeneracy analysis for inplane shims

In the second method of slicewise shim calculation, the inplane and through plane shim corrections are estimated separately. In this way, the inplane correction can be localized to the slice of interest only, while the through plane correction is calculated using the adjacent slice data.

When calculating the inplane shim corrections using data from only a single slice, an infinitesimal slice thickness is assumed since there is no through slice field information considered. This leads to different shim harmonics manifesting in the same inplane functional form. The assumption of linear independence between shim terms no longer holds, leading to degeneracy in the regression [Shen 2000, Koch 2006]. An analytical solution to this degeneracy problem was presented in detail by Koch *et al*, where the complete shim set is reduced to a subset of linearly independent shims for any slice orientation [Koch 2006]. In order to extract the non-degenerate shim set, a coordinate transformation from the magnet coordinate system, i.e., *x, y, z* to the slice coordinate system or *R, C ,D* is employed. If α, β, and γ represent the angular rotations of the imaging plane about the three magnet coordinate axes *x, y* and *z,* the new coordinates are related to the original coordinates by the transformation matrix:

$$\begin{bmatrix} R \\ C \\ D \end{bmatrix} = \begin{bmatrix} Cos(\beta)Cos(\gamma) & Cos(\alpha)Sin(\gamma)+Sin(\alpha)Sin(\beta)Cos(\gamma) & Sin(\alpha)Sin(\gamma)-Cos(\alpha)Sin(\beta)Cos(\gamma) \\ -Cos(\beta)Sin(\gamma) & Cos(\alpha)Cos(\gamma)-Sin(\alpha)Sin(\beta)Sin(\gamma) & Sin(\alpha)Cos(\gamma)+Cos(\alpha)Sin(\beta)Sin(\gamma) \\ Sin(\beta) & -Sin(\alpha)Cos(\beta) & Cos(\alpha)Cos(\beta) \end{bmatrix} \begin{bmatrix} x \\ y \\ z \end{bmatrix} \quad (3.4)$$

Thereafter, equating the through-plane (depth) coordinate value for any slice, to the *x,y,z* linear sum from Eq 3.7, yields a set of relations between the magnet coordinates. The reduced shim set can then be obtained by inserting the relationships between these magnet coordinate directions into the shim functions and subsequently removing functional redundancies from the shim set.

For example, consider a slice rotated 45^{o} about the *y* axis ($\alpha = 0$, $\beta = 45^{o}$, $\gamma = 0$) as shown in figure 3.2. Since the slice is at the origin, the depth coordinate is equal to 0.

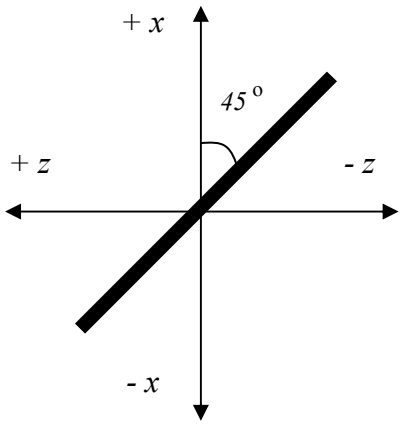

Name	Base Form	Reduced form ($\beta = 45$)
X	x	$-z$
Y	y	y
Z	z	z
$Z2$	$z^2-(x^2+y^2)/2$	$(z^2-y^2)/2$
ZX	zx	$-z^2$
ZY	zy	zy
$X2-Y2$	x^2-y^2	(z^2-y^2)
XY	xy	$-zy$
$Z3$	$z^3-3z(x^2+y^2)/2$	$-(z^3+3zy^2)/2$
$Z2X$	$x(4z^2-x^2-y^2)$	$-3z^3+zy^2$
$Z2Y$	$y(4z^2-x^2-y^2)$	$3z^2y-y^3$
$Z(X2-Y2)$	$z(x^2-y^2)$	z^3-zy^2
XYZ	xyz	$-z^2y$
$X3$	x^3-3xy^2	$-z^3+3zy^2$
$Y3$	$3x^2y-y^3$	$3z^2y-y^3$

Figure 3.2: Extraction of non degenerate 3rd order shim set for a slice at $\beta = 45^{o}$.

Therefore, from Eq 3.7 we have,

$$x\,Sin(\beta)-y\,Sin(\alpha)Cos(\beta)+z\,Cos(\alpha)Cos(\beta)\;=\;0 \qquad or \qquad x\;=-z$$

Substituting this relationship in the shim functions we see that the shims pairs (X, Z), (X2-Y2, Z2), (ZY, XY) and (Z2Y, Y3) reduce to the same functional forms as shown in Figure 3.2 leading to redundancy of the shim terms. The redundancy can be removed by eliminating one shim from every shim degenerate pair yielding a reduced shim set which includes only the shims: Y, Z, Z2, ZX, ZY, Z3, Z2X, Z2Y, ZXY, Z(X2-Y2), X3 in this case. The fieldmap data for this slice are then fit only to the reduced shim set to obtain in-plane correction values. The choice of the reduced shim set is flexible and may vary depending on the particulars of the scanner and shim system. For example, if the system includes a shielded Z2 coil, Z2 may be preferred in this case over X2-Y2.

For calculating the through-plane shims, it is assumed that the through-plane fields for usual slice widths can be approximated as simple linear gradients. This is reasonable for typical imaging slice thicknesses. However, it is important to preserve the inplane shim setting when applying the through plane shims since in angulated slices, the linear gradients will have an inplane component as well. For non oblique slices, the shim coefficients are just the gradient in the through plane direction, which does not affect the inplane field, e.g. the Z gradient for an axial slice. For oblique slices, the projections of the field gradient normal to the slice (or through-plane direction) onto the principal gradient directions (*x,y,z*) give the through-plane shim corrections. These corrections add up to the required field gradient in the direction normal to the plane, while cancelling out in-plane, thus preserving the in-plane field.

The above method of slicewise shim calculation has certain important differences from the previously described 3 slice method. First, since the inplane shim values are calculated using data from only the target slice rather than 3 slices, the inplane field is

better optimized. However, since only a linear though plane correction is performed, the through plane field variation may not be compensated as well as the first method, leading to higher signal losses. This may become increasingly important as the slice thickness increases. Secondly, since only a reduced set of shims are switched dynamically, the amount of eddy currents produced are reduced. This becomes important especially in low bandwidth imaging where eddy current effects are severe. Both the methods have been implemented in our work. For the majority of our comparison studies with static shimming, we have employed the second method with degeneracy analysis.

Figure 3.3 illustrates the Matlab 2008a based shim tool GUI developed for expedited shim analysis. The tool was run on the console computer and was easily distributable to intended clients. It included image based DS and GS, with options for other relevant parameters including fieldmap thresholding techniques, shim switching patterns, choice of shielded/unshielded coils etc.[1] The tool communicated with the RTS via the RS 232 COM1 communication port of the scanners console computer.

3.6 Dynamic shim update

During the scan, the slicewise shim values were updated prior to slice selection (or RF excitation) for every slice. The first order and higher order shims were updated differently.

[1] Details of the tool features, user directions and run environment requirements are available in a separate user manual. Contact Saikat Sengupta at saikat.sengupta@vanderbilt.edu for details.

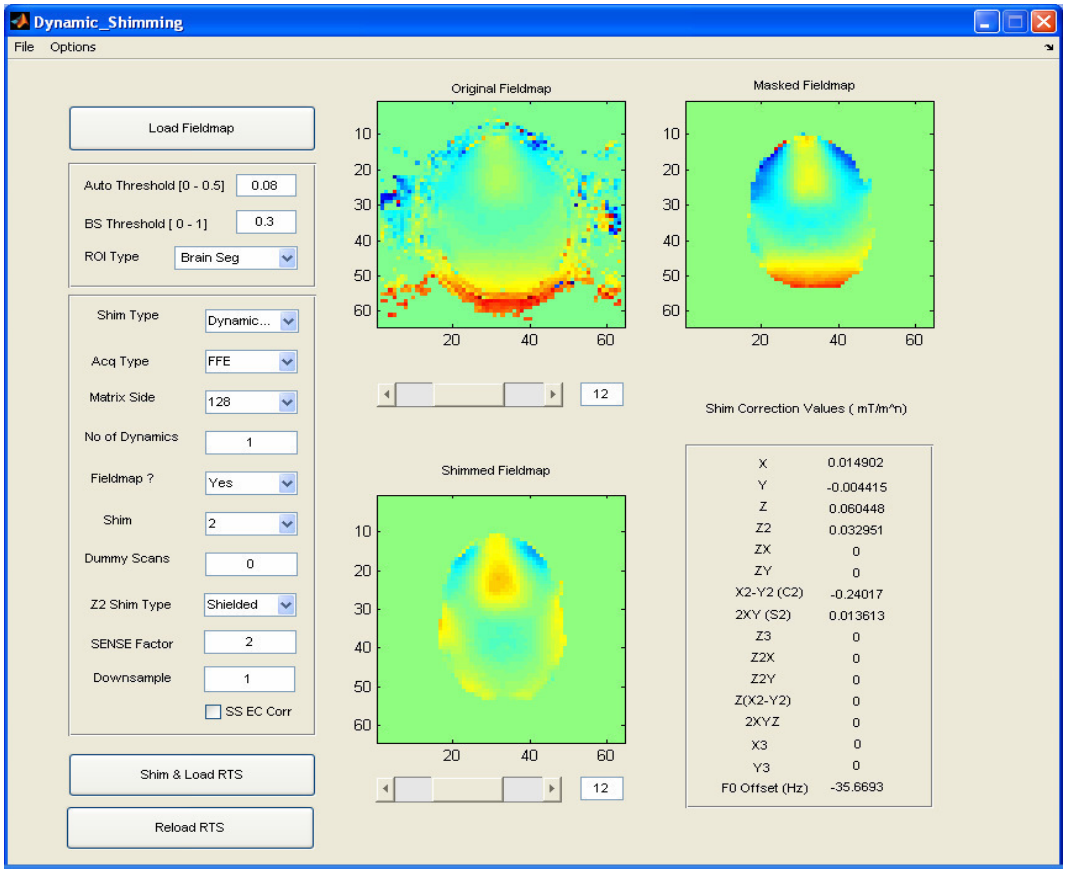

Figure 3.3 Matlab 2008a based shimming tool run on the console computer.

1st order shim update

The 1st order slice wise shim coefficients in mT/m obtained from the shim regression were written into text files and saved on the console computer for the pulse program to read during the scan operation. 1st order dynamic corrections were performed using the gradient control for X, Y and Z gradients. The values were read into an array in the pulse program from the text files and applied before every slice excitation using an inbuilt pulse program function. The sequential order of the shim values in the text files

were matched to the planned slice order. User interface controls were added to display and modify the first order shim values if required.

2nd and 3rd order shim update

Dynamic update of 2nd and 3rd order shims was performed using a separate shim control hardware module. (‘*Load & Go Real Time Shims,* ***RTS****’* MXV 14/4, Resonance Research Inc, Billerica, MA, USA). The RTS system is a multi-channel small signal driver capable of providing pre-programmed signals to the scanner shim amplifiers to allow DS operations. The RTS consisted of a solid state hard drive computer to process custom commands and store shim values, RS232 serial communication ports for shim value inputs and digital to analog converters (16 bit DAC, 4 DACs per channel, 15 channels) controlled by a digital I/O bus from the computer. The shim program on the console computer communicated with the RTS via an RS232 serial connection, with custom commands to send in the shim values, along with the shim ordering based on the parameters of the proposed imaging sequence. The hard drive stored the shim files that were loaded prior to the scan. The RTS was connected to the auxiliary input of the shim unit via an analog connection. Fig 3.4 illustrates the main components of the module, the most relevant commands used for control and the connection of the box to the shim cabinet. The shim values were supplied to the RTS in the form of 16 bit i.e. from -32767 to 32767, which corresponded to 10 to -10 amperes (-3276.7 DAC units /Amp). Therefore, the shim values calculated in Hz/cm^n were converted to DAC units for upload using the commands shown in Figure 3.4.

The RTS module did not allow for random access of the stored shim values and applied the values loaded in a predetermined loop wise fashion. Also the shim order once loaded could not be altered. Therefore, care had to be taken to match the shim order

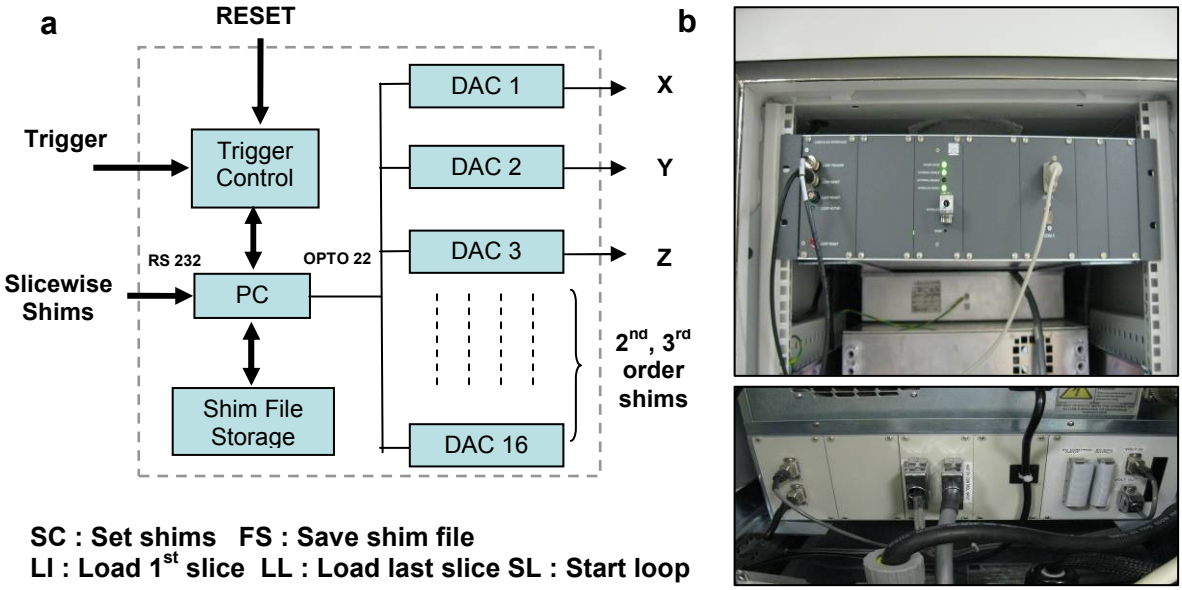

Figure 3.4 The RRI Real Time shim module (a) Components and primary RS 232 control commands (b) The module mounted in the shim cabinet (top) and connected to the shim auxiliary supply (bottom) .

with the slice order of the intended scan. For simplicity, most of our scans were acquired with ascending slice order and with a single package[1] although other slice orders (descending, default, interleaved, centric and reverse centric) have also been implemented. Also, the number of shim set loops had to be adjusted according to other factors such as matrix size, SENSE factor, dummy scans etc. Errors in the above steps

[1] In the scanner, 'Package' referred to the set of slices that could be fit within a user defined TR. If the prescribed TR was too low for a give number or slices, the stack was split into 2 or more packages, altering the slice ordering.

resulted in shim values being wrongly prescribed leading to bad shim performance and/ or ghosting artifacts.

During the scan, shim files preloaded into the module memory were applied on receipt of a positive going CMOS (complementary metal–oxide–semiconductor) trigger pulse from the spectrometer clock in a sequential loop-wise fashion. These 5μs long trigger pulses were preprogrammed into the pulse sequence before every excitation pulse. The time taken by the module to acknowledge the trigger, update the DACs and load the shim file was ~5-8 ms and the time required for shim amplifier current output stabilization was an additional ~3 ms (rated shim channel rise time, ~1ms + settling time, ~2 ms), making the total time required for output current update of all shims ~10 ms. To allow for this DAC update and amplifier settling, a time interval of 10 ms was added before every excitation pulse. Figure 3.5 illustrates slices 1 and 2 from a 2^{nd} order dynamically shimmed phantom acquired with time delays between the shim application and RF excitation of 5,6,7 and 10 ms. In slice 1, ghosting artifacts in the phase encode direction (left-right) due to the settling of the shim amplifiers are evident[1]. The ghosts are severe in the 5ms case and decrease in intensity with the increase in the delay, as expected. The images acquired with 10ms delay are relatively ghost free. In slice 2 all the images are free of apparent ghosting. The difference in the ghosting intensity of the 1^{st} and 2^{nd} slices may be explained by the fact that the shim switch from the last to the 1^{st} slice is much larger than that from the 1^{st} to the 2^{nd} slice, thereby necessitating longer settling times. After the scan, a final trigger forced the output of the shims to 0 Amps. An external hardware reset switch controlled by the operator was also used to clear the file

[1] In fact, the ghosting may be due to a combination of amplifier settling and short time constant eddy currents. Eddy currents are dealt in detail in section 4.5.

memory in preparation for the next scan. The RTS did not provide controls for the X3 and Y3 channels and had separate outputs for Z2 (labeled Z4) and Z2D (labeled Z2). It also had outputs for X, Y, Z and Z0 which were not used in our implementation.

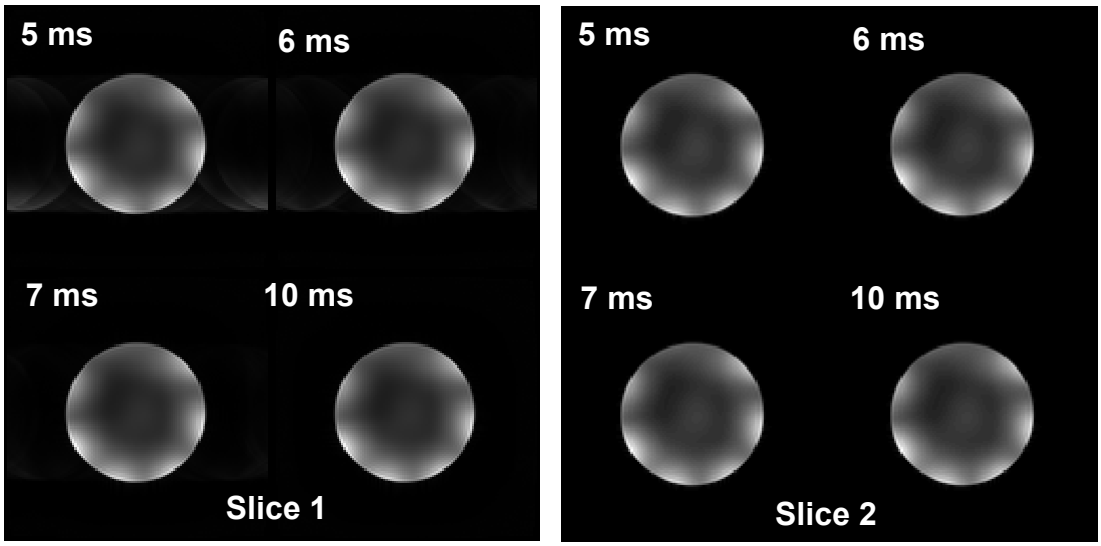

Figure 3.5 2nd order Dynamically shimming spherical phantom images showing effect of delay times on image ghosts (a) Slice 1 with 5, 6, 7 and 10 ms delay times (b) Slice 2 with the same delay times.

Center frequency (f0) update

The slicewise f0 shifts associated with the dynamic addition of the shims were written in a text file and read by the pulse program prior to the start of the scan, along with the 1st order corrections. In the DS scan, the scanner's default f0 determination preparation phase was skipped so that the slicewise f0 values were added to the f0 from the field mapping scan. The f0 was adjusted dynamically for every slice using the spectrometer's f0 setting along with the application of the 1st order shims.

In addition to the static f0 changes, dynamic eddy current related f0 changes also originated from unshielded shim switching. The above procedure did not correct for the

eddy current induced f0 shifts. These changes added to the static f0 changes and decayed with multiple time constants. Compensation for these continuously changing f0 offsets required Z0 shim waveform compensation which the current RTS did not include. We did not include hardware based shim eddy current compensation in this work, as it required additional, multiple waveform shaping circuits for each shim channel. A novel method of software based eddy current related f0 compensation developed as a part of this work is presented in chapter 4.

3.7 Workflow of Dynamic Shimming

The overall workflow of DS illustrated in Figure 3.6 can be summarized in the following steps.

1. A multi slice dual echo GRE ΔB_0 mapping scan covering the same slice planes with the same geometry as required for the main application scan is acquired.
2. ΔB_0 maps and images, user defined shim ROI and scan geometry are exported to the shim tool on the console.
3. Slicewise shims are calculated using the shim tool.
4. The slicewise 1^{st} order and f0 corrections generated by the shimming program are fed back to the scanner as text files, The RTS module is loaded with the higher order (2^{nd} or 3^{rd}) shim coefficients.
5. The application scan is run with the DS option. f0 preparation phase is skipped. The pulse program loads the slice wise 1^{st} order shims and f0 values from the text files during the acquisition of multi slice data. Simultaneously, triggers from the spectrometer prompt the RTS to load the appropriate higher order shim currents.

6. At the end of the scan, an extra trigger is given to the RTS to indicate scan termination and force the shim values to 0 Amps.

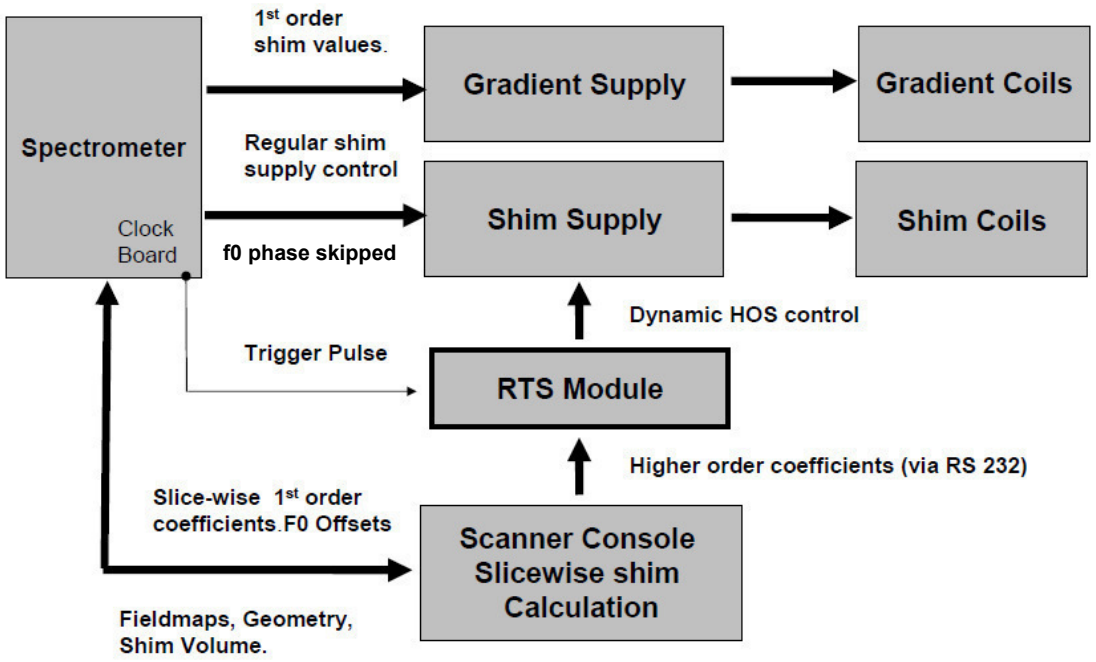

Figure 3.6 Operational diagram of Dynamic Shimming

CHAPTER IV

EVALUATION OF SLICEWISE DYNAMIC B_0 SHIMMING

Chapter III presented the details of implementation of fieldmap based slicewise dynamic and static global shimming on our high field 7 Tesla scanner. To evaluate and compare the performance of the shimming techniques, simulations and experiments were performed in phantoms and humans that measured the post shim fields, image distortions and signal losses. In addition, eddy currents produced by switching of 2^{nd} and 3^{rd} order shims were measured and characterized. Finally, an orderwise comparison of global and dynamic shimming was performed to elucidate the relative benefits of going to higher orders and from global to dynamic shims. This chapter presents the above studies in detail along with other observations relevant to the real world utility of dynamic shimming at high field.

4.1 Comparisons of shim techniques in simulations

4.1.1 Orderwise shim comparison simulations

We performed simulations to evaluate the benefits of going to higher orders in DS versus GS. Human head fieldmaps were acquired in the axial orientation for 24 subjects with a repeated echo GRE sequence which is a part of the scanners default B_0 mapping sequence (FOV 250 x 250 mm, 64 x 64 pixels, 25 slices, slice thickness/gap = 3/1 mm, TR/TE/ΔTE = 195/4/1 ms, SENSE acceleration factor = 3). The fieldmaps were skull

stripped to extract the brain as the shim ROI. Slice-wise dynamic shim residual fields were calculated using the degeneracy analysis with 4 terms (1st order), 9 terms (2nd order), 16 terms (3rd order) and 18 terms (3rd order + Z4 and Z5). Global shim residual fields were also obtained for the four conditions. Post shim fieldmap standard deviation values over the entire brain were then calculated to give a measure of field inhomogeneity.

Results

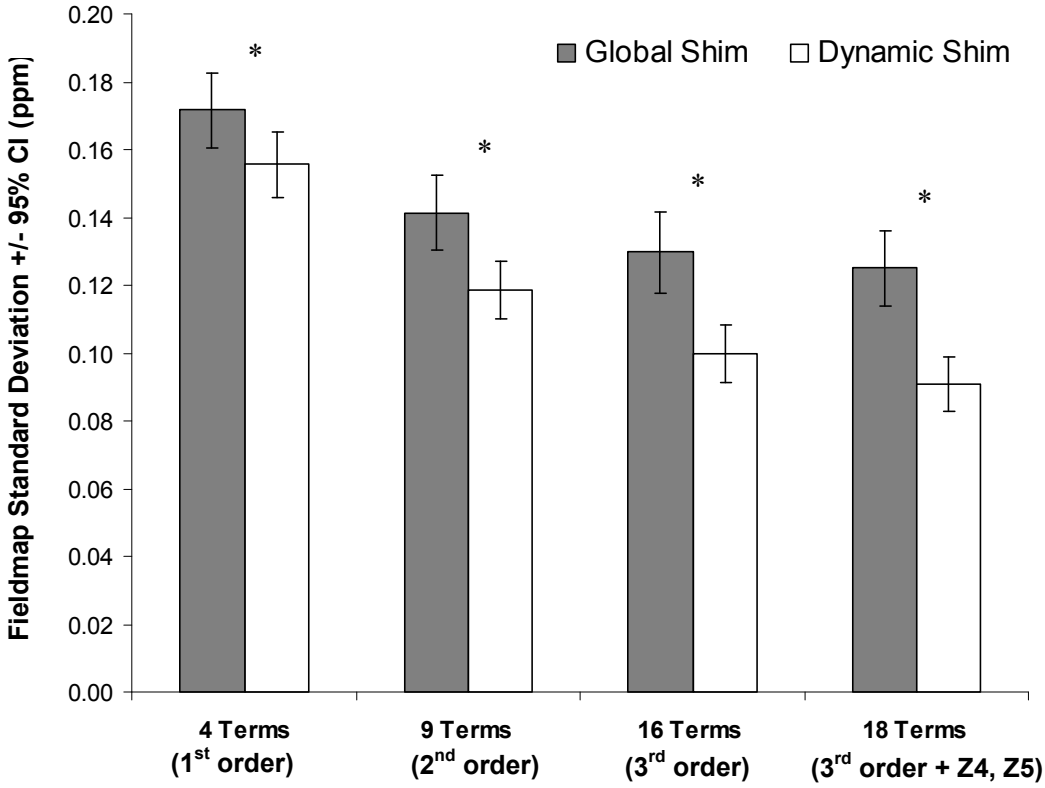

*Fig. 4.1.Comparison of whole brain residual field homogeneity of simulated shimmed fieldmaps across DS and GS shim types and orders. n =24. * Significant at p < 0.001*

Figure 4.1 displays the mean and 95% confidence interval (CI) values of the post shim field standard deviations over the 24 subjects. DS clearly performed better than GS

for all orders evaluated. Furthermore, the gains of using DS over GS increased with increasing number of terms in the shimming. Essentially, the field homogeneity improvements with GS plateaued earlier than those with DS. Overall, two conclusions could be drawn from these simulations. First, it corroborated work by earlier studies demonstrating the benefits of DS compared to GS. Second, it suggested that even though going to 3rd order GS does not provide substantial benefit over 2nd order GS, going to 3rd order DS from 2nd order DS may still provide some improvement. In practice however, 3rd order DS is difficult owing to strong eddy currents produced by the 3rd order shims.

4.1.2 Effect of constraining peak shim demand in DS

Constraining the shims coefficients to the specified current limits of the amplifiers has been shown to be beneficial in comparison to hard truncation of the shim values in GS [Wen 1995, Clare 2006]. We performed DS simulations of the same data set introduced in the previous section to evaluate the effect of constraining the shim coefficients in DS. The simulations were performed for 2nd and 3rd order DS, with and without the current constrains. The residual field homogeneity was evaluated by calculating the standard deviation of the field over the whole volume as before. The slicewise shim coefficients were also recorded.

Results

Figure 4.2 shows the simulated residual field variations after constrained and non-constrained DS as well as slice wise shim values for representative 1st (Z), 2nd (Z2) and 3rd (Z2X) order shims. The bar plots show mean and 95% CI values of the fieldmap

standard deviations over the 24 subjects. Constraining the shim calculation did not hamper the performance of DS significantly for either 2nd or 3rd order DS. However, the slice to slice shim variation observed in all three orders, was considerably higher in the unconstrained setting. Higher shim switches can lead to increased eddy currents and amplifier settling noise. Therefore, even if the non constrained shim demands lie within the current limits of the shim amplifiers, as was the case for example in the Z2 shim

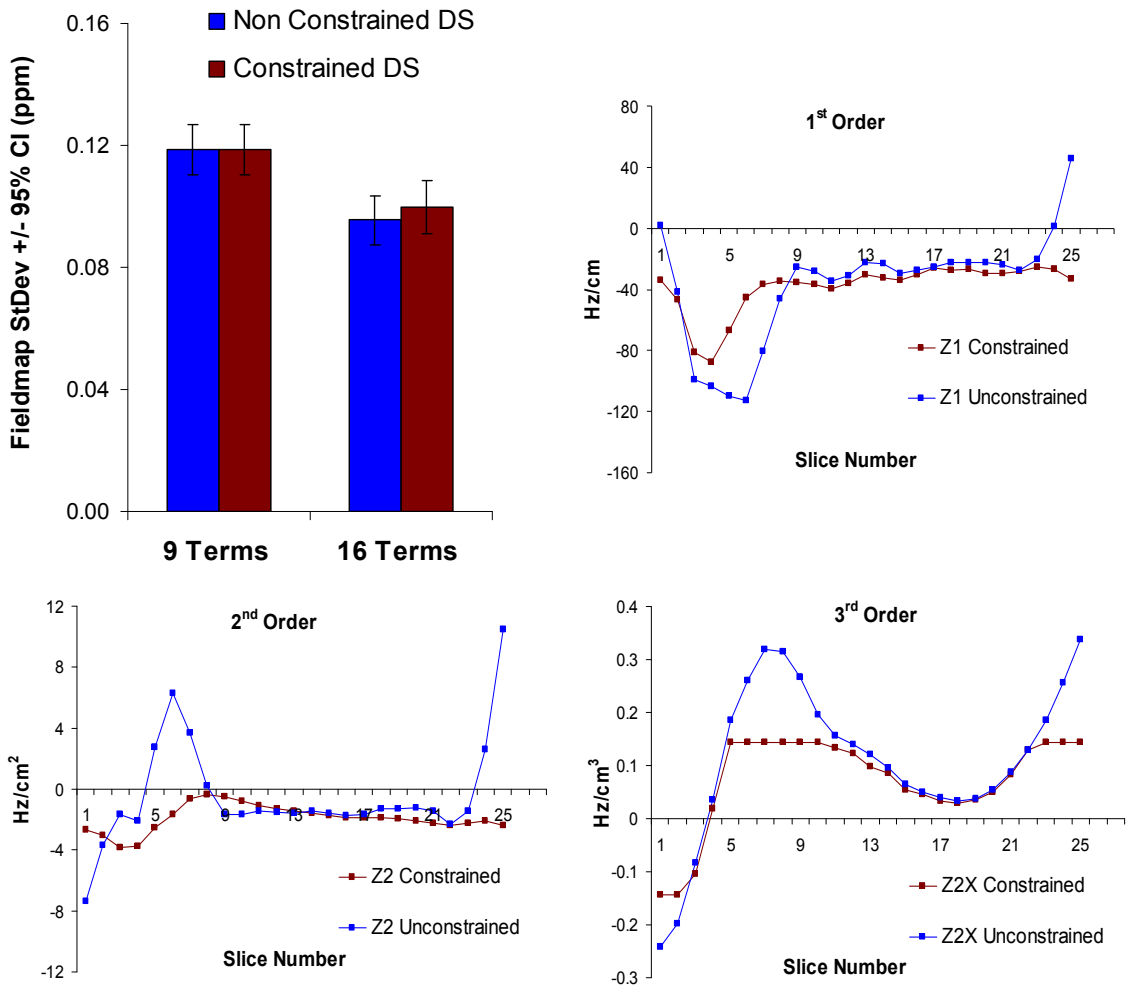

Fig.4.2.Comparison of whole brain residual field homogeneity of simulated constrained and non-constrained 2nd and 3rd order Dynamic shimming with plots showing increased slice to slice shim variation for representative 1st (Z1), 2nd (Z2) and 3rd (Z2X) order shims in unconstrained dynamic shimming.

(current limit for Z2 was 10A, -19.7 Hz/cm^2), the higher shim variation predicted worse performance. In all our imaging studies, shim constraints were included to limit the corrections to ±10 Amps.

4.2. Unshielded Z2 coil *vs* Shielded Z2 (Z2D) coil

Prior to full scale comparisons of dynamic and global shimming, imaging experiments were performed with the unshielded and shielded Z2 coils (single shot gradient echo EPI, 9 slices, FOV = 250 x250 mm, 192 x 192 pixels, TR/TE = 2000/26ms, SENSE acceleration factor = 3) to make a choice between the two coils. The RTS provided dynamic control for both of these coils. The efficiency of the shielded coil was -0.58 Hz/cm^2, around a third of that of the unshielded coil which had an efficiency of -1.97Hz/cm^2. Using the shielded coil would therefore decrease the available range of shim gradient field. For the static shimming techniques including the scanner default shimming, the unshielded coil is used.

Results

Figure 4.3 shows dynamically shimmed SS EPI images obtained with the same imaging parameters and shim correction fields, using the unshielded (Z2) and shielded (Z2D) coils. The images with the shielded coil show considerably lesser ghosting artifacts than those using the unshielded coil, which produced virtually unusable images. These artifacts were most likely due to uncompensated self and Z0 eddy fields caused by the unshielded Z2 coil. The shielded coil was therefore employed in all our subsequent studies.

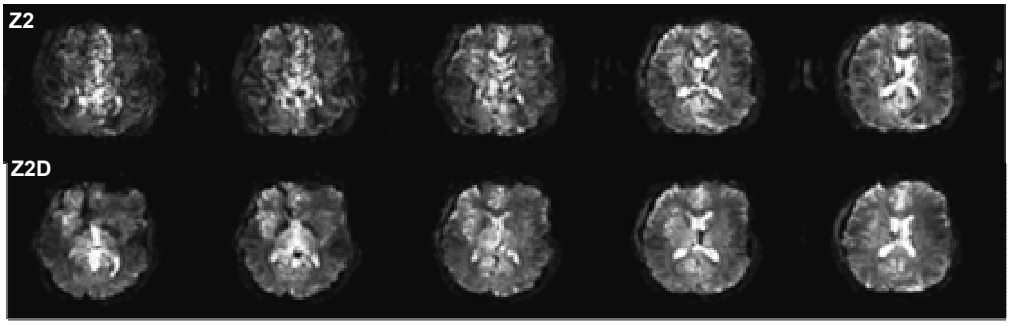

Fig. 4.3.Comparison of unshielded and shielded coil in SS EPI imaging. Images obtained with the unshielded coil show increased ghosting artifacts.

4.3. Phantom and human studies: 2nd order DS vs. 2nd order GS

All studies were performed on the 7 Tesla whole body human MRI system (Philips Healthcare Inc, Cleveland Ohio, USA) with a 16 channel SENSE array receiver coil (Nova Medical, Inc, Wilmington, MA, USA) and a single channel quadrature transmit volume coil. First-order shimming was provided via the 3 actively shielded 1st order gradients, controlled by the scanner's imaging gradient amplifiers and 2nd order shims were controlled using the external shim switching hardware module connected to the auxiliary input of the shim system. Our method was based on estimating the slice-wise B_0 field variations from a repeated GRE scan with a known ΔTE and analyzing the fieldmaps to calculate slice-wise shim settings for DS. Shim calculation was performed entirely in Matlab2008™ (Mathworks Inc, Natick, MA, USA) with the graphical user interface (GUI) run on the console computer to enable expedited shim analysis. We performed studies on phantoms and human subjects. The shielded Z2D coil was used in all DS experiments. The benefits of DS were evaluated by comparing the residual B_0 inhomogeneity, image distortion and signal losses to those obtained by conventional image based static GS.

4.3.1 Phantom experiments

A 17 cm diameter, spherical "Braino" phantom (GE Medical Systems, Milwaukee, WI, USA), containing doped water was used as a test phantom. Low resolution fieldmaps using a repeated GRE sequence with a known ΔTE (64 x 64 pixels, 300 mm FOV, 25 slices, first TE/ΔTE = 4/1 ms, slice thickness/gap = 2/2 mm) were obtained in the three principal orientations, with all shims set to 0 Amps. Using a region of interest (ROI) defined by all voxels with nonzero signal in every slice, slice-wise shim coefficients up to 2^{nd} order were calculated using the degeneracy analysis described in section 3.5.2 along with least squares minimization and fed to the external shim switching hardware module For GS, a single shim set was calculated with the same regression algorithm, for the entire ROI. GRE image sets including underlying fieldmaps were then acquired at 128 x 128 pixel resolution using the same slice geometries, flip angle, readout bandwidth and echo times with both static and dynamic shims. Results were compared in terms of the slicewise standard deviations of the post shim fieldmaps.

Results

Figure 4.4 compares slice-wise B_0 inhomogeneity following 2^{nd} order GS and DS in the spherical phantom. The standard deviation of the residual ΔB_0 expressed in ppm was lower for DS than GS fieldmaps, for all slices and orientations, with the largest improvements observed in the coronal slices. Figure 4.4a shows the first, middle (13^{th}) and last (25^{th}) slice fieldmaps for all three orientations, illustrating the improvements made by DS. Figure 4.4b displays the simulated fieldmaps for the corresponding slices shown in Figure 4.4a. For all slices, the experimental and simulated fieldmaps matched

closely validating the accuracy of the DS and GS implementations. Minor differences may arise from small errors in shim calibration and eddy currents in DS.

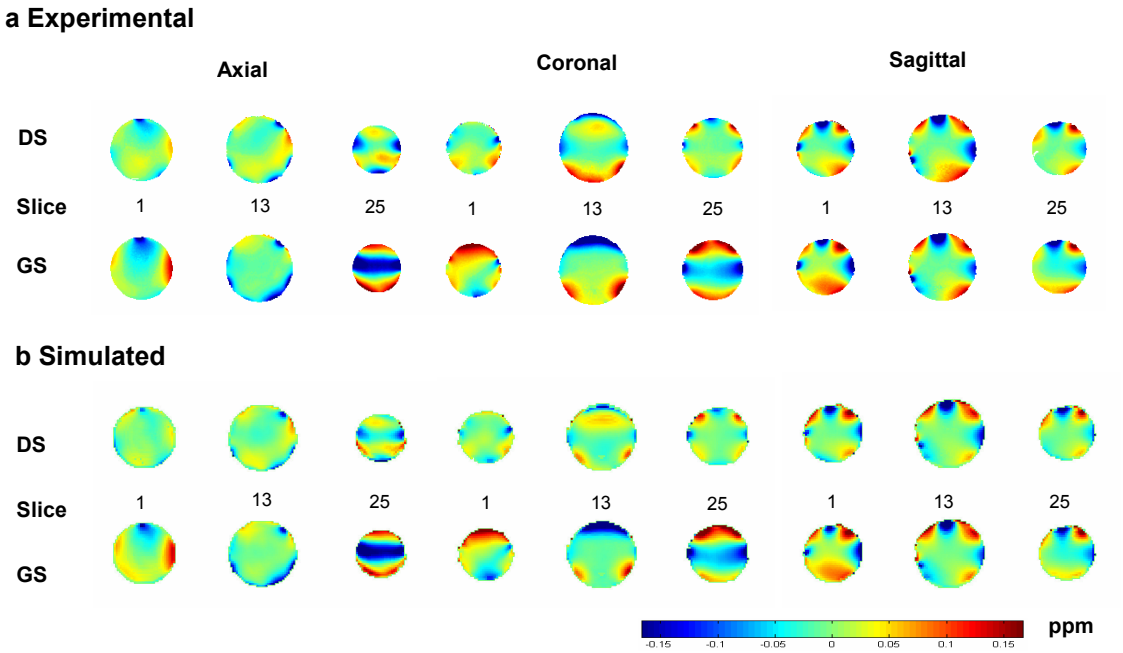

*Fig 4.4. Spherical phantom fieldmaps in ppm of slices 1, 13 and 25 from 25 slice volumes for 3 principal orientations after 2nd order DS and GS (**a**) Fieldmaps from experiments. (**b**) Fieldmaps from simulations. Fieldmaps from experiments and simulations match closely. Residual fields contain high degree of 3rd order spatial harmonics as expected.*

The residual maps also showed strong 3rd order field variations, as expected. Figure 4.5 shows the slicewise residual field standard deviation values, in all three orientations.

4.3.2 Human experiments

All human volunteers provided informed written consent and were scanned under an institutional IRB approved protocol. Low resolution fieldmaps (64 x 64 pixels,

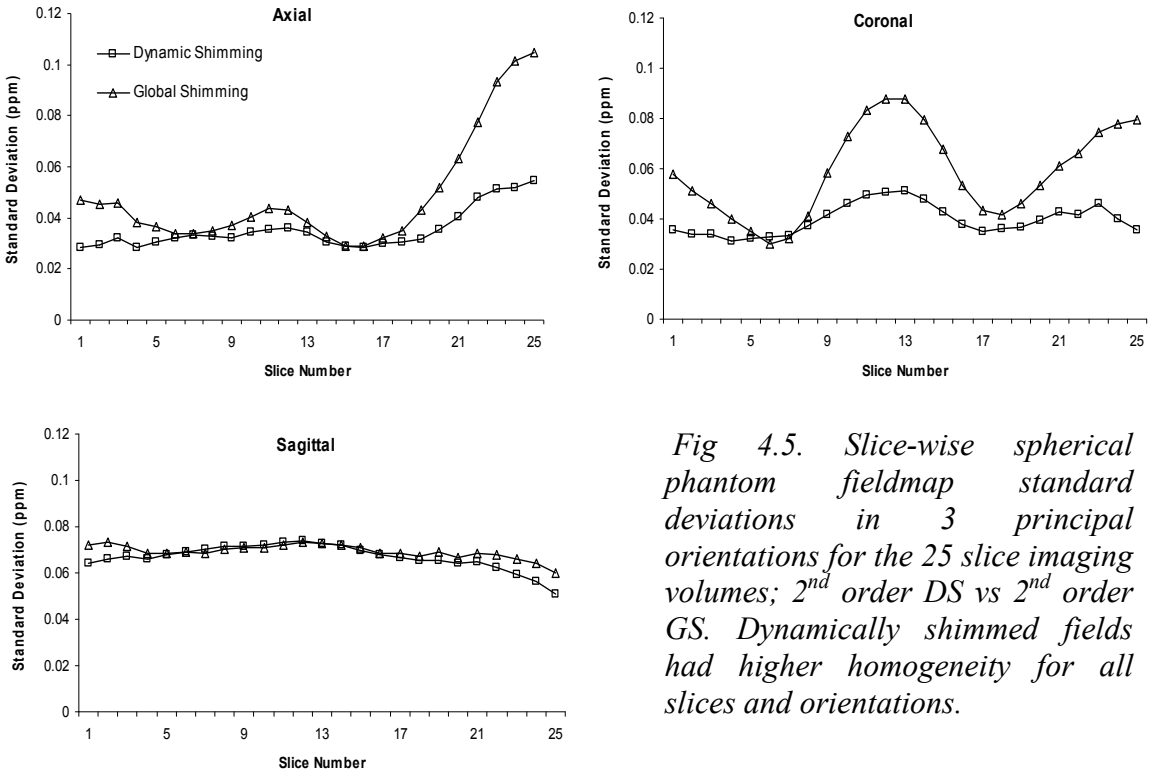

Fig 4.5. Slice-wise spherical phantom fieldmap standard deviations in 3 principal orientations for the 25 slice imaging volumes; 2nd order DS vs 2nd order GS. Dynamically shimmed fields had higher homogeneity for all slices and orientations.

250 mm FOV, 25 slices, first TE/ΔTE = 4/1 ms, slice thickness/gap = 3/1 mm for axials and 3/2 mm for coronals, total scan duration = 11.7 secs) were obtained for 12 subjects (10 axial and 4 coronal stack orientations, same orientation not repeated for any subject) with all shims zeroed. The fieldmaps were masked using skull stripping [Smith 2002] combined with an operator defined ROI to delineate the final shim region. Dynamic and global shimming coefficients were calculated and the shim switching module was loaded with the slicewise shim values. High resolution GRE images and fieldmaps (256 x 256 pixels, same image geometry as the fieldmaps, TR/ first TE/ΔTE = 820/20/1 ms, readout bandwidth = 1349 Hz/pixel, SENSE acceleration factor = 2) were acquired with DS and static GS conditions. The fieldmaps were evaluated by calculating the slice-wise standard deviations within the ROI. Since the distribution of the slicewise fields were quite often

seen to be non-normal, in addition to the standard deviation, the range covering the central 80% of pixel values (generalization of the interquartile range to the central 80%, as presented by Koch et al [Koch 2006]) and the fraction of nonzero field pixels greater than 50 Hz (0.167 ppm, corresponding to ~2.5 pixel inplane displacement at 19.4 Hz/pixel bandwidth) were also calculated within the entire multislice ROI as well as the whole brain.

To evaluate distortions arising from low bandwidth acquisitions in the presence of field inhomogeneity, single shot gradient echo axial EPI images were acquired with the same geometry, TR/TE = 2755/29 ms, SENSE acceleration factor R = 1, 128 x 128 pixels and phase encoding bandwidth = 19.4 Hz/pixel. The resulting images were rigidly registered using an inhouse rigid registration tool to the GRE images to eliminate bulk shifts arising from slice-wise base frequency (f0) offsets. Subsequently the images were non-rigidly registered to the GRE image using the multilevel Adaptive Bases Registration algorithm (ABA) [Rohde 2003], which yielded complete deformation maps of the two echo planar source images indicating inplane pixel shifts. The registration was constrained to the phase encoding direction only. The standard deviation of the pixel shift deformation map was calculated to yield a measure of the amount of distortion in the echo planar images. This method gives a more complete picture of distortion, based on measuring the mutual information between images, thereby capturing distortion information from the entire image as compared to only the edges or a single profile.

Results

Figures 4.6a and 4.6b display fieldmaps of five axial and coronal slices from different subjects. The shim ROI is the box shown in the 1st DS slice image, propagated to all the slices. Most of the slices show large reduction in field variation. Figures 4.6c and 4.6d show the slice-wise standard deviation of the field within the ROIs. We observed larger gains in fieldmap homogeneity with DS compared with GS in the inferior axial slices and the anterior coronal slices. In these locations, higher pre-shim field inhomogeneity variation was observed owing mainly to large susceptibility gradients caused by air–bone–tissue interfaces of the frontal sinuses and the ear canals.

Results from single shot echo planar imaging (SS EPI) showing image distortions are shown in Figure 4.7. Five axial slices with the image outlines from corresponding high bandwidth structural GRE images, superimposed for reference are displayed. Globally shimmed images have larger pixel shifts and extend further beyond and within the reference GRE outline. Areas of distortion correspond closely to their underlying fieldmap values (Figure 4.6a), with high positive field deviations causing pixel shifts to the left and vice versa (phase encoding was left – right). DS reduced distortions considerably, especially in the frontal areas of the brain which have high distortion when static 2nd order GS is employed. The above method of visualizing distortion provides only a qualitative estimate of the pixel shifts. Furthermore, it illustrates pixel shifts lucidly only for the edge pixels where the high bandwidth image edge may be referenced.

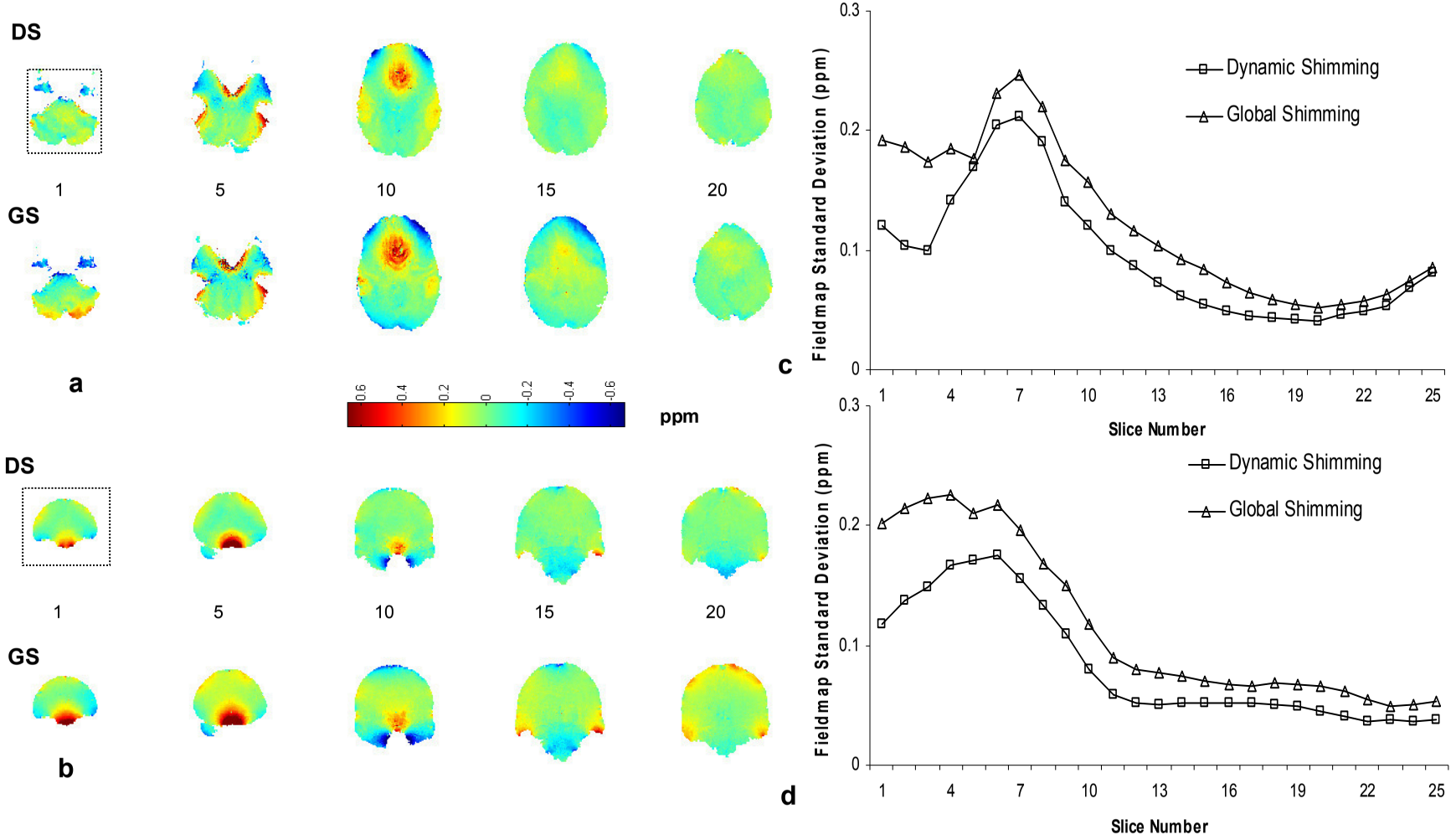

*Fig .4.6. B_0 fieldmaps in ppm of selected slices from 25 slice (**a**) axial and coronal (**b**) imaging volumes after 2nd order DS and 2nd order GS. Inplane ROIs are shown in the 1st DS fieldmap in both orientations, which extend to all slices. Slice numbers are shown in between. (**c & d**) Slice-wise fieldmap standard deviations in ppm of the same imaging volumes within the ROIs*

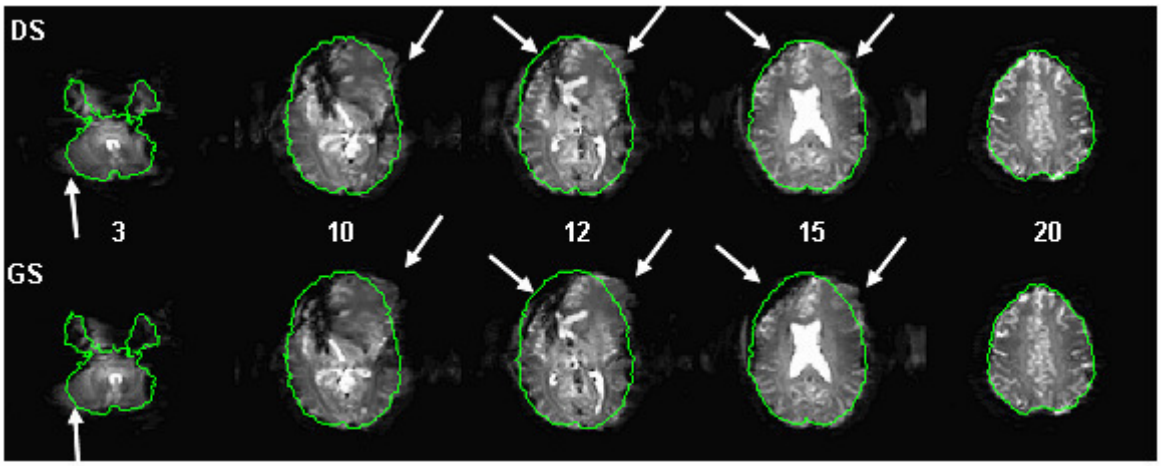

FIG.4.7. Single shot EPI geometric distortion comparison between 2nd order DS and GS acquisitions for selected axial slices (slice numbers indicated between the top and bottom rows). The green outlines derived from high bandwidth FFE images (not shown) serve as references. DS shows lesser distortions compared to GS, especially in the locations pointed out the arrows.

Figures 4.8a, b and c show results obtained from the ABA registration technique employed for holistic distortion evaluation for one slice (slice 15 in Figure 4.6a) with the corresponding GS and DS fieldmaps. Figure 4.8d shows the slice-wise standard deviation of the final pixel displacement maps, a measure of distortion obtained from the registration of the EPI images (phase encoding bandwidth = 19.4 Hz/pixel, phase encoding direction was right -left) to the high bandwidth low distortion GRE images. In the deformation maps that indicate the pixel displacement from the EPI to the GRE images, positive deformation values indicate pixel shifts to the right and negative values indicate shifts to the left. DS echo planar images had smaller pixel displacements in the phase encoding direction compared to GS images for all slices. Importantly, the deformation maps indicating pixel shifts correlated spatially to the underlying fieldmaps. Also, the magnitude of the pixel deformation agreed with the ΔB_0 value at the given phase encode bandwidth (as per Eq. 2.8) validating the method and giving a good measure of distortion.

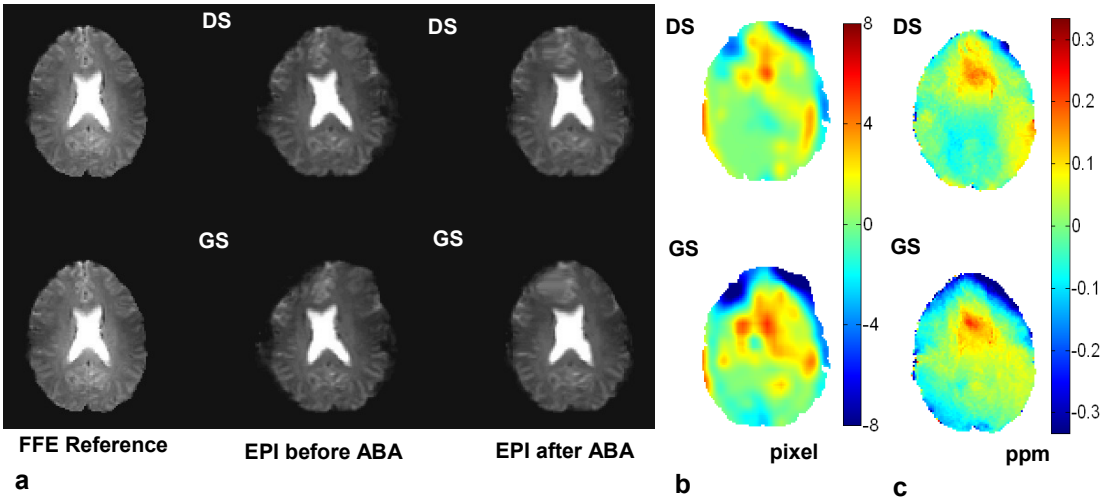

*Fig 4.8. EPI deformation analysis by registration (**a**) Slice 15, DS and GS images, before and after ABA registration. (**b**) Deformation map from EPI to FFE. + ve = shifts to the right, -ve = shifts to the left. (**c**) Fieldmap for the same slice. (**d**) Slicewise standard deviations of in-plane pixel displacement maps. DS EPI images show much smaller pixel displacements in almost all slices compared to GS images.*

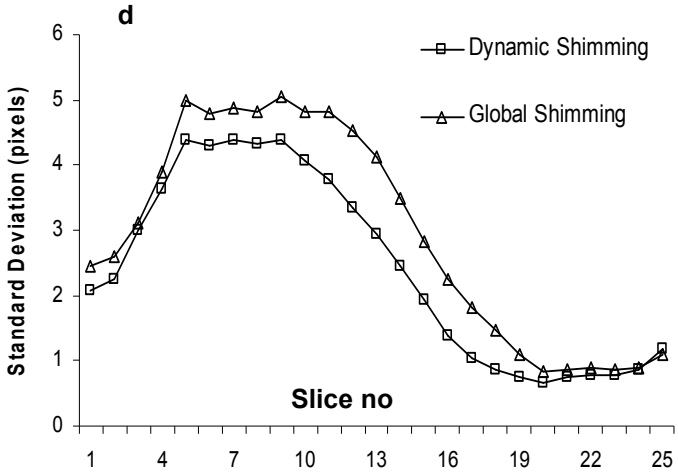

Figures 4.9a and b give estimates of the field flattening in the entire multislice shim ROI and the whole brain after DS and static GS in terms of field standard deviation, the central 80% pixel value range and the fraction of nonzero field value pixels greater than 50 Hz (Mean +/- 95% confidence interval). As shown, DS improved all three measures of field inhomogeneity over both the shim ROI and the whole brain.

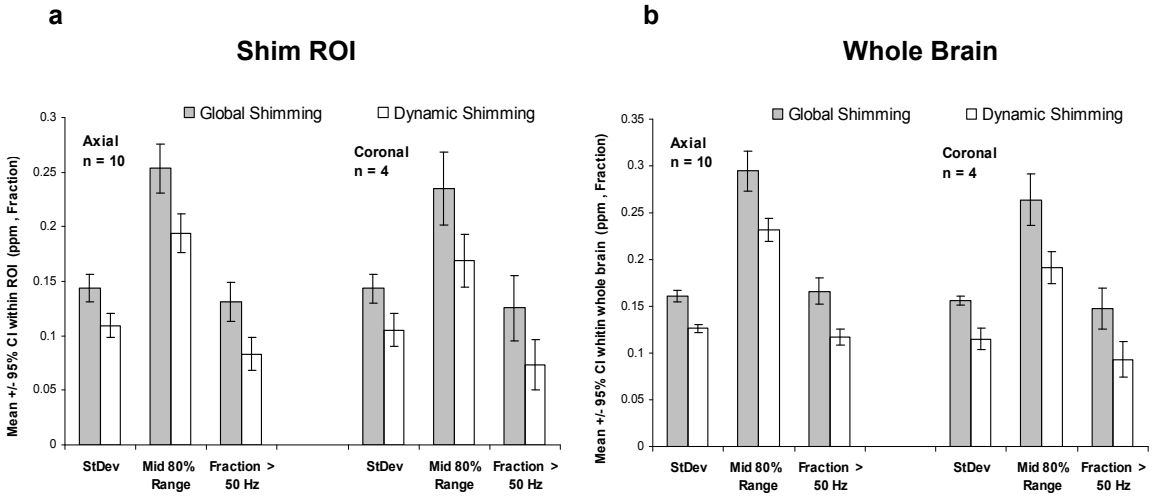

*Fig. 4.9. B_0 field homogeneity measures (Mean and 95% CI) after 2nd order DS and GS (12 subjects, 10 axial, 4 coronal) calculated within (**a**) the shim ROI and (**b**) the whole brain. Homogeneity measures include standard deviation, the central 80% pixel range and the fraction of nonzero field value pixels greater than 50 Hz (0.167 ppm, corresponding to ~2.5 pixel inplane displacement at 19.4 Hz/pixel bandwidth).*

4.4. Signal simulations and T_2^* measurements

The studies presented above were performed with the degeneracy analysis for slice-wise shim calculation as has been adopted in previous implementations of slice-wise dynamic shimming reported in literature [Koch 2006, Poole 2008]. Our results are consistent with the results of these earlier studies, confirming the benefits of DS over GS in improving the *in-plane* field inhomogeneity over extended volumes at high field. However, the question of through plane inhomogeneity which is often a major contributor to the intravoxel signal loss has not been addressed adequately. Signal loss is related to the strength of the intravoxel gradients. In GS, the signal loss can be estimated directly from the measured fieldmap by calculating the voxelwise field gradients. However, for DS, the residual fields as measured above do not provide the estimates for the through slice field gradients. This is because the final residual multislice field no

longer retains the information on the through slice field present at the time of slice acquisition. One may be able to obtain that information by acquiring the entire volume once for every slice field setting. Such an approach is obviously not efficient. The estimation of the signal improvement therefore, has to be performed directly from the images or from T_2^* maps obtained by multi-echo imaging. In this section, we present simulations and imaging studies performed to investigate this aspect of dynamic field correction.

Slice-wise shim calculation with the degeneracy analysis assumes the through slice field gradient to be linear. This is because the application of a higher order shim for the through slice correction after the inplane field has been optimized disturbs the inplane field correction. A linear through slice correction may be acceptable in thin (how thin remains an unsolved question) slices, but as the slice thickness is increased, this assumption does not hold true. For thicker slices, the through slice gradient may well be of 2^{nd} or higher order in places. Consequently, the through slice field gradients may not be adequately compensated by this method leading to signal losses. Increase in the slice gaps exaggerates the problem as even though the through slice signal loss does not decrease in itself (since it depends on the voxel size), the estimation of the through slice field is compromised due to sparser sampling.

One approach to overcoming this drawback is to optimize the slicewise fields based on the voxel signal itself. We have noted the optimization functions that can be used for this approach in section 3.4.2. In the following studies we have utilized the signal formulation in Eq 2.6 to maximize the intravoxel signal. The degeneracy analysis has not been included for the signal optimization.

Methods

Fieldmaps were acquired for the whole brain in the axial orientation with the same parameters as reported previously for 3 subjects. (25 slices, 64 x 64 matrix, slice thickness/gap = 3/1 mm, first TE/ΔTE = 4/1 ms). Post shim fields were simulated as described earlier with 2nd order DS and 2nd order GS. For 2nd order DS, two different optimization routines were employed

1. Least squares calculation using the degeneracy approach assuming a linear though slice gradient.
2. Nelder-Mead simplex algorithm (fminsearch in Matlab 2008a, Lagarias 1998) for minimizing the number of pixels in the slice of interest having signal less than 95% of the peak signal. We used the 95% threshold arbitrarily. The peak signal is calculated from Eq 2.6 assuming the intravoxel gradients and TE to be 0. The optimization was performed using all the 2nd order shim terms, thereby allowing 2nd order through plane correction.

The intravoxel gradient optimization routine was considerably more time consuming than the least squares field optimization. It was also sensitive to starting conditions. To limit the convergence time required for the technique, two modifications were added. First, a least squares optimization using the set of 3 slices was performed prior to the gradient optimization to provide a rapid initial estimate for the shim values. Second, the Z0 term was not optimized as it did not contribute towards the field gradient and was calculated from the shim corrections later. These modifications reduced the time of convergence

from around 6 minutes to less than a minute for the 25 slice volume on a 1.6 GHz processor machine. 3 slice post shim volumes centered on the slice of interest were simulated for every slice, yielding a 64x64x25x3 post DS matrix. After shimming, slicewise signal maps were calculated from the above volumes using Eq 2.6 for TE = 10 ms.

T_2^* measurements were performed in the scanner with each of the above shimming methods to provide an estimate of the signal loss. A multiecho GRE sequence was used for getting signal decay samples (TR/first TE/ΔTE = 723/1.38/3 ms, 8 echoes, voxel size 3.9 x 3.9 x 3 mm). Voxelwise T_2^* values were calculated by the scanner's built-in algorithm [Dahnke 2005]. Post shim fieldmaps were also measured in the scanner at the same resolution to evaluate and compare inplane field improvements with the three methods.

Results

Figure 4.10 shows results from the signal simulations. Figure 4.10a shows normalized signal maps of six slices spanning the 25 slice volume for one subject. The signal optimized DS maps show higher signal compared to the two other shimming methods. DS with the degeneracy analysis (DS2_NDG) reveals greater signal loss in most slices, indicating that the 1st order through slice gradient assumption may be inaccurate, at least at the given slice geometry. Figure 4.10b and c show the histogram and cumulative sum plots of the signal maps over the entire 25 slice volume for pixels having greater that 80% of the maximum signal at the TE of 10 ms considered. DS by

signal optimization is clearly seen to yield a larger number of pixels with higher signal than both the other methods.

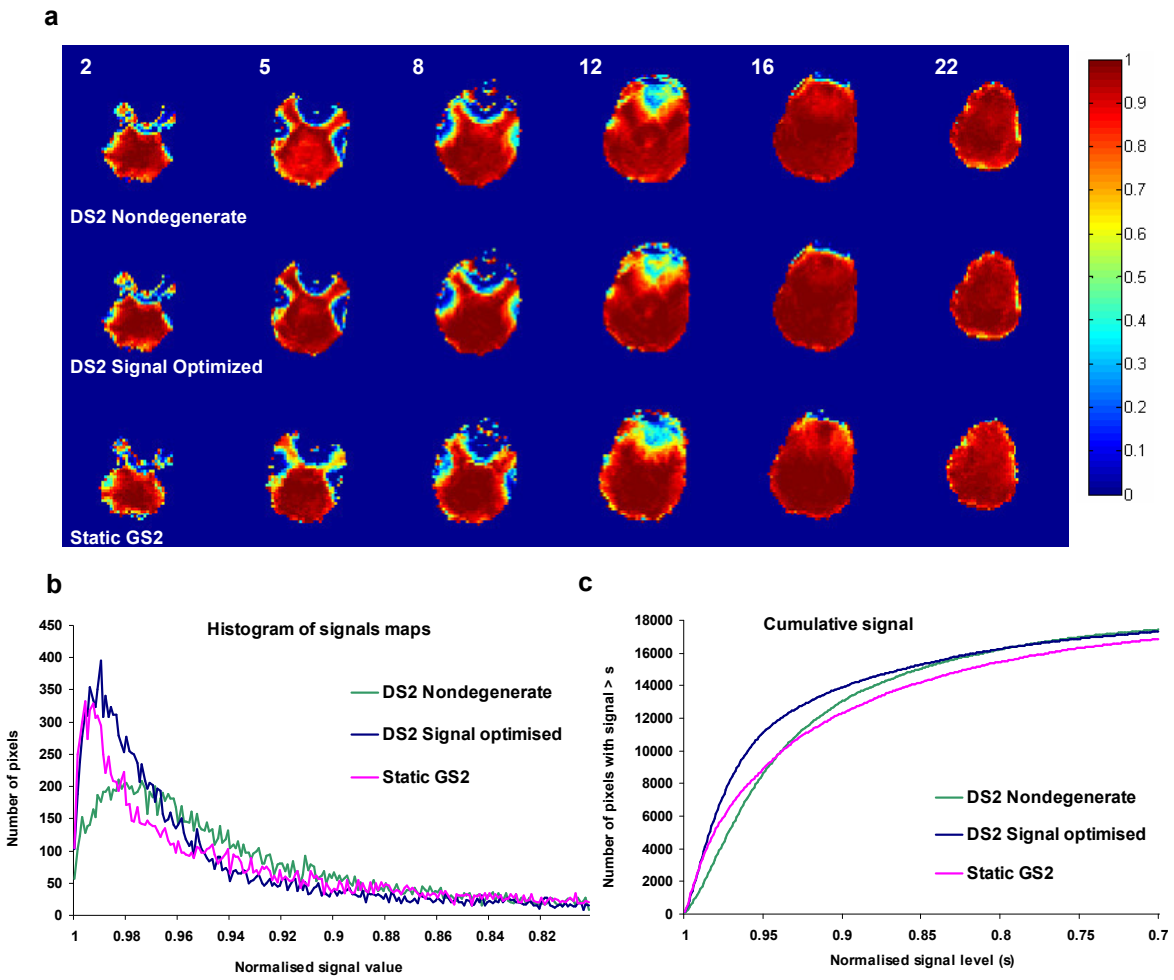

Fig. 4.10 Signal Simulation results. (a) Simulated signal maps at TE = 10 ms normalized to the maximum signal. DS2 with degeneracy analysis (top row), DS2 with signal optimization (mid row) and static GS2 (bottom row). Signal optimized DS2is predicted to considerably improve signal compared to DS2 with degeneracy analysis and GS2. (b) Histogram of whole volume signal maps, showing greater number of pixels with higher signal when slicewise signal is optimized (c) Cumulative histogram of the same.

Figure 4.11a shows T_2^* maps obtained from the multiecho GRE sequence for slices shown in Figure 4.10a while Figure 4.11b show signal ratio maps calculated from the T_2^* value as

$$S / S_0 = e^{-t/T_2^*} \ , \ t \ = \ 10\,ms$$

Both the T_2^* and the signal ratio maps show a reasonable correlation with the simulated signal maps in Figure 4.10a. For example, in slice 5 the frontal temporal lobes exhibit low signal in the simulated maps with GS, while the posterior areas have low signal in

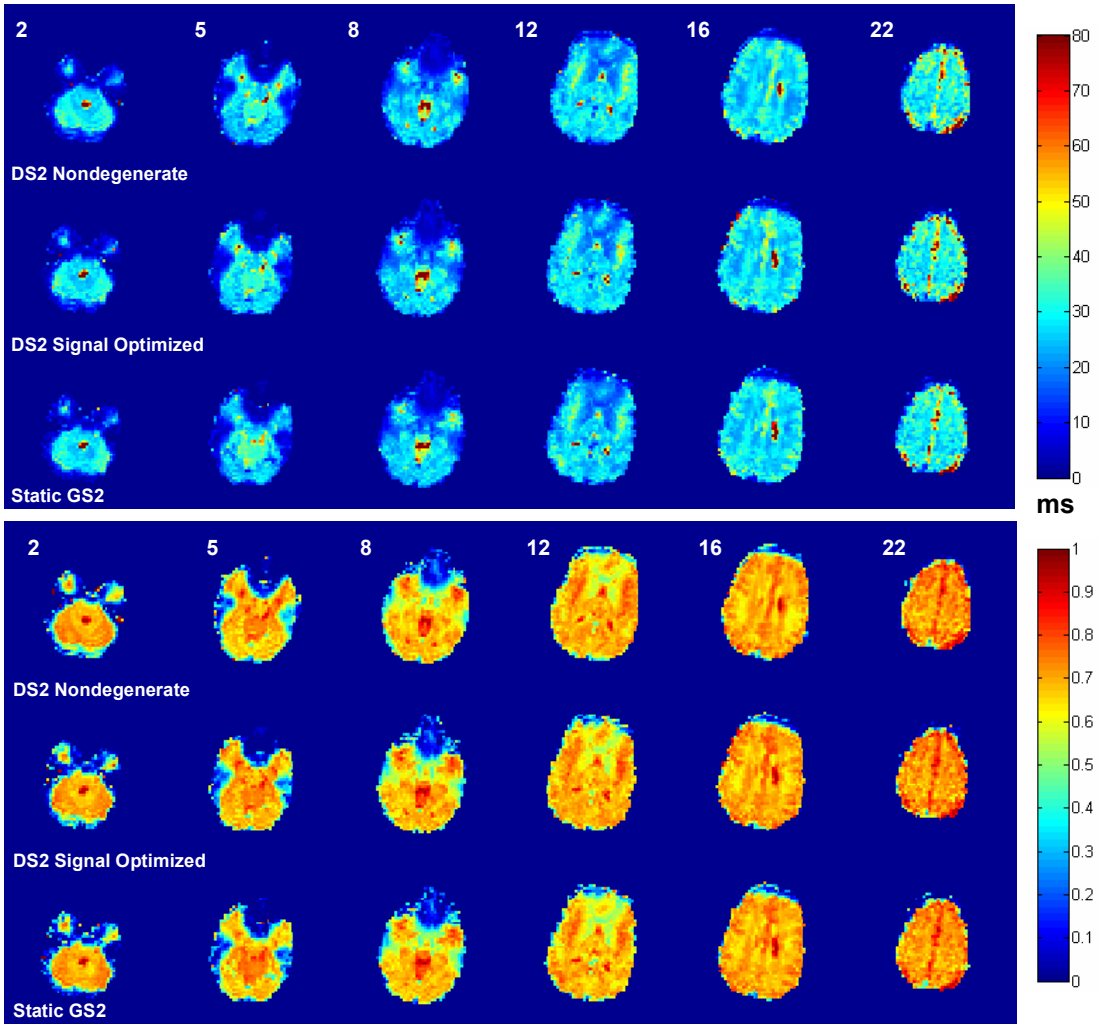

Fig. 4.11 Maps of T_2^* (top) and Normalized signal (bottom) obtained from the multiecho GRE data with the three shim types.

the DS2_NDG shim technique. These patterns are reflected in the corresponding measured T_2^* and signal ratio maps. Figure 4.12 shows the cumulative T_2^* histograms of the three shim techniques upto 50 ms. A shift towards the right in the cumulative plot with the signal optimized DS method relative to the other two methods indicates that the least number of pixels lie below any given T_2^* value in the maps obtained with the former technique.

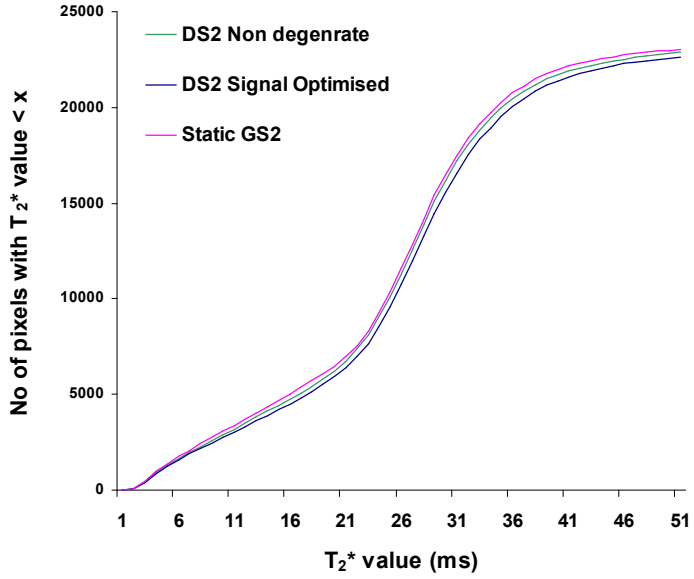

Fig. 4.12 Cumulative histogram of the T_2^* values with the three shim techniques.

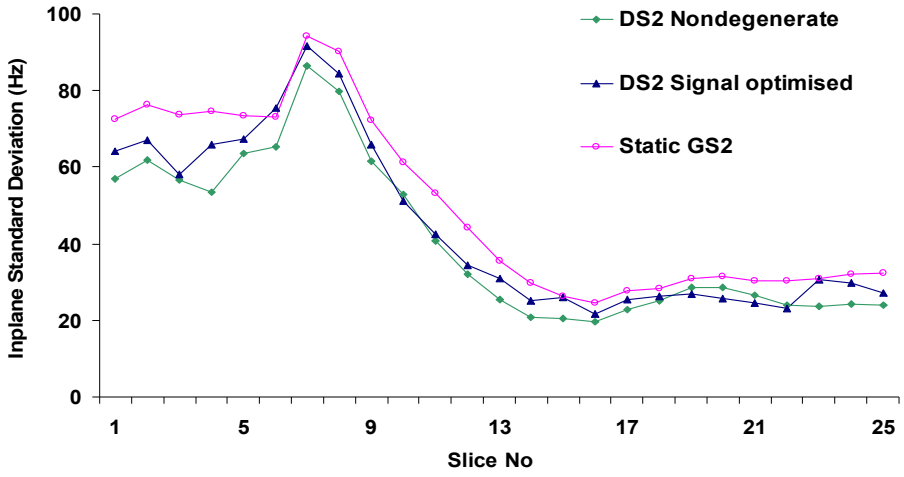

Fig. 4.13. Post shim in-plane field slicewise standard deviations for the three methods.

Figure 4.13 shows the slicewise inplane field standard deviations obtained by the three methods. The DS approach with the degeneracy analysis performs the best in all slices. This is expected as this approach optimizes the inplane field using data from the slice of interest only. The signal optimized dynamic shim is seen to compromise on the inplane field correction. However, it is still seen to have higher in-plane residual homogeneity than the static GS method. In view of the signal recovered, a slight compromise on the inplane field and hence image distortion may be acceptable. With the advent of parallel imaging techniques with ever increasing acceleration factors and the availability of reasonably robust prospective and retrospective distortion correction methods, the problem of image distortion may be considered less critical than signal loss. This is underscored by the fact that increasing acceleration causes higher signal loss due to increase in their geometry factors even while improving distortions.

The results of the T_2^* measurements presented above show a slight increase in signal recovery when using the signal optimized DS method, compared to the other shimming methods. However, these results do not entirely agree with the simulated results which predict higher differences. One reason for this might be eddy currents caused by switching of all the higher order shims. Further studies are required to perfect this optimization technique and accompanying data processing methods to reconcile the measurements with simulations and extract the maximum signal recovery.

4.5. Shim induced eddy field measurements

Rapid switching of unshielded shims can generate severe eddy currents in the conducting structures of the magnet, which produce eddy current fields that degrade

image quality. The first order shims driven by the gradient channels, are actively shielded, have pre-emphasis and therefore produce only minimal eddy currents. The higher order shims, however, can produce substantial same order and lower order eddy currents. We characterized the eddy currents produced by the switching of 2nd and 3rd order shims using the method of Terpstra *et al.* [Terpstra 1998] adapted for shims instead of first order gradients. The method employs a stimulated echo acquisition mode (STEAM) imaging sequence shown in Figure 4.14 to selectively excite a bar along a given direction. [Frahm 1985, 1987]

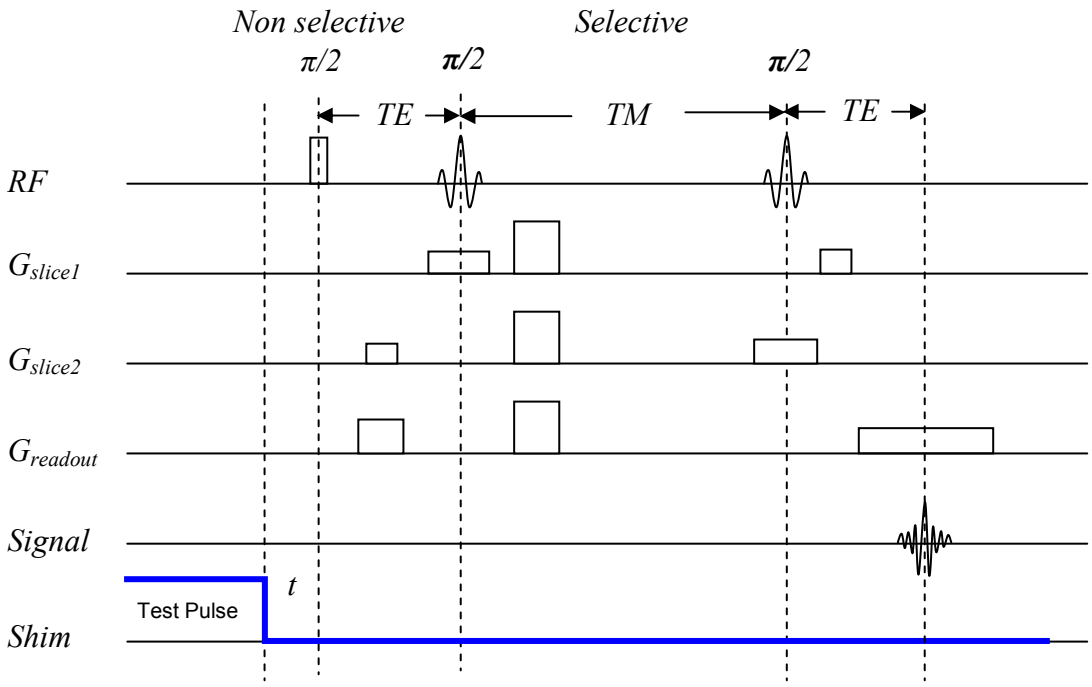

Fig 4.14. Stimulated echo imaging (STEAM) pulse sequence for shim localization in shim eddy current measurement.

A bar was excited in the spherical "braino" phantom, along the direction where the shim of interest produced the maximum field (e.g., 45° about the Z axis for a XY shim). A 1A test shim pulse was turned on for 5 seconds and then turned off. Phase data

were collected after waiting exponentially increasing amounts of time (t in Figure 4.14) in every TR, with phase encoding gradient set to zero. (FOV 300 mm, bar length 300 mm, bar width 20 mm, TE = 15 ms, Mixing Time = 100 ms, time after pulse switch off = 5 + phase encode line number $^{1.8}$ ms, TR = 3000 ms). Phase measurement was performed once with the shim pulsed and once without, for reference data. Phase versus time maps, i.e. phase along the excited bar for every time point, were obtained by unwrapping the phase data spatially and subtracting the reference map. Every time point phase data along the bar from these maps were then fit to a combination of the switched shim and lower order shims i.e. 0^{th}, 1^{st}, 2^{nd} orders for the 2^{nd} order shims and 0^{th} through 3^{rd} order, for the 3^{rd} order shims such that

$$\frac{\Delta\phi(r)}{TE} = \gamma B_{eddy}(r,t) = \gamma B_0(t) + \gamma \sum_n G_{shim}(t)\, r^n \qquad (4.1)$$

Eddy field decay amplitudes and time constants for each of these field harmonics were then determined by fitting the data ($B_0(t)$ *and* $G_{shim}(t)$) for each of these harmonics to a sum of up to 3 exponential decay functions representing short, medium and long time constants such that

$$G(t) = \sum_{i=1}^{3} A_i\, e^{-t/TC_i} \qquad (4.2)$$

Using a STEAM based imaging approach enabled the rapid and easy measurement of the shim induced eddy currents. Free induction decay based measurement approaches would require careful and tedious placement of small samples in space. Such a procedure would

be error prone and time consuming. Alternatively, a water sample tube could also be used with a properly adjusted holding frame to do the same measurement. The imaging based approach is however considerably easier to implement, flexible and much faster. The measurement for a single shim channel including the reference scan could be performed within 10 minutes.

Results

Eddy currents from shielded and pre-emphasized first order gradients were not probed as gradient switching for those terms are already compensated. Most 2nd order shims were seen to produce decaying B_0 and self eddy fields following shim switch, while XY and X2-Y2 shims produced additional minor 1st order fields. Of the 2nd order shims, the unshielded Z2 coil produced the largest B_0 variations per Hz/cm^2 of shim field.

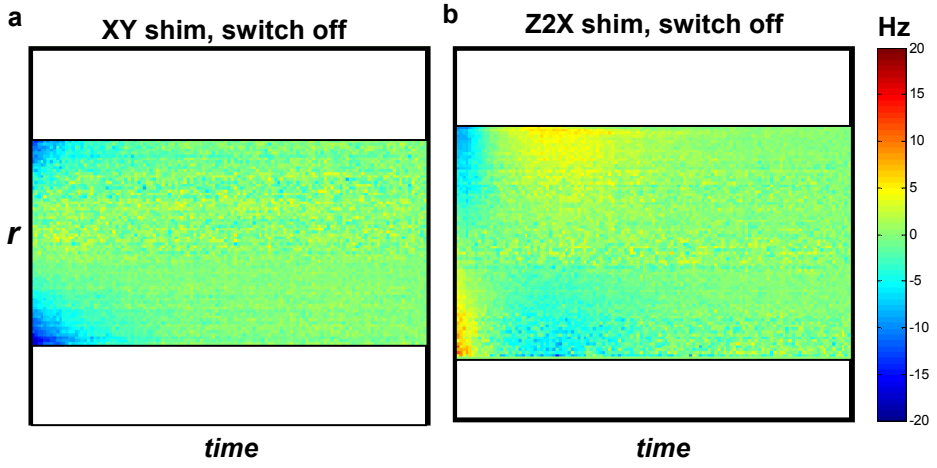

Fig 4.15. Frequency time maps of XY and Z2X shim induced eddy fields along the excited bar showing field decay with time.

Figure 4.15a and b illustrate frequency time maps obtained after switching off XY and Z2X shim pulse. The XY decay map reveals a predominantly 2nd order

component monotonically decaying while the Z2X map shows an oscillating 1st order field. Figure 4.16a shows an example of a XY shim eddy field decaying with time after a step change of ±1Amp (±3.13 Hz/cm^2). Third order shims produced smaller B_0 variations than 2nd order shims, but they coupled very strongly with 1st order gradients, with long time constants ranging from hundreds of milliseconds to a few seconds. Figure 4.16b shows the X gradient eddy decay observed after 1Amp switching of the Z2X shim, illustrating the long time required for the gradient field to decay. The longest time constants for the 3rd order shim were found to be, in general, longer than those for the 2nd

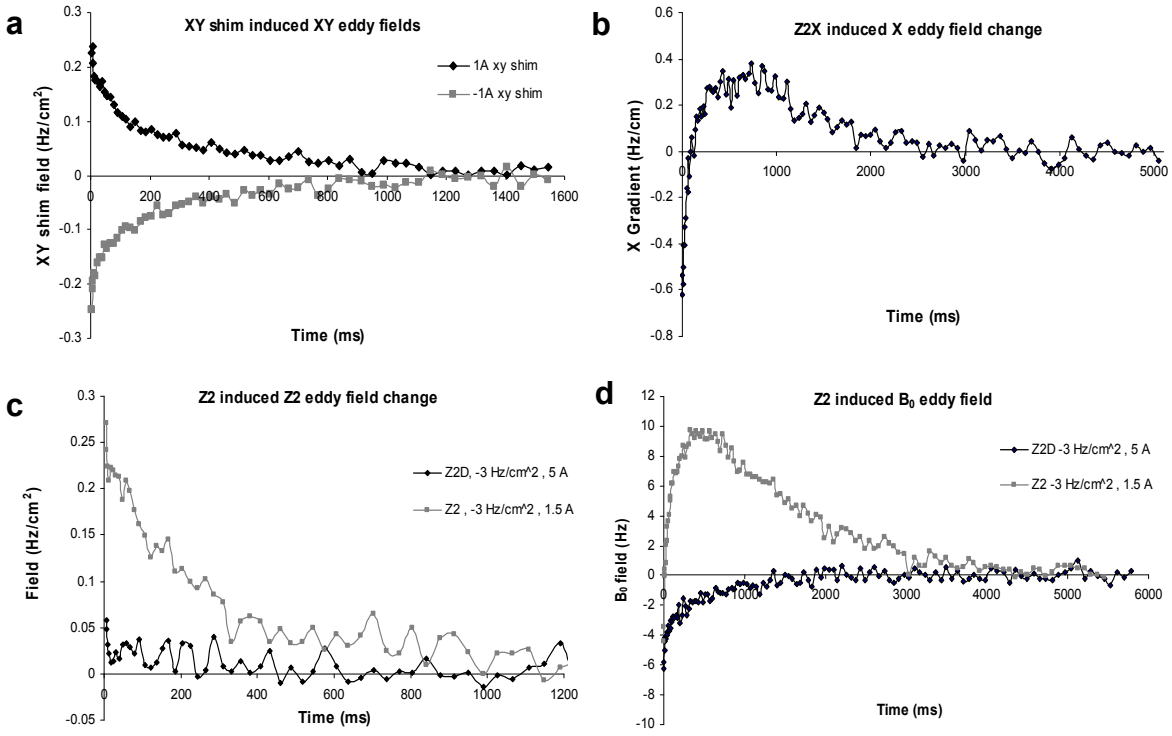

*Fig.4.16. Eddy current results (**a**): Eddy field decay after switch OFF of a XY shim pulse from 1 and -1A (3.13 Hz/cm^2 /A). The shim component reduces to non significant levels around 1000 ms after shim turn off. (**b**) X shim eddy field produced by switching off the 3rd order Z2X field from 1A (-0.0155 Hz/cm^3 /A) (**c & d**) Z2 and B0 eddy fields produced by switching the unshielded Z2 (-1.97Hz/cm^2 /A) and Z2D (-0.58 Hz/ cm^2 /A) coils from -3Hz/cm^2 to 0 Hz/cm^2. Z2D coil is seen to produce much smaller field variations after switching than the unshielded Z2 coil as expected.*

Shim (Hz/cm^n/A)		B0 Amplitudes(Hz) & Time Constants (ms)			1st Order Amplitudes(Hz/cm) & Time Constants (ms)			Self Shim Amplitudes(%) & Time Constants (ms)		
		TC1	TC2	TC3	TC1	TC2	TC3	TC1	TC2	TC3
XY	Amp	2.22	-2.94	2.04		-0.09	-0.06	9.23	5.11	1.29
3.1300	Time	4.45	25.73	107.22		22.12	368.17	4.45	25.73	107.22
X2-Y2	Amp			-2.39			-0.12	0.77	6.38	5.32
3.2000	Time			104.66			705.57	0.58	5.46	310.47
ZY	Amp								2.06	2.16
-3.3000	Time		NS			NS			17.50	447.19
ZX	Amp	-1.35	2.07	-0.46						2.40
3.3500	Time	21.14	54.12	368.83		NS				228.21
Z2	Amp	-18.51	-10.59	10.73				32.00	0.47	7.39
-1.9700	Time	2.92	207.52	1247.81		NS		1.52	19.89	308.81
Z2D	Amp	-4.60	-0.27	-0.70					3.28	0.70
-0.5800	Time	1.92	47.06	596.79		NS			4.62	617.66
Z3	Amp	1.58	-1.77	0.33	-0.28	-0.25	0.33			4.12
-0.0125	Time	12.09	271.86	805.12	88.49	208.71	1002.38			623.71
Z2X	Amp	11.87	-2.10	1.32	-0.52	-1.66	1.51	5.40	3.16	6.51
-0.0155	Time	1.39	323.62	670.30	38.13	362.81	687.56	8.64	39.55	377.38
Z2Y	Amp	0.77	-2.08	0.80	-0.50	-1.28	1.15			
-0.0151	Time	6.81	40.29	259.31	26.19	381.08	694.48		NS	
Z(X2-Y2)	Amp		-0.99	0.90			-0.08	0.68	3.78	2.87
0.0985	Time		98.60	429.14			84.91	3.17	43.87	795.20
ZXY	Amp				0.17	-0.15	0.04	1.39	6.19	2.45
0.0974	Time		NS		6.57	93.84	941.92	28.75	400.14	1969.54
X3	Amp		-0.22	-0.77			-0.13		1.06	6.72
0.0453	Time		10.03	339.91			987.98		3.18	97.13
Y3	Amp		-4.61	0.64					4.86	10.28
0.044	Time		63.42	2562.41		NS			43.12	263.80

NS : Not Significant.

Table .4.1. 2nd and 3rd order shim eddy current Amplitudes and Time constants, given per Ampere of shim switch.

order shims, except for the unshielded Z2 coil. Many of the eddy fields were also observed to have reversing polarities as seen in Figures 4.16b and 4.16d. Some of the measurements revealed a very rapidly decaying initial component with time constant less than a millisecond. However, these signals were not perfectly reproducible, most likely owing to the slight shim DAC update time variation. With better control of the shim ramp and DAC update times it might be possible to characterize these signals more accurately. The unshielded Z2 shim coupled strongly to B_0, producing large long time constant variations in the main magnetic field. Figures 4.16c and 4.16d show the decay of the self eddy field and B_0 when Z2 and Z2D coils are switched off from a value of -3Hz/cm^2 (1.5 and 5 Amperes for the Z2 and Z2D coil respectively). The Z2D coil generated a smaller and faster decaying B_0 and self eddy fields compared to the Z2 coil, as expected. Table 4.1 compiles the amplitudes and time constants from all the shims in our system, which can be used to calibrate eddy current compensation circuits.

4.6 Orderwise comparisons of shim types

To investigate the relative benefits of increasing orders of global and dynamic shimming in whole brain experiments and also to identify shimming techniques that may yield improvements in static GS without the need for dynamic higher order shim switching hardware, a separate set of human experiments was conducted. In addition to standard global and dynamic shimming, a hybrid shim approach was employed in which 1st order shims were switched dynamically on top of a static global 2nd or 3rd order shim (GS2DS1 or GS3DS1). Shim calculation for this technique followed the standard GS calculation described previously with residual slicewise first order field corrections

calculated and added for each slice dynamically during the scan using the imaging gradients. Such a technique required no additional scans, an insignificant time penalty (additional 1st order shims were obtained within ~10 seconds for a 25 slice volume on a 1.6 GHz processor machine) and was expected to yield better shim performance than a static global shim, without the use of any higher order dynamic shim switching hardware. Such an approach could therefore be employed in any scanner. 7 shim types were investigated including GS1, GS2, GS2DS1, GS3, GS3DS1, DS1 and DS2 where the number refers to the order of the shim. Only DS2 required the RTS. GRE field mapping experiments as described previously were carried out in the axial and coronal orientations (axial n = 7, coronal n = 5, 128 x 128 pixels, 25 slices TR/first TE/ΔTE = 320/10/1 ms, slice thickness/gap = 3/1 mm for the axials, 3/2 mm for the coronal, 250 x 250 mm FOV, SENSE acceleration factor = 2) for each of the 7 shim types. Fieldmaps were analyzed for shim performance with the full volume metrics described previously (field standard deviation, the central 80% pixel value range and the fraction of nonzero field value pixels greater than 50 Hz) calculated over the whole brain. To evaluate the significance of differences in the 2nd and higher order shims (GS2, GS2DS1, GS3, GS3DS1 and DS2) a Repeated Measures Analysis of Variance (ANOVA) was performed on the 5 groups, with post hoc paired t tests at $\alpha = 0.05$. A conservative Bonferroni correction was applied on the post hoc tests to account for the multiple testing. We did not include the 1st order shims in the test as most scanners already possess and routinely use 2nd order static shims at the least if not 3rd order. Moreover, 2nd order shims have been previously shown to perform significantly better than 1st order shims in many studies [Jaffer 1996, Zhao 2005, Koch 2006, Poole 2008].

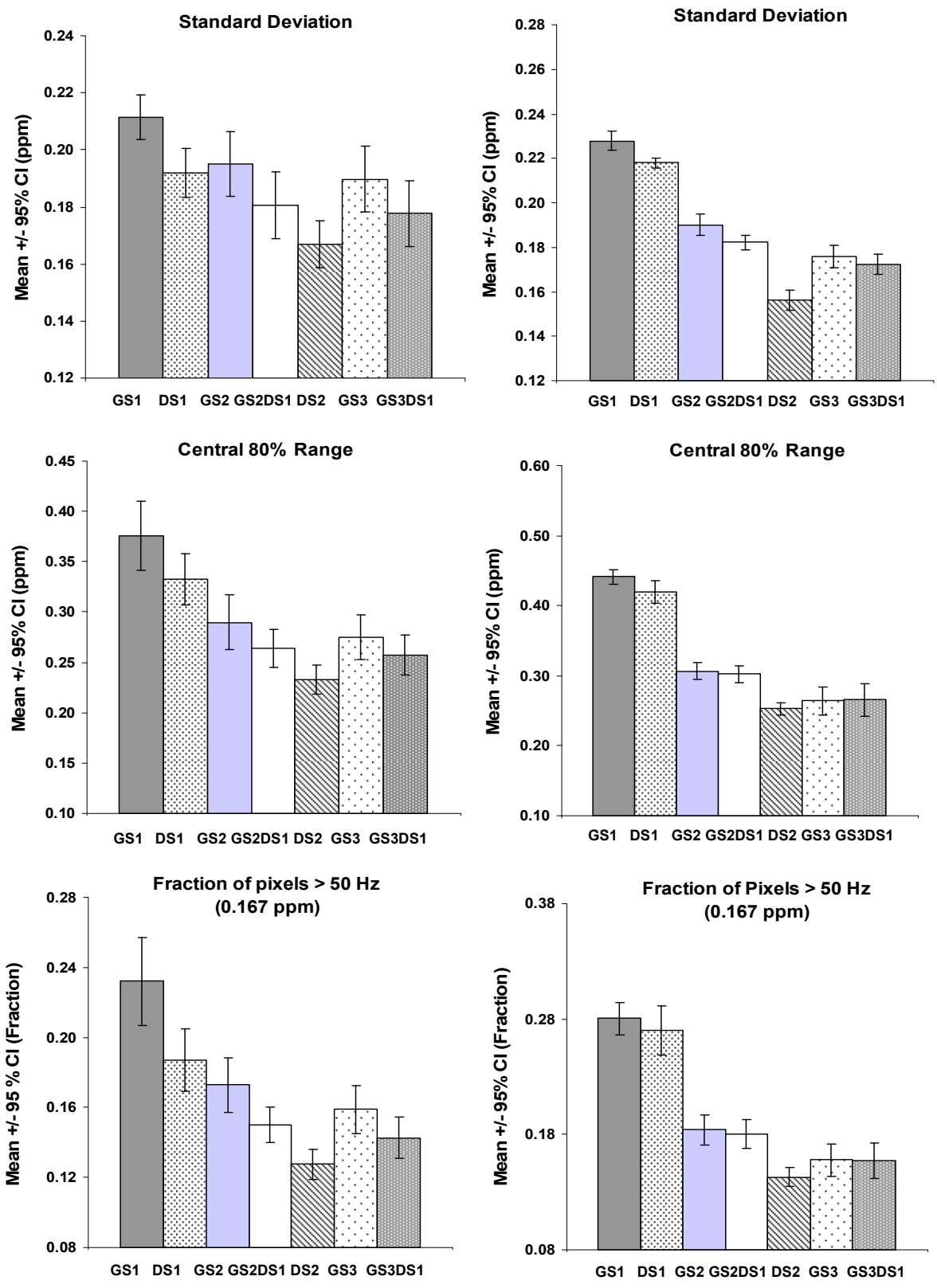

Fig .4.17. Results from Orderwise comparison of shims including 1st and 2nd order GS and DS (GS1,GS2,DS1,DS2) and two combined shims (GS2DS1 and GS3DS1) for 7 axial and 5 coronal subjects. Axial: Right Column, Coronal: Left Column.

Results

Figure 4.17 shows the results of shim order comparison in axial and coronal orientations. As predicted, the shim performance measured by the volume standard deviation, central 80% range and the fraction of pixels > 50 Hz over the whole brain

Axial

STDEV	GS2	GS2DS1	GS3	GS3DS1	DS2
GS2		*		*	*
GS2DS1	*		*		*
GS3		*		*	*
GS3DS1	*		*		
DS2	*	*	*		

80% IQR	GS2	GS2DS1	GS3	GS3DS1	DS2
GS2					*
GS2DS1					*
GS3				*	*
GS3DS1			*		
DS2	*	*	*		

FRAC> 50Hz	GS2	GS2DS1	GS3	GS3DS1	DS2
GS2		*		*	*
GS2DS1	*				*
GS3				*	*
GS3DS1	*		*		*
DS2	*	*	*	*	

Coronal

STDEV	GS2	GS2DS1	GS3	GS3DS1	DS2
GS2		*	*	*	*
GS2DS1	*		*	*	*
GS3	*	*			*
GS3DS1	*	*			*
DS2	*	*	*	*	

80% IQR	GS2	GS2DS1	GS3	GS3DS1	DS2
GS2			*	*	*
GS2DS1					*
GS3	*				
GS3DS1	*				
DS2	*	*			

FRAC> 50Hz	GS2	GS2DS1	GS3	GS3DS1	DS2
GS2			*	*	*
GS2DS1			*	*	*
GS3	*	*			
GS3DS1	*	*			
DS2	*	*			

Table 4.2: Post hoc test results showing statistical significance (implies significant at α = 0.05 with Bonferroni correction) between individual shims with the three measures.*

improved with increasing shim order for both axial and coronal orientations and matched the simulation results presented in section. In both orientations 2nd order DS performed the best, even when compared to 3rd order GS while 1st order GS had the most residual inhomogeneity. Greater improvements were observed in going from 1st to 2nd orders in the coronal orientation than the axial orientation for DS. 2nd order GS performed better than 1st order DS in coronal orientation according to all three measures.

The repeated measures ANOVA revealed significant differences in the set of 5 shims types tested ($p < 0.01$). Table 4.2 shows the results of post hoc tests with Bonferroni correction. Importantly, the combined global and dynamic shimming

techniques GS2DS1 and GS3DS1 implemented without any higher order shim switching hardware improved field homogeneity significantly over 2nd and 3rd order GS by almost all the measures. Greater improvements were observed in the axial orientation. The highest improvements were observed in the inferior axial slices where strong linear residual fields post 2nd order GS (Figure 4.6 a, c) were compensated for by the slicewise additional 1st order dynamic corrections. Similar improvement was not achieved in the coronal orientation indicating the presence of primarily higher order residual fields post GS. These results demonstrated that GS2DS1 and GS3DS1 were options which could improve field homogeneity over static GS2 and GS3 without the use of real time shim switching hardware. Significant differences between DS2 and GS3DS1 (the best one could do without the use of time higher order shim switching) were seen in only two measures, the fraction > 50 Hz in the axial and standard deviation in the coronal orientation. Results shown in Figure 4.17 however suggested that DS2 did improve field homogeneity over GS3DS1 as quantified by all three paratmers.

4.7 Artifacts in uncompensated DS

In the previous sections, the results of experimental evaluation of DS on a high field imaging system have been presented. DS was shown to yield lower residual field inhomogeneity, lower distortion and higher residual signal than image based static GS These results are consistent with earlier studies of DS at lower field strengths. However, all the experiments reported here, including the SSEPI studies were performed using unshielded (except for the shielded Z2) and uncompensated higher order shims. While the present setting yielded artifact free images with the imaging parameters used,

specifically SS EPI at TR/TE = 2755/29 ms, 25 slices and SENSE acceleration factor = 1, pushing the limits of these factors led to severely increased ghosting and SENSE reconstruction artifacts.

As TR was reduced, number of slices increased, SENSE factor increased and the range of pre-shim ΔB_0 increased (leading to higher shim demands), ghosting artifacts became predominant, severely hampering image quality. The artifacts were seen to be severe even with the use of the shielded Z2 coil. Examples of artifactual SSEPI 2nd order DS images are shown in Figure 4.18.

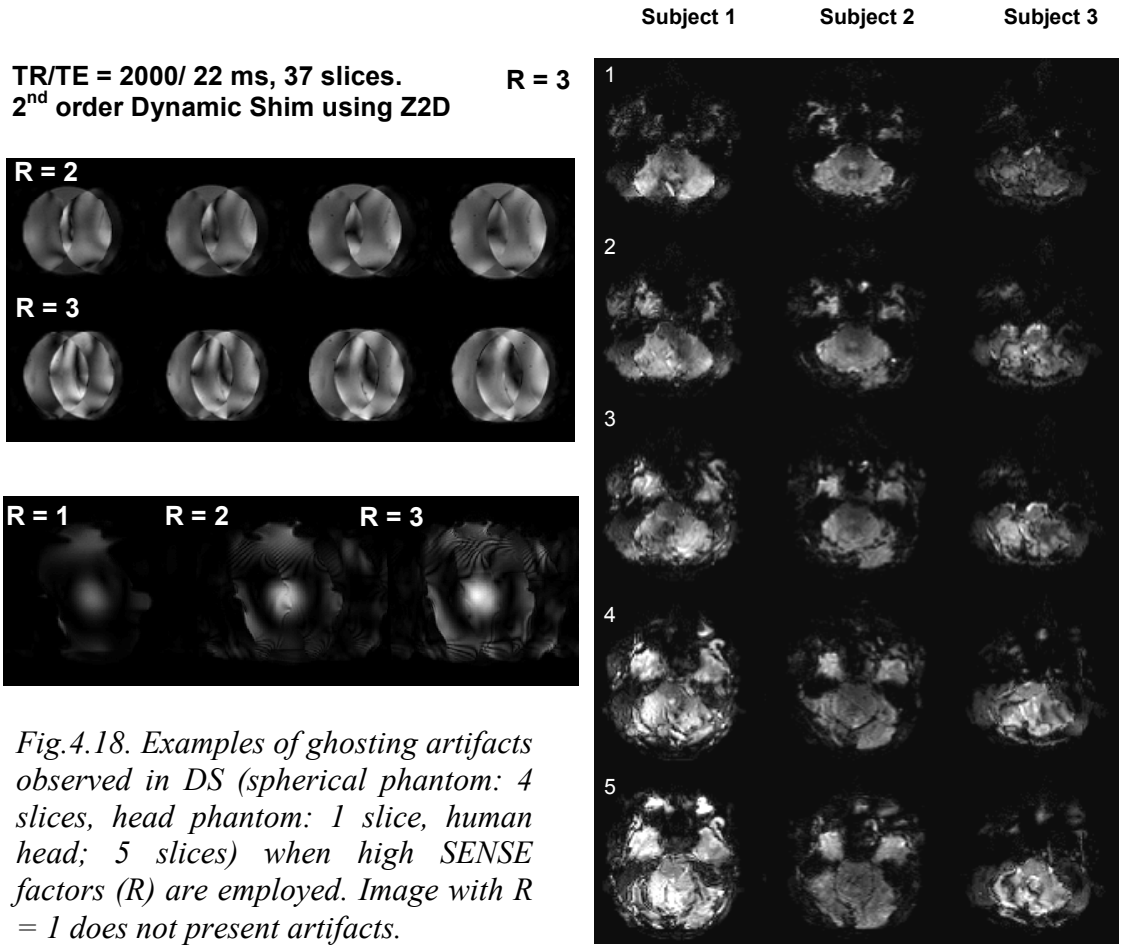

Fig.4.18. Examples of ghosting artifacts observed in DS (spherical phantom: 4 slices, head phantom: 1 slice, human head; 5 slices) when high SENSE factors (R) are employed. Image with R = 1 does not present artifacts.

The spherical phantom and human head images were acquired with a TR/TE = 2000/22 ms, 37 slices. The SENSE acceleration factor was 3 for the human scan while the phantom scan was repeated with R = 2 and 3. A copper sulphate head shaped phantom was also imaged at acceleration factors of R = 1, 2 and 3. These paratmers are typical of whole brain functional MRI studies, which otherwise might benefit greatly from DS. The severe artifacts seen here seriously limit the practical utility of non compensated DS. A closer look at the spatial structure of the artifacts reveals a similarity to SENSE reconstruction artifacts. [Pruessmann 1999, 2001]. The ghosting pattern is seen to increase in complexity with increasing reduction factor closely mirroring the image aliasing patterns in parallel imaging.

The effect of TR on the intensity of the artifacts provides further clues to the underlying reason. Figure 4.19a shows SSEPI images of the head shaped phantom acquired with 2^{nd} order DS at TRs of 3, 4.3, 5.6, 6.8 seconds. The ghosting artifacts decrease with increasing TR, pointing to decaying eddy currents being the source. Figure 4.19b displays the same slice with a static 2^{nd} order global shim and first order dynamic shim (which is compensated for eddy currents) acquired at a TR of 3 seconds. The artifacts are considerably reduced in both cases, further reinforcing the hypothesis that the artifacts are caused by eddy current fields produced by rapidly switching shims.

One of the possible reasons for the enhanced artifacts could be time varying eddy fields of various orders produced by dynamic shim switching leading to off-resonance and erroneous SENSE reconstruction. It has been shown that the SENSE reconstruction is ill conditioned in the presence of B_0 inhomogeneities and in general non cartesian *k* space trajectories (that may be either intentional as in spiral or radial sampling or caused

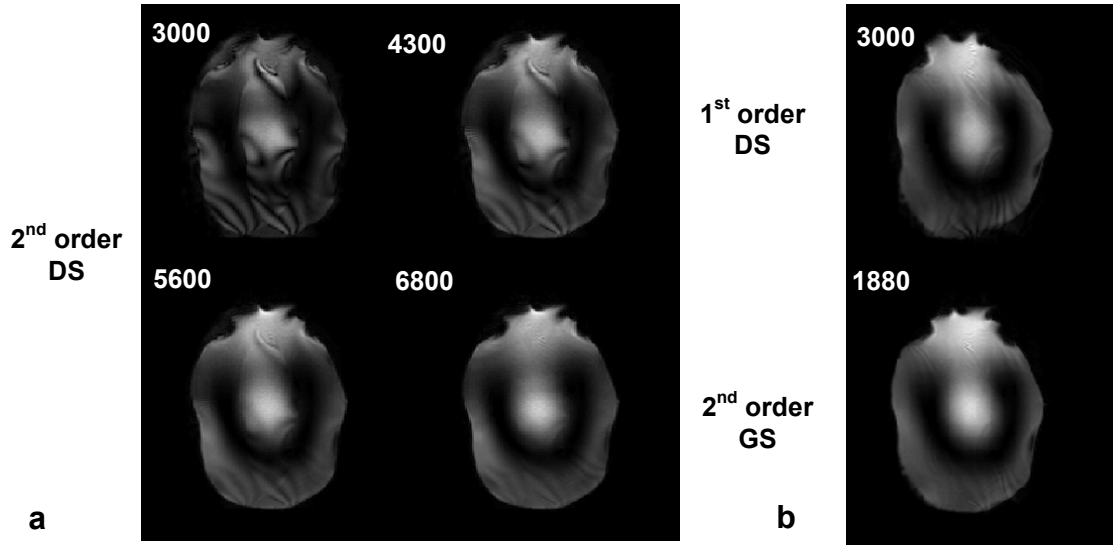

Fig .4.19 (a) Artifacts decrease with increasing TR. Single slice is displayed with TRs in msecs (b) 1st order DS and Static global shimming do not produce artifacts.

by eddy fields), leading to structured noise amplification in the reconstruction [Pruessmann 2001, Sutton 2001]. In general, the interaction of off-resonance with parallel imaging reconstruction has been described previously [Sutton 2001, 2003, Barmet 2005]. One technique that has been proposed in order to deal with B_0 inhomogeneities in SENSE is the iterative conjugate gradient reconstruction (ICGR) method. [Sutton 2003]. This technique models the reconstruction problem as a solution to a general 'system matrix' equation. The system matrix includes in addition to the Fourier encoding terms, the field inhomogeneity, coil sensitivities and in theory any other known signal perturbations. The ICGR method has been shown to correct for ΔB_0 related artifacts in SENSE [Barmet 2004, 2005]. One important caveat however, is that the field inhomogeneity has to be known at the time of image acquisition. In DS, due to rapid switching of shims, eddy current fields are changing continuously. In order to account for these changing fields in the ICGR method, one will have to perform real time mapping of

higher order fields. Continuous field monitoring by multiple NMR probes has been shown to improve iterative image reconstruction. [Pruessmann 2005, Wilm 2009]. We have not conducted in depth modeling and characterization of the above artifacts. In 2nd and 3rd order DS however, these artifacts remain truly debilitating and prevent us from applying uncompensated DS in most real world applications.

Apart from advanced reconstruction techniques like ICGR, there are several approaches that vary in their cost and effectiveness that may be adopted to deal with the above artifacts. The approaches may be broadly classified into hardware and software based methods. The list below gives an overview of the possible solutions

Hardware Based

1. Fully shielded shim coil set: Using a fully shielded shim coil set similar to the gradients can reduce eddy currents substantially. Currently, only the Z2 and Z0 coils are shielded in our scanner. However, this is an expensive and inefficient solution. More practically, improved shielding on only certain coils like the Z2 may provide acceptable performance.
2. Full eddy current compensation on higher order shims: Eddy current compensation on the shim waveform control can also reduce eddy current effects to a high degree. This again is an expensive solution given the number of shim channels present in a typical higher order shim system[1].
3. Spatio-Temporal Field monitoring: It is also possible to monitor and correct for the eddy current fields in real time using an arrangement of NMR probes [DeZanche 2008, Barmet 2008, Wilm 2009] or using separate spherical

[1] We have recently acquired a second generation RTS, the MXV 14/4 from Resonance Research Inc, MA,USA that includes full eddy current compensation for higher order shims.

harmonic inductive detection coils in the bore [Edler 2008]. While still requiring considerable hardware resources, both of these techniques are more economical than the two above methods. However they have not been adequately validated invivo.

Software Based

4. Smarter switching strategies: Better optimized shim switching strategies may be investigated to minimize eddy current effects. These may include switching about a central value so that long time constant eddy currents are cancelled [Wider 1994 , Alexander 1997] , applying shim switches immediately after the data acquisition for the preceding slice, optimizing the slice order for minimizing slice to slice shim switches or other similar techniques. These techniques however in most probability will not be sufficient to fully eliminate the eddy currents.
5. Using combined shims: Using combined shim techniques such as GS2DS1 or GS3DS1 described in section 4.6 that perform better than simple static GS can provide at least partial benefits of DS, without the complicating effects of eddy currents.
6. Using software based eddy current compensation strategy: One can also employ software based eddy current compensation strategies that include correction of eddy current effects by post processing of raw data signal given the prior knowledge of the modified phase and *k*-space trajectories in the presence of eddy fields. [Ordidge 1986, Crozier 1992, Duyn 1998, Ma 2007]. These strategies however suffer from the basic drawback of most post

processing methods, in that signal once lost due to eddy field intravoxel gradients may not be recovered. Furthermore, the eddy current calibration scans do not generally reproduce the effects observed in an actual scan, particularly those of the long time constant fields. We have proposed a novel prospective eddy field compensation method presented in the following chapter that overcomes the above drawback.

In general, all the software based methods are more economical than hardware based methods. However, they suffer from being non-generalizable. In summary, some form of eddy current compensation will be necessary to realize the absolute potential of 2^{nd} and 3^{rd} order DS.

4.8 Discussion

We have implemented higher order dynamic slice-wise B_0 shimming on a 7 Tesla whole body MRI system, by incorporating an external hardware module to store shim values and access the shim supply, in addition to standard communication to the shim unit from the spectrometer. We have also presented a comparison of shimming techniques including hybrid approaches which do not require shim switching hardware, to evaluate the relative benefits of going to higher orders and to DS from GS. Finally we have presented 2^{nd} and 3^{rd} order shim induced eddy current measurements.

Using the RTS module allowed us to access the shim supply and partly circumvent the hardware limitations that make DS difficult. The shim amplifiers nevertheless were relatively low bandwidth with long settling times (+/- 15 ppm of nominal full scale within 2 ms rated) when connected to the inductive shim coil loads in

the magnet. In addition, the current RTS module added 5 - 8 ms of variable DAC update time. As a result, a 10 ms time delay had to be added after each trigger before MR signal excitation, which added considerable time to the GRE scans. This settling time also depended on the magnitude of the shim switch. Therefore, one might be able minimize the time penalty in the GRE DS by extending the delay for the largest shim switches while minimizing the delays for the other switches. Our system did not allow extending the ramp time of the shims which may help to reduce the amplifier settling noise, very short time constant eddy currents and shim acoustic noise. A final goal in this regard would be to minimize DAC update and amplifier settling times and providing fast, flexible control of the shims via the spectrometer and software objects in the pulse programming environment. In general, to minimize amplifier settling and eddy current effects, the shim switch can be made as much before excitation as possible, for instance, just after the acquisition of the preceding slice.

DS showed considerable improvements over static GS, reflected in terms of fieldmap homogeneity, in plane geometric distortion. DS yields the greatest benefits over GS when the imaging volume is relatively large and the inhomogeneity changes substantially over the volume. For smaller volumes with more uniform homogeneity profiles, the improvements obtained by DS over GS are relatively small. We have compared DS to an image based static GS instead of a projection based shimming method, such as FASTMAP. In our experience, projection based methods did not perform well in whole brain studies at 7 Tesla, when the ROI was extended into the frontal and inferior regions of the brain. The reason for this was not investigated, although we suspect that signal voids in these areas of the brain cause errors in estimating

the shims. Also, when calculating shim coefficients, fieldmap thresholding is an often overlooked but critical step, which can otherwise lead to large errors and increased variation in shim values. For example, in the brain fieldmaps, it is essential to exclude the scalp field information. It was also found necessary to constrain the shim calculation to limits based on shim amplifier ratings, especially for the weaker Z2D. Constraining the shim calculation also reduced variations in shim values from slice to slice, leading to smoother shim transitions and reduced eddy current related artifacts.

The benefits in signal recovery by DS as evident from the T_2^* maps were not significant when compared to GS, even though large improvements were predicted in the simulations. DS by optimizing the signal however was seen to improve signal recovery over the degeneracy method. Future studies should be focused on investigating these differences between the predicted and measured signal.

In our measurements, higher order unshielded shims produced strong B_0, self or cross term eddy fields, with multiple decay time constants varying from milliseconds to seconds. Of the 2nd order shims, the Z2 unshielded channel had the strongest eddy currents with the longest time constants as was also observed by Koch *et al*. [Koch 2006]. In the imaging experiments, the tesseral second order shims most often operated with interslice switches of much lesser than 10% of maximum (1 Amp), both on humans and phantoms leading to minimal eddy field effects from those unshielded shims. However the Z2 harmonic was observed to contribute significantly to the field corrections, rendering it indispensable. The presence of the actively shielded Z2 shim coil in our scanner was absolutely critical in limiting the eddy currents and image artifacts in SSEPI. Our results with eddy current measurement and imaging comparing Z2 and Z2D

precluded the use of an unshielded Z2 coil in DS (Figure 4.3). Careful thresholding of the fieldmaps to remove erroneously unwrapped field regions and spike noise pixels before calculating the inplane and the through plane shims, removing scalp and extraneous field information and constraining the shims helped considerably in reducing the slice to slice shim variations. These steps in conjunction with using the Z2D shim coil were critical in allowing SS EPI images without considerable ghosting artifacts with the parameters used. The use of a Z2D coil however came at the cost of reduced shim strength, -0.58 $Hz/cm^2/A$ vs -1.97 $Hz/cm^2/A$ for the unshielded Z2 coil. In future implementations of DS, both the Z2 coils will be used simultaneously. The unshielded coil will provide a constant value to which slicewise Z2D changes will be added, increasing the Z2 dynamic range. It is important to note that using the Z2D coil does not completely eliminate eddy fields from Z2 switching, especially in the B_0 channel as observed in our measurements. Improvements in shim coil shielding techniques and addition of shim eddy current compensation will improve DS in the future. The eddy current values measured here may be used as initial estimates for adjusting a compensation system. The pre-emphasis shim currents will produce their own eddy current fields, which have to be compensated in an iterative manner. Our measurements did not separate any non-eddy current effects that can also result in field changes i.e., current non-constancy effects or vibration induced emfs that are not compensated for by the shim amplifiers [Nixon 2008].

Third order shims, especially Z3, Z2X and Z2Y, were seen to produce very strong first order fields with long time constants in the Z, X and Y directions respectively, when the shims were switched dynamically. The magnitudes of these first order fields decayed with time and scaled with the switch magnitude of the 3^{rd} order shims. These fields were

different from static interactions between the 3rd and 1st order shims, which were, themselves quite large (e.g. -22.57 Hz/cm of X per Hz/cm^3 of Z2X, -7.08 Hz/cm of Y per Hz/cm^3 Z2Y). The absence of an effective compensation system for these first order decaying eddy fields hindered us from implementing 3rd order DS. Compensation of these strong linear eddy fields may not be trivial however, as it might entail interfering with the gradient signal channels.

4.9 Conclusion

Dynamic slice-wise shimming has been implemented on a 7 Tesla high field imaging system and has been shown to produce better field homogeneity compared to static GS method in phantom as well as human whole brain studies. The results demonstrate the feasibility and benefits of DS in high field imaging. Larger benefits were observed in improving inplane distortion than reducing intravoxel signal losses. Future studies should focus on improving signal levels while perhaps compromising to some extent on inplane distortions. The use of a shielded Z2 coil was found to be necessary for obtaining ghosting artifact free images with DS. 2nd and 3rd order unshielded shims were seen to produce long time constant eddy currents of self and lower orders. Finally, a combination of 2nd and 3rd order global and 1st order dynamic shims was also found to improve field homogeneity over 2nd and 3rd order GS, but not over 2nd order DS

Eddy current effects severely limited the application of higher order dynamic shimming in invio studies. Image quality was severely hampered in pulse sequences typically used for whole brain fMRI studies with high SENSE factors. If 2nd and 3rd order DS is to be used in real world applications utilizing low bandwidth sequences, eddy

current compensation will be necessary. Further work is also needed in optimizing shim switching strategies, shim coil shielding, and software control of shims for a more robust implementation of DS to maximize its benefits.

CHAPTER V

SOFTWARE BASED PROSPECTIVE COMPENSATION OF SHIM INDUCED EDDY FIELDS IN STEADY STATE

5.1. Introduction

The performance of DS is severely limited by eddy currents and resulting eddy fields (fields produced by the eddy currents) induced by the switching of 2^{nd} and 3^{rd} order unshielded shims. Eddy currents flow in the conducting structures of the magnet and cause severe field deviations leading to signal losses, distortion and ghosting in imaging [Ahn 1991 1991a, Hughes 1992]. These fields are time varying and decay with multiple time constants. In higher order shims, the time constants range from a few milliseconds to several seconds as observed in our measurements (Table 4.1) and previously reported [De Graaf 2003, Koch 2006]. Traditionally, eddy current effects produced by first order gradient switching have been minimized by actively shielded gradient designs [Mansfield 1986] and residual eddy current effects compensated by using shaped current waveforms in the gradients [Jensen 1987, Glover 1987] as introduced in section 2.7.1. However, the shielding and hardware compensation approaches, when extended to shims, require extensive hardware additions that are typically not available for higher order shims.

In their studies of higher order DS, de Graaf *et al.* in 2003 developed an analog Z2-Z0 compensation unit to correct for the time varying Z0 fields produced by the unshielded Z2 shim coil switching [de Graaf 2003]. Koch et al [Koch 2006] extended this to include all the 2^{nd} order shim eddy currents. However, the inclusion of pre-emphasis on the shims reduced the available shim strengths considerably. In particular the

important Z2 shim was reported to be weakened by up to 75%. Although most 2nd order shims in our whole brain DS experiments were seen to operate at less than 25 % of peak - peak levels, the 3rd order shim demands observed in simulations often exceeded 75% of available range. Therefore, shielding may not be an option for the already weak 3rd order shims and for potential higher order shims. Compensation for all the higher order shims, i.e. 5 second order, 7 third order channels and additional Z0 channels using multiple time constant circuits (Figure 2.11a) will require complex and expensive hardware and calibration. Furthermore, compensation of 1st order eddy fields produced by 3rd order shim switching may potentially involve delicate adjustments to the gradient current drives and existing gradient eddy current compensation (ECC) systems which should be avoided whenever possible for the sake of gradient stability.

Some scanners include certain shims that are actively shielded, most commonly the Z2 shim (as was the case in our 7 Tesla Philips system). Although this helps to mitigate the eddy current problem, actively shielded shims still require compensation for perfect correction (Figure 4.16 c & d). More often than not, only one or two shims have such active shielding. Active shielding of shims also requires additional hardware that includes the outer shield coil that takes up bore space, separate control boards similar to those of the first order gradients, dedicated communication channels and software object controls for precise dynamic operation of the actively shielded coils. Finally, active shielding also reduces the available strength of the shim coil. Overall, hardware based compensation of higher order shim induced eddy currents by either method can prove to be complicated, inefficient and very expensive.

In this chapter, we present a novel method of software based prospective eddy field compensation (EFC) applied to higher order multislice DS. The technique is independent of the object scanned, slice-wise shim amplitude and dynamic shim switching pattern. It does not require the use of extra hardware for ECC or shim shielding. The method is based on an assumption of reaching an eddy field steady state during a DS imaging sequence. This method requires a single one-time calibration scan that characterizes the eddy field behavior of the shim system and derives *correction factors* that are then used to prospectively correct for the eddy fields produced during any DS acquisition.

5.2. Effects of eddy fields from higher order shims

The measurement of eddy currents in our 7 Tesla scanner has been presented previously in section 4.5. These results showed the step response of individual shims, sampled in time. The time constants and amplitudes were measured from the step response by multiexponential fitting. It is interesting however to visualize the effect of the shim switching induced eddy fields in an actual multi-slice DS experiment where the shims are stepped continuously and hence result in the linear convolution of the switching pattern and the step response.

GRE fieldmapping experiments with DS were performed with a copper sulphate human head shaped phantom. In the first experiment, only the Z2X 3^{rd} order shim was switched dynamically for 11 axial slices with shim values of [2.96,2.96,1.48,1.48,0,0, -1.48,-1.48,-2.96,-2.96,0] mT/m^3 . Two other fieldmaps were acquired, one with all slices set to Z2X = 2.96 mT/m^3 and one reference map with all shims set to 0 mT/m^n . In the

second experiment, full 3rd order DS with fieldmapping was performed on 9 slices of the head phantom over a range of TRs, specifically , 168, 600, 1200, 2000 and 3000 ms.

Figure 5.1 shows the fieldmaps acquired from the above experiments. Figure 5.1a shows odd slices from the first experiment, after reference subtraction. In the case where the Z2X shim is kept at a constant value of 2.96 mT/m^3 , the field seen is as expected, showing 3rd order Z2X variation. However in the case where the shim is switched between different values, very strong linear fields in the X (up-down) direction are observed in the slices, which are not explained by the applied Z2X value.

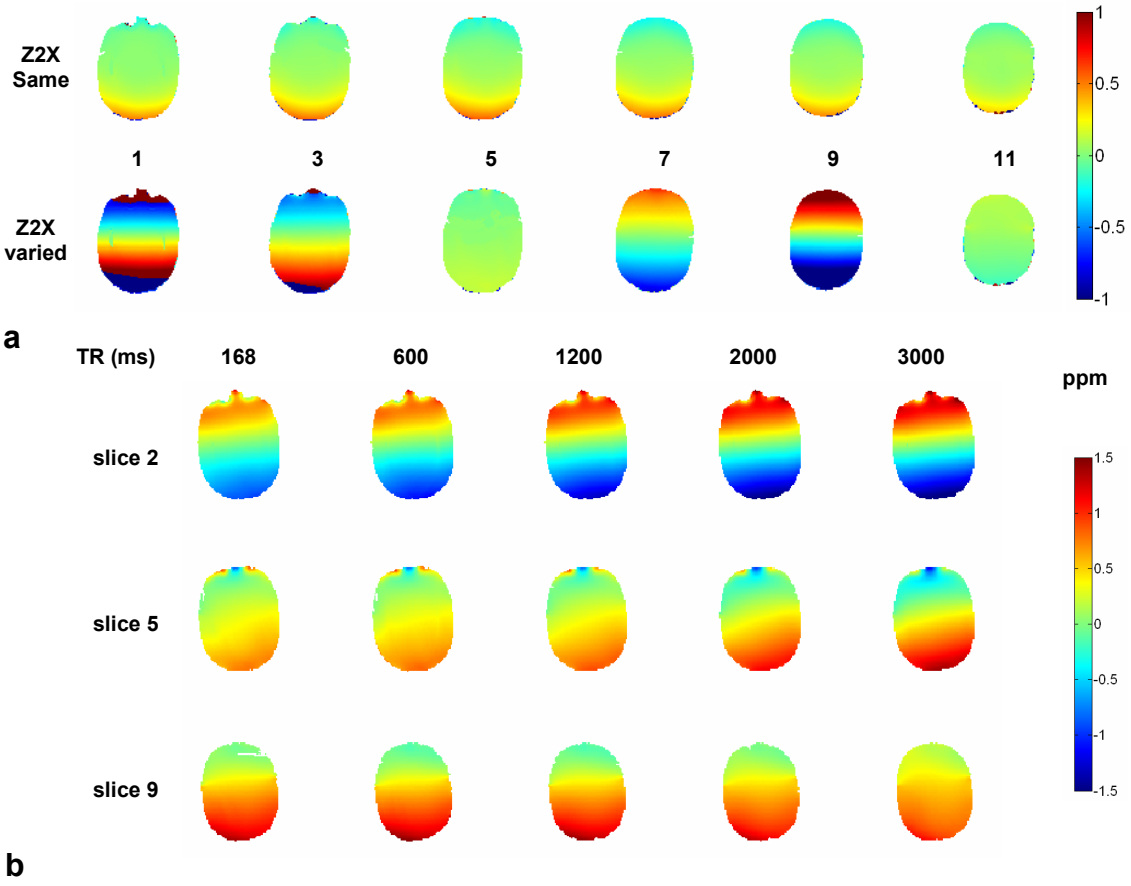

FIG 5.1. Fieldmaps showing fields generated by dynamic switching of shims.(a) Effect of varying vs same Z2X shim values (b) Effect of increasing TR while Z2X switching.

The strengths of these fields are also not explained by the static interaction of Z2X with the X gradient, which is relatively minor (Table 3.1). In addition, the fact that small linear fields are observed in the 5^{th} and 11^{th} slices where the Z2X value was 0, implies that there is a slice to slice interaction in time, pointing to presence of slowly decaying eddy fields.

Figure 5.1b shows the fieldmaps for three slices from the 2^{nd} experiment. One can see strong linear X fields produced by the interaction of Z2X and X through the different TRs. However, the strength of this field is seen to vary for the same slice with TR. This evidence strongly suggests that these interactions are produced by eddy fields that vary in time and therefore depend on the time between the slices, i.e. the time between shim switches. If these interactions were from static cross terms, they would be expected to be fixed with time.

5.3. Theory: Steady state model of dynamic shim induced eddy fields

In our scanner, switching of the 2^{nd} order shims were seen to produce strong self and 0^{th} order eddy fields while switching of the 3^{rd} order shims are seen to produce self, 0^{th} and very strong 1^{st} order fields as shown above and in section 4.5. Other DS studies with 2^{nd} order shim switching have also reported similar interactions [Koch 2006]. Some of the dominating interactions observed in our measurements were the unshielded Z2 shim coupling to Z0, Z2X coupling to X and Z2Y coupling to Y. These fields had large decay time constants of up to a few seconds and superimposed on the existing static field interactions. Dynamic higher order shimming using unshielded shim coils was found to be unfeasible when ECC is not used.

For our method of higher order shim EFC, we make three assumptions. First, we assume that in a multi slice DS GRE experiment, the time varying eddy fields reach a steady state in which the magnitudes of these fields do not change from shot to shot for the same slice. This is a reasonable assumption in a DS multi-slice GRE experiment where the same set of shim values are applied cyclically and switched at a fixed time interval (which is usually the repetition time (TR) / number of slices, irrespective of the actual slice order). Second, we assume that the eddy fields produced depend not only on the most recent switch of higher order shim but also on the previous switches. Third, we ignore any change in eddy field magnitude during the GRE data readout window. Given the high sampling bandwidths in GRE imaging and relatively long time constants of the higher order shim eddy currents, this is reasonable. It follows then, that in an n slice DS experiment we can write:

$$\begin{bmatrix} Ge_1 \\ Ge_2 \\ . \\ . \\ Ge_n \end{bmatrix} = \begin{bmatrix} \Delta G_{1n} & \Delta G_{n,n-1} & \Delta G_{n-1,n-2} & . & \Delta G_{3,2} \\ \Delta G_{2,1} & \Delta G_{1,n} & . & . & \Delta G_{4,3} \\ . & . & . & . & . \\ . & . & . & . & . \\ \Delta G_{n,n-1} & . & . & . & \Delta G_{2,1} \end{bmatrix} \begin{bmatrix} C_1 \\ C_2 \\ . \\ . \\ C_{n-1} \end{bmatrix} \tag{5.1}$$

$$\begin{aligned} & Ge = \Delta G.C \\ or \quad & \& \\ & [(\Delta G^T \Delta G)^{-1} \Delta G^T].Ge = C \end{aligned} \tag{5.2}$$

Here, ***Ge*** is the $n \times 1$ vector of an eddy field harmonic prevalent during individual slice acquisitions. We identified $\boldsymbol{Ge_i}$ as the deviation of a field harmonic magnitude from its ideal value for slice i assumed to be caused by the eddy field. The harmonic represented in ***Ge*** may be the same as the switched shim (self interaction) or different (cross term).

$\boldsymbol{\Delta G}$ is a $n \times n\text{-}1$ matrix of the slice wise shim differences such that $\Delta G_{ij} = G_i - G_j$ where G_i is the shim setting for slice i and $\boldsymbol{C}$ is a $n\text{-}1$ element vector of *correction factors* which gives the *contributions* of the $n\text{-}1$ recent shim switches to the eddy field of any harmonic prevailing during acquisition of any slice. Therefore, in a regular multislice DS GRE experiment where shim values are updated in every slice, C_1 is the contribution of the most recent shim switch to the eddy field in any slice, C_2 is the contribution of the next recent shim switch and so on.

Eddy currents are generated when conducting structures are placed in the vicinity of time varying magnetic fields such as those generated by dynamically switched shims. By Faraday's law, the magnitude of the currents will depend on the rate of change of the magnetic flux and the geometry and impedance of the shim coils and conducting structures. The time constants with which the eddy currents in the conducting structures of the magnet decay depend on the physical properties of the structures, such as their size, impedance and temperature [Ahn 1991]. Therefore, the eddy currents and hence the eddy fields produced in the magnet for any particular shim switching pattern should remain the same regardless of the object imaged. Furthermore, since the correction factor vectors $\boldsymbol{C}$ specify only the relative contributions of the recent shim switches to the eddy field, $\boldsymbol{C}$ is also independent of the actual shim amplitudes.

$\boldsymbol{C}$ may be estimated for the eddy interaction between any pair of shim harmonics by using just a *one time* calibration scan. For example, the time varying Z0 field produced by Z2 shim switching yields a vector for Z2 to Z0 interaction denoted as ***C_Z2_Z0***, which remains invariant with varying shim switching patterns, amplitudes, slice geometry and imaged object, for a fixed time between shim switches (Δt_{ss}) and

number of shim switches. Therefore, for that particular Δt_{ss}, $\boldsymbol{C}$ can be used to calculate the eddy fields expected for the given $\boldsymbol{\Delta G}$ to prospectively compensate for them, assuming that the structures in the magnet in which the eddy currents flow and their relevant properties remain the same. Therefore, a complete one time calibration of all the shim eddy interactions for a particular multislice DS experiment parameterized only by Δt_{ss} yields a set of $\boldsymbol{C}$ vectors which can compensate for all eddy fields without the use of any hardware eddy current compensation. For a standard higher order shim system with 12 higher order shims and 16 channels in all (including X, Y, Z and Z0) for example, the entire matrix of correction factors including self and cross terms would be an *n-1x16x16* array.

The above formulation can be extended to a range of Δt_{ss} and slices to yield $\boldsymbol{C}$ vectors for a complete generalized solution. As Δt_{ss} and the number of slices change for a particular Δt_{ss}, the steady state is set up differently which results in different correction factors.

In the following sections, we present the experiments performed to prove the invariability of $\boldsymbol{C}$ to various experimental parameters including the sample, the actual shim switching pattern and shim values. The $\boldsymbol{C}$ vectors derived from phantom calibration scans were applied in phantom and human DS experiments. Results from 2^{nd} and 3^{rd} order multislice GRE and single shot EPI DS experiments performed on phantom and humans without the use of any hardware based higher order eddy current compensation or shim shielding are presented.

5.4 Generation of steady state

To investigate the formation of eddy field steady state during a DS experiment, a 25 slice, 30 dynamic, single shot EPI scan was performed on a 17 cm diameter spherical doped water "braino" phantom with complete 2nd order DS and with static 2nd order pencil beam projection based shim (PB2). The phase encodes were turned off and raw k space data was acquired. No dummy scans were employed. The first few dynamics images therefore were expected to be acquired under the transient eddy fields, converging to a steady state. Figure 5.2 shows the difference between the first 7 and the 8th dynamic raw phase data for slice 1, for both the shim types.

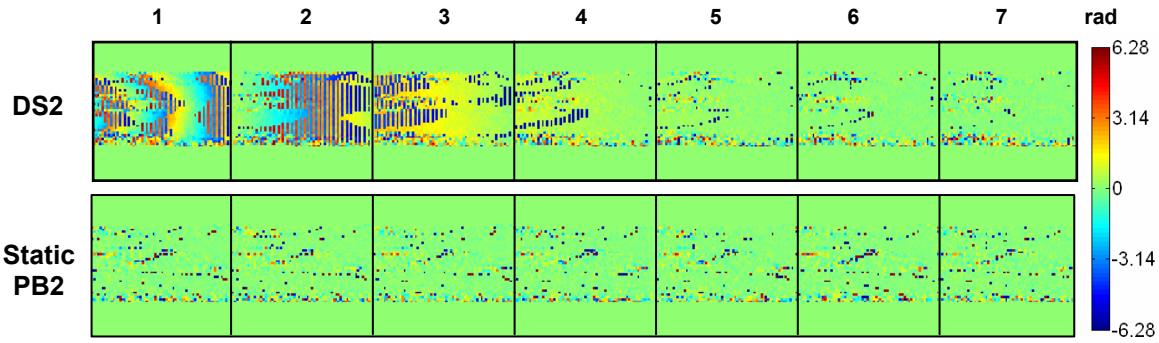

FIG 5.2. Generation of steady state. Raw k space phase difference of dynamics 1-7 from the 8th dynamic of an EPI scan showing steady state generation when using 2nd order DS in comparison to static 2nd order Pencil Beam shim where phase variations between the dynamics are minimal.

In the static shim case, the dynamic to dynamic phase variations are minimal, as expected. However in the DS case, an initial phase transient is clearly seen most likely corresponding to the slowly decaying eddy fields reaching a steady state with continuous shim switching. These results implied that it required about five dynamics in the DS case to develop an eddy field steady state. A more rigorous modeling analysis based on

convolution of the eddy field characteristics may yield a better understanding of the steady state buildup.

5.5 Calibration scans and reproducibility of correction factors

Calibration scans were performed on the shim system to obtain ***C*** vectors for all eddy field interactions at a Δt_{ss} = of 18.7 ms and also to test for invariability of ***C*** with the sample, actual shim values and switching pattern. The scans were performed on different days on two different phantoms, a spherical and a human head shaped phantom. Multislice GRE DS fieldmapping experiments were performed with a ΔTE of 1ms. Individual 2nd and 3rd order shims were switched in different arbitrary patterns for 9 slice (Figure 5.3a, 4 Z2Y shim patterns, 3 in head phantom, 1 in spherical phantom; 1 Z2X pattern, TR/first TE/ΔTE = 168.0/4.4/1.0 ms, slice thickness/gap = 2/2 mm) and 25 slice (Figure 5.3b; 3 unshielded Z2 patterns, spherical phantom, TR/first TE/ΔTE = 467.0/4.4/1.0 ms, slice thickness/gap = 2/2 mm) axial scans. All other shims were set to 0.

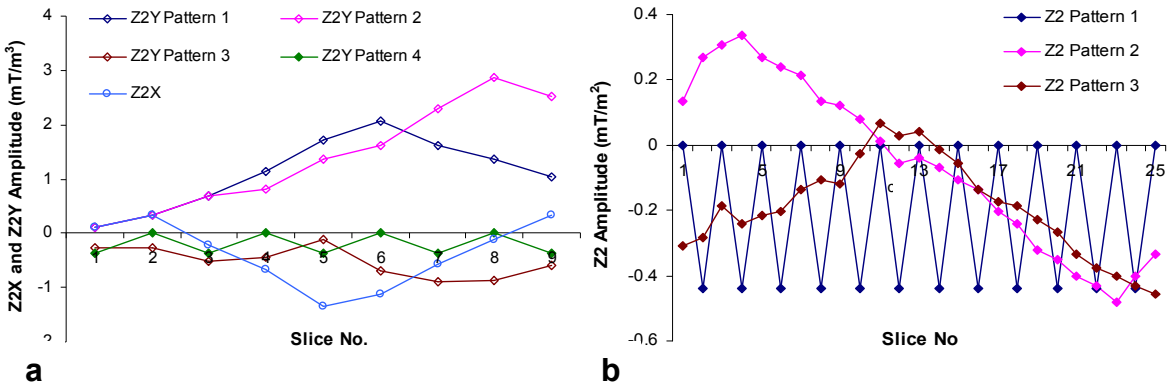

FIG 5.3. Examples of shim switching patterns used in calibration of eddy fields. (a) 9 slice switching patterns of Z2Y (4 patterns) and Z2X shims (1 pattern). (b) 25 slice switching patterns of unshielded Z2 shim. Solid markers indicate spherical phantom, open markers indicate head phantom.

Reference fieldmaps acquired without any shims applied were subtracted from the above fieldmaps. The Z0 offsets expected due to slice position were also subtracted. Shim decomposition up to 3rd order was performed to identify the harmonics that correlated strongly with the switched shim pattern (cutoff $r^2 = 0.9$). The slicewise coefficients of the relevant harmonics were then used as ***Ge*** in Eq.5.2 to calculate 'initial' ***C*** vectors. These 'initial' ***C*** vectors for each particular interaction, for example, ***C_Z2Y_Y,*** i.e. changes in the *Y* shim due to switching of Z2Y, obtained from different calibration scans were averaged and fit to a second order polynomial to yield the final ***C*** vectors.

For calculating the ***C*** vectors for the 'self' shim interactions, i.e. the eddy fields in the shim harmonic that is switched, the 2nd order shims (unshielded Z2, shielded Z2, ZX, ZY, X2Y2 and XY) were switched individually in 25 slice axial GRE spherical phantom fieldmapping scans with the second switching pattern shown in Figure 5.3b (or its inverse). The applied shim values, i.e. the intended ideal fields were subtracted from the actual values obtained for that harmonic from fieldmap shim decomposition. This yielded the field deviations from ideal which we attributed to the eddy current fields as ***Ge***. These slicewise difference fields were then used as ***Ge*** in calculating ***C*** for these interactions. In this manner, the entire *n-1x16x16* correction factor matrix describing the interactions for whole shim system for a particular Δt_{ss} was populated.

Figures 5.4a and 5.4b demonstrate the invariability of the ***C*** vectors with the imaged object and the shim switching pattern for a particular Δt_{ss}. Figure 5.4a shows four Z2Y-Y ***C*** vectors obtained from four different calibration scans with the shim switching patterns given in Figure 5.3a using the spherical and head phantoms, showing high

reproducibility. Figure 5.4b illustrates the Z2_Z0 ***C*** vectors obtained from separate 25 slice calibration scans with different shim switching patterns shown in Figure 5.3b. The ***C***

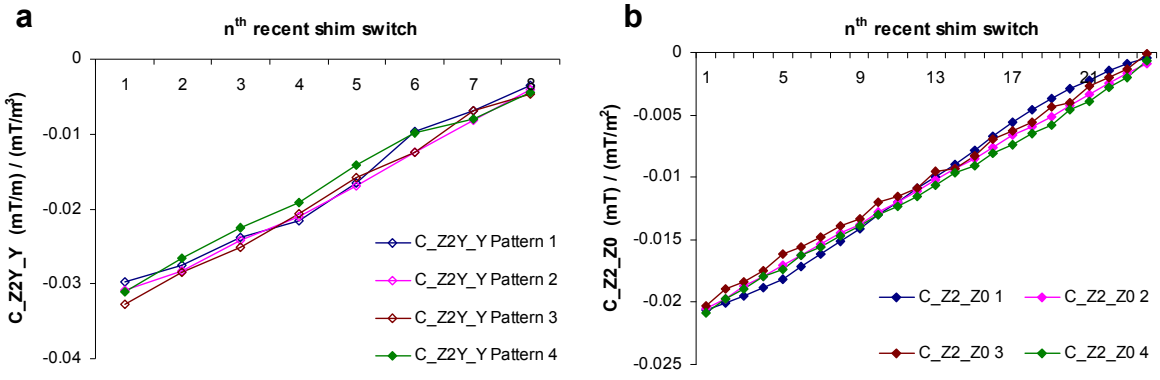

FIG.5.4. Calibration of eddy fields and correction factor reproducibility. (a) 9 slice C_Z2Y_Y vectors obtained from the 4 Z2Y switching patterns shown in Fig 5.3a (b) 25 slice C_Z2_Z0 vectors obtained from switching patterns of unshielded Z2 shim shown in Fig 5.3b. Pattern 2 of Fig 5.3b was repeated on a different day, yielding C_Z2_Z0 vector 4.

vectors show a very high degree of agreement, irrespective of the shim amplitudes, switching patterns, phantom used and day of scanning. The high degree of repeatability in the ***C*** vectors observed here is critical to the successful operation of this method.

*Adjustment of **C** vectors by inclusion of static cross terms*

The phantom calibration scans yielded ***C*** vectors that described the interaction between any pair of shims. However, the ***C*** vectors calculated according to Eq. 5.2 were observed to predict an estimate of ***Ge*** having a constant offset from the actual ***Ge*** for all slices**.** Empirically, this offset was observed to be the *mean value of the switched shim over all the slices multiplied by* the *static interaction factor* between the relevant pair of shims. Therefore, in steady state, the eddy fields were observed to superimpose on this

slicewise static interaction level that was constant for all slices. To account for this offset, an additional unity column was added to $\Delta \boldsymbol{G}$ making it an n x n element matrix, where n is the number of slices and $\boldsymbol{C}$ was changed to an n x 1 element vector with the final element specifying the value of the static cross term. With this adjustment, the calibration process not only accounted for the time varying eddy fields but also the static cross terms between the shims. These modified $\boldsymbol{C}$ vectors hence produced were used in all our experiments for eddy field compensation including the phantom and human scans.

5.6 2nd and 3rd order DS studies with steady state eddy field corrections

The correction factors obtained from the calibration scans were used for prospective correction of the eddy fields in complete 2nd and 3rd order DS experiments in both phantoms and human heads. Both GRE fieldmapping and single shot EPI scans were performed using unshielded shims, with and without the corrections. The following sections present the experiments performed and results obtained.

5.6.1. Phantom experiments: Self shim eddy field correction

To validate the 'self' channel correction, the calibration scan experiment was repeated. However, the 'self' $\boldsymbol{C}$ vectors derived as described before were now used to calculate the field deviations expected due to the self eddy fields using Eq 5.1 based on the $\Delta \boldsymbol{G}$ matrix calculated from the intended shim values. These corrections were used to prospectively adjust the slicewise individual shim value. The shielded Z2 shim was not adjusted as it compensated intrinsically for the self eddy fields produced and hence

served as a reference for comparing the performance of the unshielded Z2 coil with and without correction.

Figure 5.5 (a–d) shows the measured values of the 2nd order tesseral shim harmonics (XY, X2-Y2, ZY and ZX) obtained from the 25 slice spherical phantom scans before and after applying 'self' correction. The prescribed values are also plotted. In the absence of correction, the eddy fields in the self channels prevent the shims from reaching the prescribed level. As a result, incorrect slicewise shim fields are observed. With correction, the fields are adjusted to closely match the slicewise prescribed values. The field errors observed without corrections should not be confused with calibration errors.

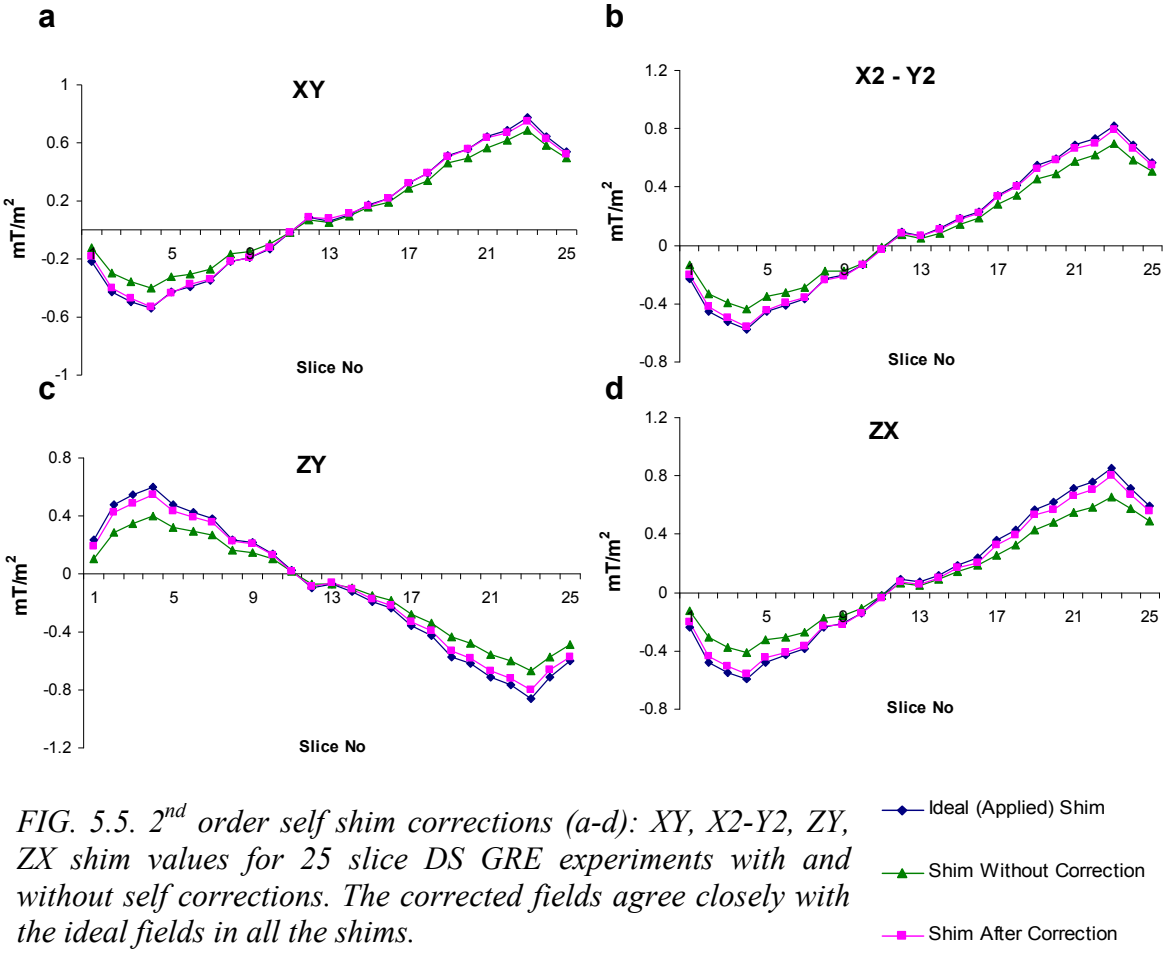

FIG. 5.5. 2nd order self shim corrections (a-d): XY, X2-Y2, ZY, ZX shim values for 25 slice DS GRE experiments with and without self corrections. The corrected fields agree closely with the ideal fields in all the shims.

Figure 5.6 compares the performance of the shielded Z2 coil without correction to the unshielded Z2 coil with correction. The shielded Z2 coil follows the prescribed field closely, as expected. Without correction, the field from the unshielded Z2 coil is severely compromised by the self eddy fields. The initial slices are maximally influenced owing to the largest switch in shim values from the last to the first slice (ascending non interleaved slice order was used). After correction, the slicewise fields agree with the ideal values and the ones produced by the shielded Z2 coil Therefore, the *Z2_Z2 C* vector gives us a entirely software based correction for the self eddy field produced by the unshielded, uncompensated Z2 coil. These results indicate that one may be able to produce unshielded shim coil performance similar to that of a shielded coil very easily by prospectively applying the steady state software based corrections.

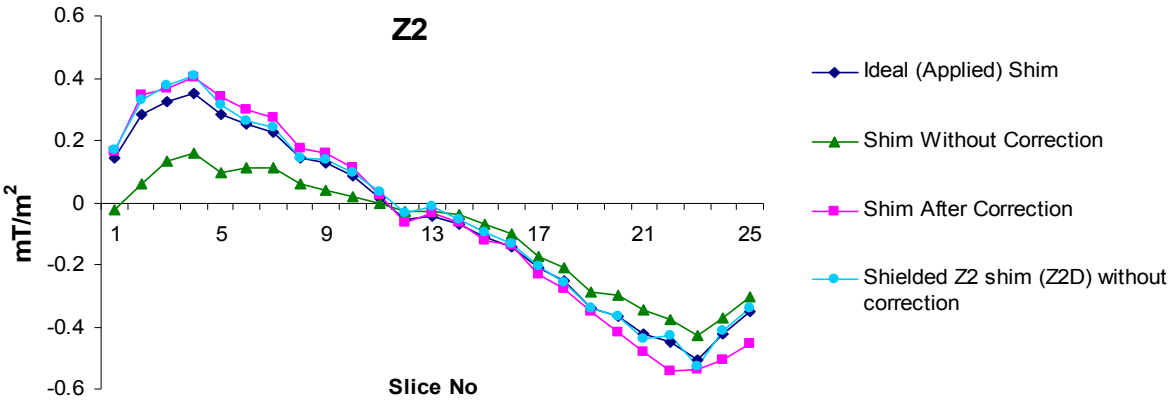

FIG. 5.6. 2nd order self shim correction for the Z2 coils. The unshielded Z2 shim field after correction follows the ideal and the shielded shim field values.

5.6.2. Complete DS GRE Fieldmapping experiments: Phantoms

For validation of the correction technique for complete 2^{nd} and 3^{rd} order DS, 9 slice spherical phantom (64 x 64, TR/first TE/ΔTE = 77.0/4.4/1.0 ms, slice thickness/gap = 2/2 mm) and 25 slice head phantom (64 x 64, TR/first TE/ΔTE = 215.0/4.4/1.0 ms, slice thickness/gap = 2/2 mm) axial fieldmaps were obtained. All shim currents set to 0 mT/m^n. Using a region of interest (ROI) defined by all voxels with nonzero signal in every slice, slice-wise shim values up to 2^{nd} order (for the spherical phantom) and 3^{rd} order (for the head phantom) were calculated. The slicewise shim eddy field corrections for all the shim channels were obtained using the complete correction factor matrix derived from the calibration scans and prospectively added to the shim values. Dynamically shimmed GRE based fieldmaps were then acquired at 128 x 128 pixel resolution with and without the eddy field corrections at a Δt_{ss} of 18.7 ms, which matched the Δt_{ss} of the calibration scans.

Figure 5.7 illustrates the corrections obtained in complete 2^{nd} and 3^{rd} order phantom DS experiments. Figure 5.7a shows 9 axial slice fieldmaps acquired of a spherical phantom using 2^{nd} order DS, with and without eddy field corrections. The fieldmaps without eddy field corrections included conventional static Z2 to Z0 correction of -2.08 $ppm/mT/m^2$ of Z2 for all slices. The fieldmaps without the steady state corrections however show residual field offsets that are different for different slices and are not compensated by just the static correction. These offsets caused by eddy fields from Z2 switching are compensated in the scans with the steady state correction. The steady state correction includes the static interaction correction as well, which is inherently captured in the modified $\boldsymbol{C}$ vector.

Figure 5.7b shows selected slice fieldmaps from a 25 slice head phantom scan using 3rd order DS. In all slices, severe field gradients caused by 3rd to 1st order eddy field interactions are corrected using this method, without any hardware ECC or individual

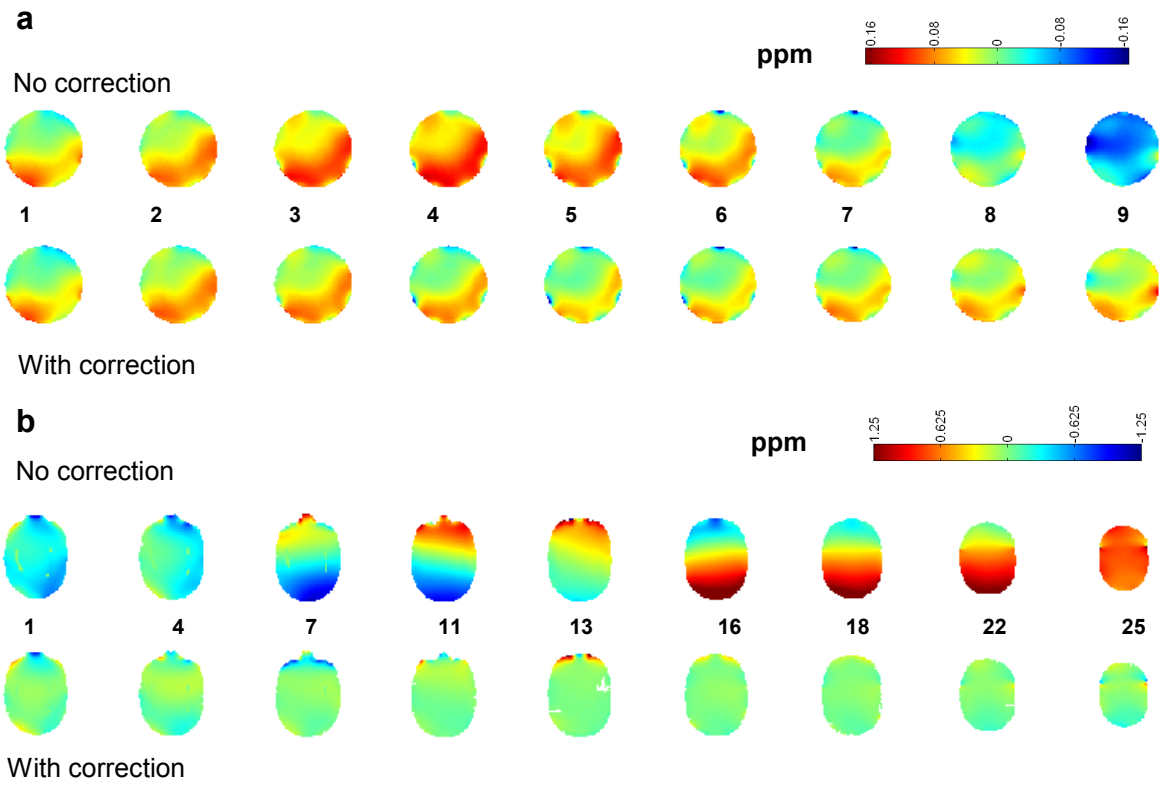

FIG. 5.7. Correction results from 2nd and 3rd order DS phantom experiments. (a): Fieldmaps in ppm from a 2nd order DS scan, without and with Z2 to Z0 eddy field correction. (b) Fieldmaps from 3rd order DS scan, without and with Z2X to X and Z2Y to Y corrections. In all cases severe field offsets and gradients are corrected.

prescanning. The resultant fieldmaps are well shimmed. This indicates that 3rd order DS is possible without using hardware ECC or shielded shim coils.

5.6.3. Complete DS single shot EPI experiments: Phantoms

In order to validate the corrections in low bandwidth imaging, single shot GRE EPI scans were performed on the spherical phantom using the T/R volume coil. 25 axial

slices were acquired with the same scan geometry as the GRE scans, with TR/TE = 1420/23 ms and no SENSE acceleration, giving a Δt_{ss} of 57 ms. The scans were performed with 2nd and 3rd order DS, with and without the steady state field corrections. The scans without the eddy field corrections included the static cross term corrections. 10 dummy scans were used to allow the eddy fields to reach a steady state.

It was necessary to perform an offline reconstruction to eliminate severe FOV/2 ghost artifacts, most likely caused due to short time constant eddy currents distorting k-space sampling. For this purpose, the scanner inbuilt first order phase correction was found to be inadequate in correcting for these artifacts. For this purpose, an established phase correction method using the odd and even echo lines of the phase measurement scan was used [Bruder 1992, Hu 1996]. A phase calibration preparation was run on the scanner prior to the actual EPI scan.[1] The preparation stage consisted of two scans similar to the actual scans, but without any phase encodes blips. The two scans had different TEs, the difference being equal to dwell time in the phase encode direction. Therefore, the even numbered echoes of the first scan occurred at the same time as the odd numbered echoes of the second scan. This ensured that those two echoes experienced the same degree of eddy fields. Care was taken to ensure that the slicewise dynamic shim values were also applied during the echo phase offset determining preparation stage.

Complex raw data was extracted for the actual scan, along with the echo phase calibration data for odd and even lines of k-space. After inverse Fourier transforming the calibration data along the readout direction, phase offsets between pairs of consecutive lines were determined by multiplying the phase from odd calibration lines with the conjugate of the phase from even calibration lines in the k-t space. These alternate line

[1] The Philips scanner runs a phase calibration preparation scan as its default setting for all EPI scans.

phase correction factors hence obtained were then multiplied to the phase of the k-t transformed raw data to yield a phase corrected raw data set. Following this, inverse Fourier transform was performed along the phase encode direction to yield the final corrected image.

Figure 5.8 display the results from the EPI scans. The images without the eddy field corrections show severe distortions, bulk shifts and ghosting. The distortions are primarily in the form of skewing indicating large field gradients along the frequency encode (up-down, or *x*) axis. These effects are almost perfectly corrected by the steady state field corrections.

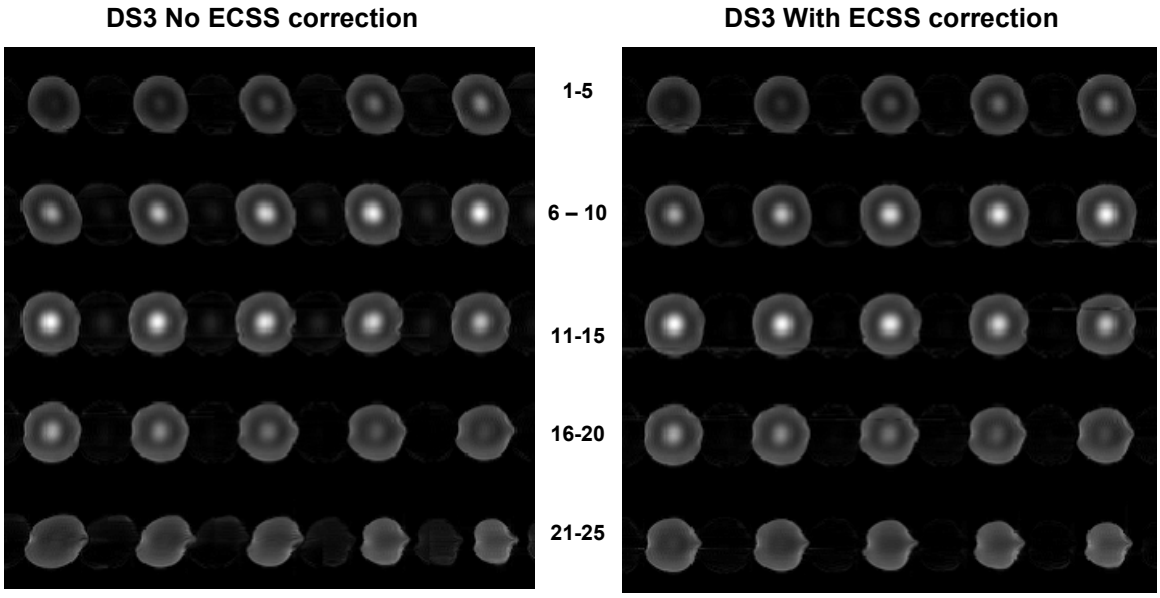

Figure 5.8 25 slice single shot EPI phantom images without and with ECSS correction after N/2 correction for 3rd order DS. Images without correction show severe distortions, bulk shifts and ghosting that are corrected by the method.

5.6.4. Complete DS GRE Fieldmapping experiments: Humans

All human volunteers provided informed written consent and were scanned under an IRB approved protocol. For the human scans, low resolution fieldmaps (n = 4,

64 x 64 pixels, 25 slices, TR/first TE/ΔTE = 196.0/3.9/1.0 ms, slice thickness/gap = 3/1 mm) were obtained with all shims zeroed. The fieldmaps were masked using skull stripping to delineate the shim region. Slice-wise shim coefficients up to 3rd order were calculated. Dynamically shimmed GRE images and fieldmaps (128 x 128 pixels, TR/first TE/ΔTE/Δt_{ss} = 467.0/4.4/1.0/18.7 ms) were acquired with and without the prospective steady sate eddy current corrections. The scans without the eddy field corrections included the static cross term corrections.

The ***C*** matrix used for the eddy field correction in the human DS experiments was derived entirely from calibration scans run on phantoms. No calibration scans were run on human subjects. Also, the slice gaps and thicknesses used in the human scans (3/1 mm) were different from those used in the phantom calibration scans (2/2mm).

Figure 5.9 shows fieldmaps from 25 slice human head 3rd order DS scans with and without corrections. The fieldmaps without corrections show severe offsets and field gradients due to the eddy currents produced by 2nd and 3rd order shim switching. The magnitude of the field is well in excess of 1 ppm at places, and the *x* and *y* field gradients exceed 0.1 mT/m, which can cause significant pixel displacements even at high readout bandwidth GRE imaging (bandwidth 0.032 mT/pixel here). In comparison, the fieldmaps with the correction show well shimmed fields, with excellent homogeneity. These results strongly suggest that the method is applicable under the higher and more arbitrary slicewise shim correction demands usually encountered in the human brain and the ***C*** factors obtained from phantom calibrations are very reliably translatable to human scan.

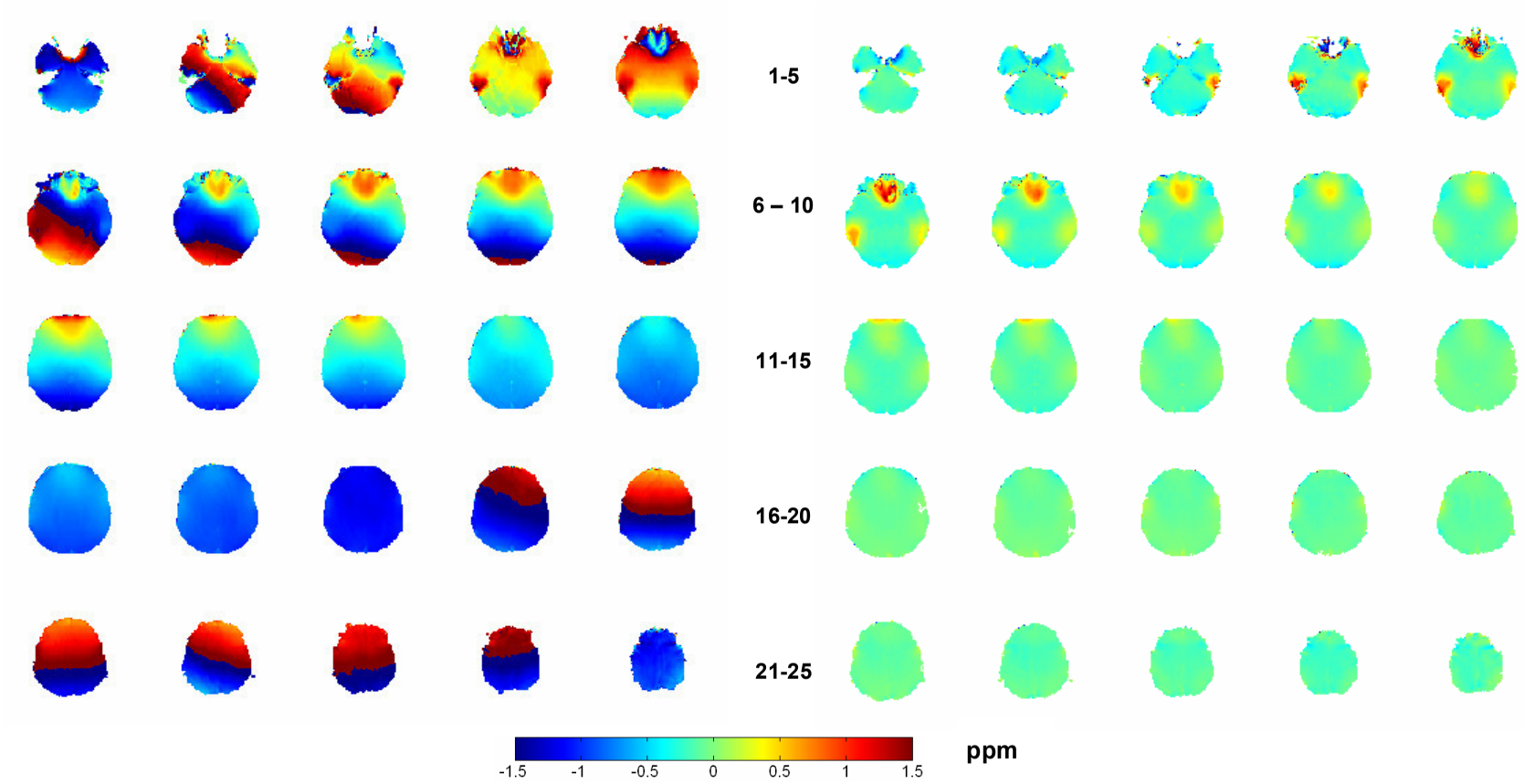

*FIG. 5.9 25 slice fieldmaps showing results from 3rd order DS GRE human experiments without and with steady state eddy field corrections. In all cases severe field offsets and gradients are corrected by the method. Field wraps are observed in the maps without correction, indicating field offsets greater than 1.7 ppm (1.7 ppm = 500 Hz = 1/2 * 1/ ΔTE, ΔTE = 1ms). Slice numbers indicated in between the two sets of fieldmaps.*

5.6.5. Complete DS single shot EPI experiments: Humans

In order to validate the corrections in low bandwidth imaging in humans, single shot GRE EPI scans were performed on an individual subject using the T/R volume coil. 25 axial slices were acquired with the same scan geometry as above, with TR/TE = 2765/27 ms, 128 x 128 pixels, no SENSE acceleration and 10 dummy scans. The Δt_{ss} was 110 ms. The scans were performed with 2^{nd} and 3^{rd} order DS with and without the steady state field corrections. Reconstruction with N/2 ghost correction using raw data was performed in a similar fashion as described previously for the phantoms.

The single shot echo planar images show considerable improvements with steady state field corrections in both 2^{nd} and 3^{rd} order DS. Selected slices after N/2 ghost removal are shown in Figure 5.10. The uncorrected 2^{nd} order DS images show bulk shifts in the phase encode (left-right) direction as a result of 2^{nd} order shim to Z0 eddy field interactions. These shifts are corrected by the field corrections, indicating the compensation of Z0 eddy fields. The 3^{rd} order DS images without correction show very poor quality with large distortions, shifts, signal losses and ghosting. Significant in-plane skewing as well as stretching distortions are observed and indicate large field gradients in the frequency and phase encode directions. These correlate well with the gradients observed in the fieldmaps, as expected. In some slices (for example in slice 1), signal is lost completely. The steady state corrections correct for these effects to a large extent leading to greatly improved image quality.

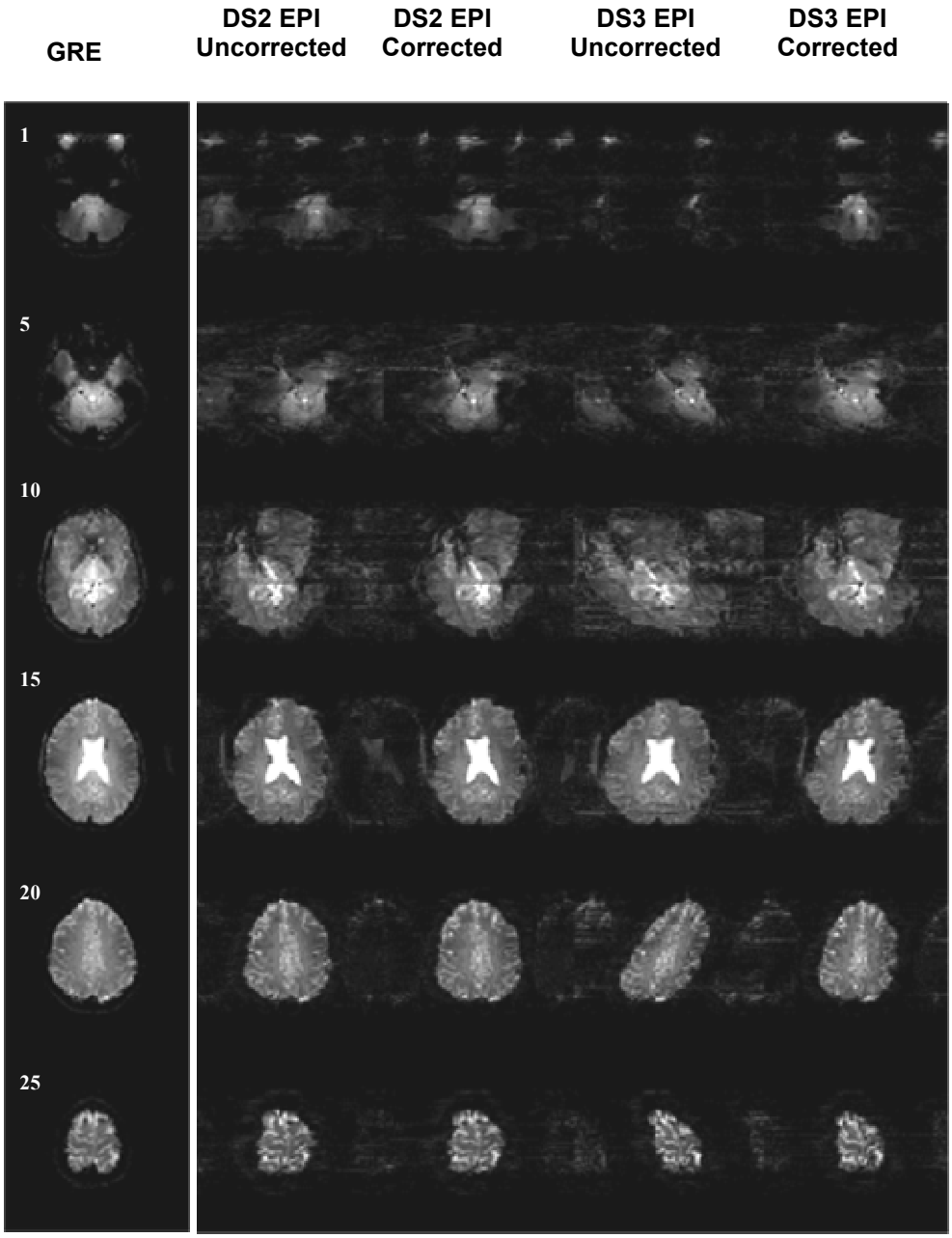

FIG. 5.10. Slices from 2nd and 3rd order dynamically shimmed single shot EPI scans before and after steady state field corrections for the human head. Images shown are post phase correction for odd and even echoes. Uncorrected DS2 images show left - right bulk shifts arising from Z2 to Z0 interactions and ghosting that are corrected by the method. Uncorrected DS3 images show severe distortions, bulk shifts and signal losses due to 3rd order to 1st order interactions, corrected to a large extent by the steady state corrections. High bandwidth gradient echo images and slice numbers are shown in the left panel.

5.7 Generalization of steady state correction

The eddy field correction procedure described here is based on the assumptions of steady state conditions set up by rapid cyclic shim switching. Therefore, the medium and long time constants of the eddy fields, Δt_{ss} and number of slices or shim switches per cycle are parameters that determine the ***C*** vectors. To investigate the variation of the ***C*** vectors with Δt_{ss} and the number of slices, two sets of scans were performed

The first experiment probed the variation of ***C***, specifically ***C_Z2_Z0*** with changing Δt_{ss}. 9 slice axial GRE fieldmaps scans were performed using the spherical phantom with only the unshielded Z2 shim switched in the switching pattern = 0,-0.4,0,-0.4,0,-0.4,0,-0.4,0 mT/m^2 for a range of TRs (TR/Δt_{ss} = 168/19, 250/28, 500/55, 750/83, 1000/111, 2000/222, 5000/555, 10000/1111, 15000/1666, 25000/2778, 40000/4444 ms). The fieldmaps were analyzed as described above and ***C_Z2_Z0*** vectors obtained for each of the Δt_{ss}.

In the second set of scans, only the Z2X shim was switched between 0 and -0.37 mT/m^3 (1Amp) for alternate slices of GRE field mapping scans with the head phantom. The scans were repeated for 5, 8, 9, 11, 15 and 25 slices. The Δt_{ss} was 18.7 ms for all the scans. ***C_Z2X_X*** for all the scans was obtained from the fieldmaps acquired.

The extension of the method to varying Δt_{ss} is important for its general applicability. Figure 5.11a shows the Z2_Z0 correction factors obtained from 9 slice scans with TRs / Δt_{ss} ranging from a minimum allowed of 168/ 19 ms to 40.0/4.4 secs. The ***C*** vectors up to around TR/ Δt_{ss} of 2000/222 ms coincide with each other, with subsequent vectors deviating increasingly from the initial cluster. With increasing TR's above 2000 ms, the correction factor values from all the switches except the most recent

have decreasing absolute values, indicating progressively declining contributions to the eddy fields from these switches. However, for a large range of commonly employed

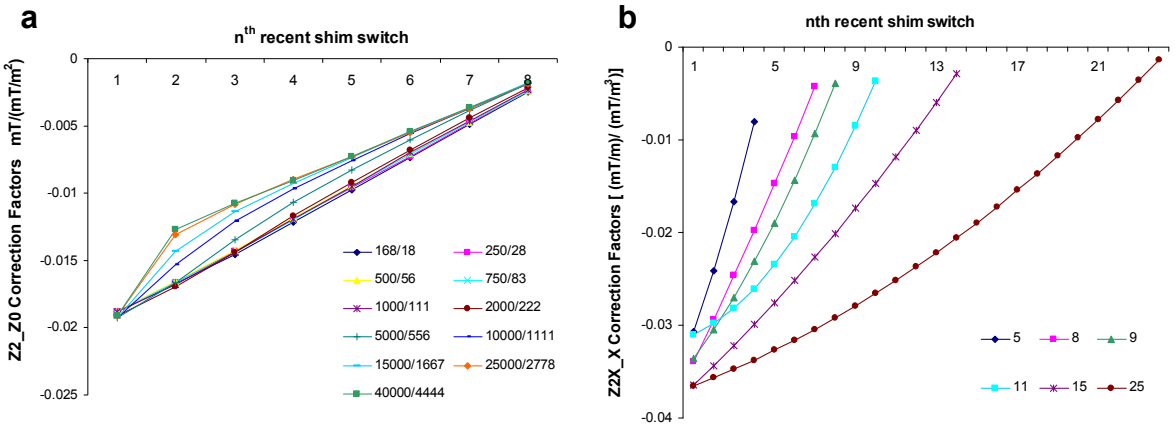

FIG 5.11. (a) Change of C with Δt_{ss}. Z2_Z0. C vectors are shown for 9 slice experiments with varying Δt_{ss}. (b) Change of C with number of slices for same Δt_{ss}. Z2X_X C vectors shown as an example for Δt_{ss} = 18.7 ms.

TRs, the ***C*** vectors do not vary significantly and therefore may be successfully used in a range of experiments.

Figure 5.11b shows the variation of C vectors with number of slices for the same $\Delta t_{ss.}$ The ***C*** vectors change significantly with the number of slices with the n^{th} recent switch accounting for lesser amounts of the eddy fields as the number of slices are reduced. The variation in the ***C*** vectors reflects the effect of the shim switching cycle period on the steady state field developed.

5.8. Discussion

A promising new method for software based prospective compensation of eddy fields produced by shim switching in DS experiments has been described and

demonstrated. The method does not require expensive ECC hardware, shim shielding or individual prescanning and has the potential to greatly reduce eddy current related field perturbations in DS. The method is based on the assumption of reaching an eddy field steady state during a DS experiment.

In addition to not requiring any form of compensation hardware or shim coil shielding, the eddy fields are measured from the actual imaging scan. This is in contrast to traditional eddy field measurement techniques, in which only a step response of the shim is measured. As a result, the convolution effects of rapid repeated shim switching are not captured using the traditional methods. Furthermore, other effects like temporal field fluctuations from pulsed gradient coil vibrations which are usually not compensated can also be potentially accounted for using this method, since they may also be assumed to reach a steady state with shim switching. Also, this method does not reduce the dynamic range of the shims, as is often the case in shim shielding or hardware shim waveform shaping.

The $\boldsymbol{C}$ vectors derived from the calibration scans have been shown to be fixed over a range of imaged objects including the human head, shim switching patterns and actual shim values. The correction factors translate into a characterization of the eddy current behavior of the shims and the magnet structure. The modified n element $\boldsymbol{C}$ vectors inherently account for the dynamic eddy fields as well as the static interactions on which the eddy fields superimpose. The last element of the modified $\boldsymbol{C}$ vector was seen to be equal to the mean value of the switched shim multiplied by the static interaction factor between the two shim harmonics.

The $\boldsymbol{C}$ vectors have been demonstrated to be largely consistent over a range of TRs. The Z2_Z0 interaction considered here as a representative example has highly coincident $\boldsymbol{C}$ vectors up to TRs of at least 2000 ms or Δt_{ss} of 222 ms. As long as the shims are switched in a cyclic manner with a fixed period and Δt_{ss} , we hypothesize the calibration factors will be reproducible irrespective of the sequence type. Results from the EPI scans for example show that even though we introduced the theory in the context of GRE scans, the correction procedure is independent of the sequence and is dependent only on Δt_{ss} and number of slices. Most of the commonly employed GRE and EPI based scans have much smaller Δt_{ss} values and therefore, a single $\boldsymbol{C}$ matrix should be sufficient to compensate for all regular multislice GRE DS scans. This technique should also be applicable to 3D GRE scans, which may of interest in parcellated DS techniques [Poole 2007]. For EPI scans commonly used in functional MRI, certain number of dummy scans over the volume may be employed to reach shim steady state, before actual data acquisition. This is not a hindrance as dummy scans are commonly employed in most dynamic echo planar functional experiments. Further work is however needed to evaluate the robustness of the $\boldsymbol{C}$ vectors with respect to different sequences, especially in long TR scans such as in multislice spectroscopic imaging.

Going further, one may be able to develop a *complete general model* of the $\boldsymbol{C}$ vector that will model the variation of $\boldsymbol{C}$ with respect to the Δt_{ss} and number of slices for a given scanner. Under normal day to day operating conditions, the correction factors are not expected to change significantly. Therefore, information from a single one time phantom calibration scan can be used to develop the general model describing the complete interaction between the shims in the system. Such a calibration scan may be for

example included in a periodic quality assurance procedure to account for long term changes in the magnet's behavior. This general model may then be employed for compensation of eddy fields in any given scan.

This technique may not work in cases where the shims may be switched randomly where steady state is not set up, for instance in compensation of respiration induced field fluctuations. In that particular instance though, only 1^{st} order DS or 1^{st} order DS on top of 2^{nd} order global shims may be sufficient. We have also ignored the short time constant effects of shim switches in our steady state assumptions. The short time constants of the shim eddy currents range from less than a millisecond to a few milliseconds [Koch 2006]. The fields with very short time constants (< 1 ms) may not be included in the steady state and practically may not influence the signal, as usually a delay of ~5 ms is added after shim switching for shim amplifier settling. Alternatively, the ramp times may be extended to reduce the shortest time constant eddy currents. The slightly longer time constant fields would contribute to variations or noise in the $\boldsymbol{C}$ vectors, depending on the actual shim switch value. The effects of these fields on k-space may be calibrated and compensated for in phase measurement preparation stages as was done for the echo planar imaging results presented here. The long time constant eddy fields and their build up however are more difficult to calibrate using preparation phase measurements. The steady state correction method however compensates for these long time constant effects.

5.9. Conclusion

A novel method for software based prospective compensation of eddy fields produced by dynamic shim switching has been described and demonstrated. The method

is based on the assumption of reaching an eddy field steady state generated during a dynamic B_0 shimming experiment. The static and dynamic interactions of the entire shim system are characterized and represented by a single correction factor matrix derived from a one time phantom calibration scan. The method is shown to be independent of the shim switching pattern, imaged object and the actual shim values. The method does not require expensive hardware, shim eddy current compensation or shim shielding thereby providing an economical and efficient alternative. Future work will involve developing a general model of correction factors parameterized in terms of Δt_{ss} and number of slices that will enable software eddy field correction for any multislice DS experiment.

CHAPTER VI

CONCLUSIONS AND FUTURE WORK

The overall purpose of this work was to improve image quality at high field by the utilization of advanced B_0 shimming techniques. Slicewise dynamic B_0 shimming was the primary approach investigated. Specifically, the aims of this work were to 1) Implement slicewise dynamic B_0 shimming on a 7 Tesla ultra high field scanner 2) To evaluate its benefits versus traditional static global shimming and investigate eddy currents produced by higher order shim switching 3) To develop, implement and evaluate a software based prospective based eddy field compensation system.

Dynamic slice-wise shimming was implemented on a 7 Tesla high field imaging system and was shown to produce better field homogeneity, lesser distortion and lesser intravoxel signal losses compared to static GS method in phantom as well as human whole brain studies. Larger benefits were observed in improving inplane distortion than reducing intravoxel signal losses. The results demonstrated the feasibility and benefits of DS in high field imaging. Eddy currents produced by switching of order higher order unshielded shims were also characterized. 2^{nd} and 3^{rd} shims were observed to induce high amplitude rapidly decaying as well as lesser amplitude long time constant eddy currents of self and lower orders. The time constants and amplitudes extracted herein provide a starting point for hardware eddy current circuit setting in the future. The incremental benefits of higher shim orders with both static global and dynamic shimming have also been compared. 2^{nd} order DS was found to yield the minimum residual

inhomogeneity of all the shim orders evaluated, including 3rd order global static shim. These results indicate that it might be more beneficial to include dynamic 2nd order switching capability in a shim system than to include 3rd order static shim coils. Furthermore, combinations of 2nd and 3rd order global and 1st order dynamic shims were found to improve field homogeneity over pure 2nd and 3rd order GS. These combined shim approaches may provide viable image quality improvement alternatives to establishments that do not posses resources to add real time shim switching hardware to their existing systems. An easy to use shimming tool GUI has also been developed and deployed on the scanner to enable other users to include these advanced shimming options in their studies.

The use of a shielded Z2 coil was found to be critical for obtaining ghost artifact free echo planar images with DS. However, as the SENSE factor and shim switching demands were increased, ghosting artifacts increased significantly to the point of rendering the images unusable. Based on empirical evidence, we hypothesize that the artifacts are caused by the interaction of eddy current fields and SENSE reconstruction. These artifacts remain the bottleneck for seamless application of 2nd and 3rd order DS. Of the potential methods to minimize these artifacts, hardware eddy current compensation, although expensive, may be the most generally applicable.

In view of the challenges posed by eddy currents, we have proposed a novel economical software based prospective shim eddy field compensation system. The feasibility of this method has been demonstrated in phantom and human scans. The method can potentially be utilized for correcting the above mentioned artifacts. Further work needs to be done to establish the general applicability of this method.

Ideally, a DS system would be akin to a typical gradient system. It would include fully shielded and eddy current compensated shim coils and would be driven by high bandwidth amplifiers to minimize amplifier ripple. In addition, it would include mechanisms for fast, precise and random shim switching that are controlled by the spectrometer based on the sequence demands. Finally, full dynamic software control would be needed for each individual shim channel for precise waveform (strength, duration, ramp etc) and switching control.

The following list proposes areas of future work that may be carried out to maximize the benefits of DS and to answer unresolved questions that have presented themselves during the course of this work

1. *Improve Signal recovery by use of DS* : The results of T_2^* mapping with dynamic and global shimming are inconsistent with simulated results. Future work will have to address this difference.

2. *Hardware eddy current compensation of higher order shims*: To minimize the eddy currents produced by shim switching and related artifacts, hardware eddy current compensation by shim waveform shaping will be necessary. This work will involve calibration of shim – Z0 cross and self shim channels to cancel out short medium and long time constant fluctuations.

3. *Variety of application studies on the 7T and 3T*: Shimming, being a fundamental component of NMR, a perfectly eddy current compensated DS system will enable

a host of application studies where the benefits of DS over GS can be realized. The benefits will be maximized when extended volumes are investigated. We have demonstrated this in the case of resting state connectivity. Other studies may include whole brain fMRI and DTI, whole body imaging, leg muscle DTI, spine imaging etc.

4. *Compensation of respiration induced field inhomogeneities by DS*: Compensation of respiration induced field fluctuations in the brain with DS has been demonstrated earlier [Van Gelderen 2007]. A combination of slicewise and respiratory field fluctuation driven DS may provide further benefits.

5. *Investigation of SENSE and eddy current interaction:* The effects of inhomogeneity and eddy currents on SENSE reconstruction have been reported previously [Sutton 2003, Barmet 2005]. It may be of interest to replicate in simulations the artifacts encountered in this work, thereby providing a deeper understanding of the above mentioned interaction.

6. *Extension of ECSS to include multichannel data and robust general model. :* The ECSS method introduced in chapter 5 may be extended to include multichannel data in echo planar scans. As a prospective correction method, this may potentially be effective in correcting the eddy current related artifacts. Further work may also

involve developing a robust general model of the correction factors for universal applicability.

7. *Integration of improved B_0 shimming in B_1 profile correction*. : Improved B_0 shimming can prove to be instrumental in improving correction of inhomogeneous B_1 profiles encountered at high field. Integration of DS with B_1 shimming methods would yield more complete solution for the inhomogeneity effects at high field.
8. *Optimization of FASTMAP shim at 7T:* In our experience, FASTMAP based higher order shimming methods have been unreliable in high field experiments. Given the time penalties associated with fieldmap based shimming a more robust projection based shimming method would greatly benefit the imaging community.

To summarize, the work presented in this thesis contributes towards tackling a major technical challenge in high field imaging, namely B_0 inhomogeneity. DS has been shown to be a potentially valuable tool to improve field homogeneity at 7 Tesla. Further work will be required to perfect the methods presented and answer new questions that present themselves as we continue to push the boundaries of high field imaging.

Reference

[Ahn 1991] Ahn CB, Cho ZH. Analysis of the eddy-current induced artifacts and the temporal compensation in nuclear magnetic resonance imagin.g IEEE Trans Med Imag, 1991; 10, 47-52.

[Ahn 1991a] Ahn CB, Cho ZH. Analysis of Eddy Currents in Nuclear Magnetic Resonance Imaging Magn Reson Med 1991; 17, 149- 163.

[Alexander 1997] Alexander AL, Tsuruda JS, Parker DL. Elimination of Eddy Current Artifacts in Diffusion-Weighted Echo-Planar Images: The use of Bipolar Gradients. Magn Reson Med. 1997 38:1016-1021.

[Anderson 1961] Anderson WA. Electrical Current Shims for Correcting Magnetic Fields. Rev. Sci. Instrum 1961; 32(3): 241.

[Barmet 2004] Barmet C, Tsao J, Pruessmann KP. Efficient iterative reconstruction for MRI in strongly inhomogeneous B_0. Proceedings of the International Society for Magnetic Resonance in Medicine 2004, 347.

[Barmet 2005] Barmet C, Tsao J, Pruessmann KP. Sensitivity encoding and B_0 inhomogeneity - A simultaneous reconstruction approach. Proceedings of the International Society for Magnetic Resonance in Medicine 2005; 682.

[Barmet 2008] Barmet C, De Zanche N, Pruessmann KP. Spatiotemporal magnetic field monitoring for MR. Magn Reson Med. 2008; 60(1):187-97.

[Bhagwandien 1994] Bhagwandien R, Moerland MA, Bakker CJ, Beersma R, Lagendijk JJ. Numerical analysis of the magnetic field for arbitrary magnetic susceptibility distributions in 3D. Magn Reson Imaging. 1994; 12(1):101-7.

[Blamire 1996] Blamire AM, Rothman DL, Nixon T. Dynamic shim updating: a new approach towards optimized whole brain shimming. Magn Reson Med. 1996; 36(1):159-65.

[Boesch 1991] Boesch C, Gruetter R, Martin E. Temporal and spatial analysis of fields generated by eddy currents in superconducting magnets: optimization of corrections and quantitative characterization of magnet/gradient systems. Magn Reson Med. 1991; 20(2):268-84.

[Bottomley 1984] Bottomley PA. Selective volume method for performing localized NMR spectroscopy. US Patent 1984.

[Bowtell 1991] Bowtell R, Mansfield P.Gradient coil design using active magnetic screening. Magn Reson Med. 1991;17(1):15-9; discussion 19-21.

[Chmurny 1990] Chmurny, G.N.; Hoult, D.I. The Ancient and Honourable Art of Shimming. Concepts in Magnetic Resonance 1990; 2: 131-149.

[Cho 1988] Cho ZH, Kim DJ, Kim YK. Total inhomogeneity correction including chemical shifts and susceptibility by view angle tilting. Med Phys. 1988; 15(1):7-11.

[Clare 2006] Clare S, Evans J, Jezzard P. Requirements for room temperature shimming of the human brain. Magn Reson Med. 2006; 55(1):210-214.

[Crozier 1992] Crozier S, Eccles CD, Beckey FA, Field J, Doddrell DM. Correction of eddy-current-induced bo shifts by receiver reference-phase modulation, J Magn Reson 1992; 97, 661-665.

[Cusack 2005] Cusack R, Russell B, Cox SM, De Panfilis C, Schwarzbauer C, Ansorge R. An evaluation of the use of passive shimming to improve frontal sensitivity in fMRI. Neuroimage. 2005;24(1):82-91.

[Dahnke 2005] Dahnke H, Schaeffter T. Limits of Detection of SPIO at 3.0 T Using *T*2* Relaxometry Magn Reson Med. 2005;53: 1202–1206

[de Graaf 2003] de Graaf RA, Brown PB, McIntyre S, Rothman DL, Nixon TW. Dynamic shim updating (DSU) for multislice signal acquisition. Magn Reson Med. 2003 ;49(3):409-16.

[DeZanche 2008] De Zanche N, Barmet C, Nordmeyer-Massner JA, Pruessmann KP. NMR Probes for Measuring Magnetic Fields and Field Dynamics in MR Systems. Magn Reson Med. 2008; 60:176–186.

[Duyn 1998] Duyn JH, Yang Y, Frank JA, van der Veen JW. Simple correction method for k-space trajectory deviations in MRI .J Magn Reson. 1998;132(1):150-3.

[Edler 2008] Edler K, Hoult D. Spherical Harmonic Inductive Detection Coils for Dynamic Pre-emphasis Magn Reson Med. 2008; 60:277–287

[Forbes 2001] Forbes LK, Crozier S. A novel target-field method for finite-length magnetic resonance shim coils: Part 1: Zonal shims. J. Phys. D: Appl. Phys. 2001; 34:3447-3455.

[Forbes 2002] Forbes LK, Crozier S. A novel target-field method for finite-length magnetic resonance shim coils: Part 2: Tesseral shims. J. Phys. D: Appl. Phys. 2002; 35:839-849.

[Forbes 2003] Forbes LK, Crozier S. A novel target-field method for magnetic resonance shim coils: Part 3: Shielded zonal and tesseral coils. J. Phys. D: Appl. Phys. 2003; 36:68-80.

[Frahm 1985] Frahm J, Merboldt KD, Hänicke W, Haase A. Stimulated Echo Imaging J. Magn. Reson 1985; 64: 81–93.

[Frahm 1987] Frahm J, Merboldt KD, Hänicke W. Localized Proton Spectroscopy Using Stimulated Echoes J. Magn. Reson 1987; 72, 502-508.

[Glover 1987] Glover et al. Method for magnetic field gradient eddy current compensation. US Patent # 4698591Oct 1987.

[Glover 1991] Glover GH, Schneider E. Three-point Dixon technique for true water/fat decomposition with B0 inhomogeneity correction. Magn Reson Med. 1991;18(2):371-83.

[Golay 1958] Golay MJE. Field homogenizing coils for nuclear spin resonance instrumentation. Rev. Sci. Instr 1958; 29: 313–315

[Golay 1971] Golay MJE. Nuclear magnetic resonance apparatus. US Patent # 3569823 Mar 1971.

[Gruetter 1992] Gruetter R, Boesch C. Fast, Non-iterative Shimming on Spatially Localized Signals: In Vivo Analysis of the Magnetic Field along Axes. J Magn Reson 1992; 96:323-334.

[Gruetter 1993] Gruetter R. Automatic, localized in vivo adjustment of all first- and second-order shim coils. Magn Reson Med 1993; 29:804-811.

[Gruetter 2000] Gruetter R, Tkác I. Field mapping without reference scan using asymmetric echo-planar techniques. Magn Reson Med 2000; 43(2):319-23.

[Hoult1987] Hoult DI. Shimming on spatially localized signals. J Magn Reson. 1987; 73, 174-177.

[Hoult 2009] Hoult D, Chen CN. Biomedical Magnetic Resonance Technology. ISBN 0852741189 1st Ed Jan 1, 1989 (Taylor & Francis).

[Hsu 2005] Hsu JJ, Glover GH. Mitigation of susceptibility-induced signal loss in neuroimaging using localized shim coils. Magn Reson Med. 2005; 53(2):243-8. Erratum in: Magn Reson Med. 2005; 53(4):992.

[Hu 1995] Hu X, Le TH, Parrish T, Erhard P. Retrospective estimation and correction of physiological fluctuation in functional MRI. Magn Reson Med. 1995;34(2):201-12.

[Hughes 1992] Hughes DG, Robertson S, Allen PS. Intensity artifacts in MRI caused by gradient switching in an animal-size NMR magnet. Magn Reson Med. 1992; 25(1):167-79.

[Jaffer 1996] Jaffer FA, Wen H, Balaban RS, Wolff SD. A Method to improve the B_0 homogeneity of the heart in Vivo. Magn Reson Med. 1996; 36:375-383.

[Jensen 1987] Jensen DJ, Brey WW, Delayre JL, Narayana PA. Reduction of pulsed gradient settling time in the superconducting magnet of a magnetic resonance instrument. Med Phys 1987; 14(5):859-62.

[Juchem 2006] Juchem C, Muller-Bierl B, Schick F, Logothetis NK, Pfueffer J. Combined passive and active shimming for in vivo MR spectroscopy at high magnetic fields. J. Magn. Reson 2006; 183: 278–289.

[Kim 2002] Kim DH, Adalsteinsson E, Glover GH, Spielman DM. Regularized higher-order in vivo shimming. Magn Reson Med. 2002;48(4):715-22.

[Koch 2006] Koch KM, McIntyre S, Nixon TW, Rothman DL, de Graaf RA. Dynamic shim updating on the human brain. J Magn Reson. 2006;180(2):286-96.

[Koch 2006a] Koch KM, Brown PB, Rothman DL, de Graaf RA. Sample-specific diamagnetic and paramagnetic passive shimming. J Magn Reson. 2006;182(1):66-74.

[Koch 2007] Koch KM, Sacolick LI, Nixon TW, McIntyre S, Rothman DL, de Graaf RA.Dynamically shimmed multivoxel 1H magnetic resonance spectroscopy and multislice magnetic resonance spectroscopic imaging of the human brain. Magn Reson Med. 2007; 57(3):587-91.

[Koch 2007a] Koch KM, Brown PB, Rothman DL, de Graaf RA Proceedings of the 15th International Society on Magnetic Resonance Medicine, Berlin Germany 2007; pp. 982.

[Koch 2010] Koch KM, Hargreaves BA, Pauly KB, Chen W, Gold GE, King KF. Magnetic resonance imaging near metal implants. J Magn Reson Imaging. 2010;32(4):773-87.

[Lagarias 1998] Lagarias JC, Reeds JA, Wright MH, Wright PE. Convergence Properties of the Nelder-Mead Simplex Method in Low Dimensions. SIAM Journal of Optimization 1998; 9(1), 112-147.

[Lu 2009] Lu W, Pauly KB, Gold GE, Pauly JM, Hargreaves BA. SEMAC: Slice Encoding for Metal Artifact Correction in MRI. Magn Reson Med. 2009;62(1):66-76.

[Ma 2007] Ma C, Jiang XH. A New Eddy-current Compensation Method in MRI. PIERS Online. 2007; 3 (6), 874 – 878.

[Mansfield 1986] Mansfield P, Chapman B, Active Magnetic Screening of Gradient Coils in NMR Imaging J. Magn. Reson 1986; 66: 573.

[Marques 2005] Marques JP, Bowtell R. Application of a Fourier-based method for rapid calculation of field inhomogeneity due to spatial variation of magnetic susceptibility. Concepts in Magn Reso Part B: Magnetic Resonance Engineering Volume 2005; 25B (1): 65–78.

[Maudsley 1979] Maudsley AA, Oppelt A, Ganssen A Rapid measurement of magnetic field distributions using nuclear magnetic resonance Siemens Forch. Entwick1.-Ber 1978; 326-331.

[Maudsley 1984] Maudsley AA, Simon HE, Hilal SK Magnetic field measurement by NMR imaging. J. Phys E: Sci. Instrum 1984; 17: 216-20,

[Morich 1988] Morich MA, Lampman DA, Dannels WR, Goldie FD. Exact temporal eddy current compensation in magnetic resonance imaging systems. IEEE Trans Med Imaging. 1988;7(3):247-54.

[Morrell 1997] Morrell G, Spielman D. Dynamic shimming for multi-slice magnetic resonance imaging. Magn Reson Med. 1997;38(3):477-83.

[Nixon 2008] Nixon TW, McIntyre S, Rothman DL , de Graaf RA, Compensation of gradient-induced magnetic field perturbations J Magn Reson 2008; 1922, 209-217.

[Ordidge 1986] Ordidge J, Cresshull ID. The correction of transient B0 field shifts following the application of pulsed gradients by phase correction in the time domain. J of Magn Reson 1986; 69(1): 151-155.

[Poncelet 1992] Poncelet BP, Wedeen VJ, Weisskoff RM, Cohen MS. Brain parenchyma motion: measurement with cine echo-planar MR imaging. Radiology. 1992; 185(3):645-51.

[Poole 2008] Poole M, Bowtell R. Volume parcellation for improved dynamic shimming. MAGMA. 2008; 21(1-2):31-40. Epub 2008 Jan 8.

[Poole 2008a] Poole M, Green D, Bowtell R. Shoulder-Slotted Insertable Gradient and Shim Coil Set. Proceedings of the International Society for Magnetic Resonance in Medicine 2008; 16: 1165.

[Prammer 1988] Prammer MG, Haselgrove JC, Shinnar M, Leigh JS A new approach to automatic shimming J of Magn Reson 1988; 77(1): 40-52

[Pruessmann 1999] Pruessmann KP, Weiger M, Scheidegger MB, Boesiger P. SENSE: sensitivity encoding for fast MRI.Magn Reson Med. 1999; 42(5):952-62.

[Pruessmann 2001] Pruessmann KP, Weiger M, Börnert P, Boesiger P. Advances in sensitivity encoding with arbitrary k-space trajectories. Magn Reson Med. 2001;46(4):638-51.

[Puessmann 2005] Barmet C, Tsao J, Pruessmann KP. Magnetic field monitoring during MRI acquisition improves Image reconstruction. Proceedings of the International Society for Magnetic Resonance in Medicine 2005; 681

[Raj 2000] Raj D, Paley DP, Anderson AW, Kennan RP, Gore JC. A model for susceptibility artefacts from respiration in functional echo-planar magnetic resonance imaging. Phys Med Biol. 2000;45(12):3809-20.

[Raj 2001] Raj D, Anderson AW, Gore JC. Respiratory effects in human functional magnetic resonance imaging due to bulk susceptibility changes Phys Med Biol. 2001;46:3331-3340.

[Reese 1995] Reese TG, Davis TL, Weisskoff RM. Automated shimming at 1.5 T using echo-planar image frequency maps. J Magn Reson Imaging. 1995; 5(6):739-45.

[Reber 1998] Reber PJ, Wong EC, Buxton RB, Frank LR. Correction of off resonance-related distortion in echo-planar imaging using EPI-based field maps. Magn Reson Med. 1998;39(2):328-30.

[Robertson 1992] S. Robertson, D. G. Hughes, Q. Liu, P. S. Allen Analysis of the temporal and spatial dependence of the Eddy current fields in a 40-cm bore magnet Magn Reson Med 1992; 25(1):158–166.

[Rohde 2003] Rohde GK, Aldroubi A, Dawant BM.. The adaptive bases algorithm for intensity-based nonrigid image registration. IEEE Trans Med Imaging. 2003; 22(11):1470-9.

[Romeo 1984] Roméo F, Hoult DI. Magnet field profiling: analysis and correcting coil design Magn Reson Med. 1984; 1(1):44-65.

[Schneider 1991] Schneider E, Glover G. Rapid in vivo proton shimming. Magn Reson Med. 1991; 18(2):335-47.

[Sekihara 1985] Sekihara K, Matsui S, Kohno H, A new method of measuring static field distribution using modified Fourier NMR imaging. Journal of Physics E: Scientific Instrument 1985; 18: 224-227.

[Shen 1997] Shen J, Rycyna RE, Rothman DL. Improvements on an in vivo automatic shimming method [FASTERMAP]. Magn Reson Med. 1997;38(5):834-839.

[Shen 1999] Shen J, Rothman DL, Hetherington HP, Pan JW. Linear projection method for automatic slice shimming. Magn Reson Med. 1999;42(6):1082-8.

[Shen 2001] Shen J.Effect of degenerate spherical harmonics and a method for automatic shimming of oblique slices. NMR Biomed. 2001; 14(3):177-83.

[Smith 2002] Smith SM. Fast robust automated brain extraction. Human Brain Mapping, 2002; 17:143-155.

[Sutton 2001] Sutton B, Fessler JA, Noll D. Iterative MR Image reconstruction using sensitivity and inhomogeneity field maps. Proceedings of the 9th International Society on Magnetic Resonance Medicine, Glasgow, Scotland 2001; pp. 771

[Sutton 2003] Sutton BP, Noll DC, Fessler JA. Fast, iterative image reconstruction for MRI in the presence of field inhomogeneities. IEEE Trans Med Imaging. 2003; 22(2):178-88.

[Terpstra 1998] Terpstra M, Andersen PM, Gruetter R. Localized eddy current compensation using quantitative field mapping. J Magn Reson. 1998;131(1):139-43.

[Truong 2002] Truong TK, Clymer BD, Chakeres DW, Schmalbrock P.Three-dimensional numerical simulations of susceptibility-induced magnetic field inhomogeneities in the human head. Magn Reson Imaging. 2002 ;20(10):759-70.

[Turner 1986] Turner R. A target field approach to optimal coil design J. Phys. D 1986; 19: 1116–1123

[Turner 1986a] Turner R. Bowley R.M. Passive screening of switched magnetic field gradients Journal of Physics E: Scientific Instruments 1986; 19(10) :876-879.

[Van de Moortle 2002] Van de Moortele PF, Pfeuffer J, Glover GH, Ugurbil K, Hu X. Respiration-induced B0 fluctuations and their spatial distribution in the human brain at 7 Tesla. Magn Reson Med. 2002;47(5):888-95.

[Van Gelderen 2007] Van Gelderen P, de Zwart JA, Starewicz P, Hinks RS, Duyn JH, Real-time shimming to compensate for respiration-induced B0 fluctuations. Magn Reson Med. 2007; 57, 362-368.

[Webb 1991] Webb P, Macovski A. Rapid, fully automatic, arbitrary-volume in vivo shimming. Magn Reson Med. 1991;20(1):113-22.

[Wen 1995] Wen H, Jaffer FA. An in vivo automated shimming method taking into account shim current constraints. Magn Reson Med. 1995;34(6):898-904.

[Wider 1994] Wider G, Dotsch V, Wutrich K. Self-compensating pulse magnetic field gradients for short recovery times J Magn Reson. 1994 Series A, 108 255 - 258

[Wilm 2009] Wilm BJ, Barmet C, Pavan M, Boesiger P, Pruessmann KP. Integration of higher-order dynamic fields into MR image reconstruction Proceedings of the International Society for Magnetic Resonance in Medicine 2005; 681

[Wilson 2002] Wilson JL, Jenkinson M, Jezzard P.Optimization of static field homogeneity in human brain using diamagnetic passive shims. Magn Reson Med. 2002 ;48(5):906-14.

[Wilson 2003] Wilson JL, Jenkinson M, Jezzard P. Protocol to determine the optimal intraoral passive shim for minimisation of susceptibility artifact in human inferior frontal cortex. Neuroimage. 2003;19(4):1802-11.

[Wilson 2003a] Wilson JL, Jezzard P. Utilization of an intra-oral diamagnetic passive shim in functional MRI of the inferior frontal cortex. Magn Reson Med. 2003 ;50(5):1089-94.

[Yacoub 2001] Yacoub E, Shmuel A, Pfeuffer J, Van De Moortele PF, Adriany G, Andersen P, Vaughan JT, Merkle H, Ugurbil K, Hu X. Imaging brain function in humans at 7 Tesla. Magn Reson Med. 2001; 45, 588-594.

[Yoder 2004] Yoder DA, Zhao Y, Paschal CB, Fitzpatrick JM. MRI simulator with object-specific field map calculations. Magn Reson Imaging. 2004;22(3):315-28.

[Zhao 2005] Zhao Y, Anderson AW, Gore JC. Computer simulation studies of the effects of dynamic shimming on susceptibility artifacts in EPI at high field. J Magn Reson. 2005;173(1):10-22.

[Zhao 2005a] Zhao Y. Studies of Magnetic Susceptibility Artifacts in Magnetic Resonance Imaging. Dissertation Yale University 2005, New Haven, CT ,USA.